A&A manuscript no.
(will be inserted by hand later)

Your thesaurus codes are:
(02.08.1; 03.13.4; 08.03.4; 08.05.1; 08.13.2; 08.18.1)

ASTRONOMY AND ASTROPHYSICS

2-D non-LTE models of radiation driven winds from rotating early-type stars

I. Winds with an optically thin continuum

P. Petrenz and J. Puls

Universitäts-Sternwarte München, Scheinerstr. 1, 81679 München

Received; accepted

Abstract. We extend previous 2-D models of line-driven winds from rotating hot stars by accounting for the dependence of ionization structure and occupation numbers on local physical properties (density, velocity field) and the non-local stellar radiation field.

For this purpose, we formulate for the first time an approximate non-LTE description of 2-D winds. We propose the concept of a "mean irradiating atmosphere", which allows, in a computationally effective way and for all locations in the stellar wind, to consider the *frequency dependence* of the incident photospheric radiation field, which decisively determines the local ionization equilibrium.

Employing 2-D NLTE occupation numbers, force-multipliers and according force-multiplier parameters as function of (r, Θ), our hydrodynamic models are entirely self-consistent.

To estimate maximum effects arising from rotation and a consistent non-LTE approach, we concentrate on rapidly rotating B-star winds, since for this spectral regime the ionization structure is most sensitive to local conditions and variations of the radiation field. In order to avoid any contamination by the bi-stability effect (Lamers & Pauldrach 1991), we further restrict ourselves to winds with an optically thin Lyman continuum.

For all considered models, we find a *prolate* wind structure if gravity darkening and non-radial line forces are accounted for. Thus, the "$\varkappa$-effect" suggested by Maeder (1999), aiming at the possibility to obtain an oblate wind morphology, is actually *not* present for winds with an optically thin continuum. This result should be valid at least in the OB-star range.

The density contrast between the polar and the equatorial flow grows with rotation rate and decreases from thin winds ($\dot{M} \gtrsim 10^{-8}\,M_\odot\mathrm{yr}^{-1}$: $\rho_{\rm eq}/\rho_{\rm p} \lesssim 20\ldots30$) to denser ones ($\dot{M} \gtrsim 10^{-6}\,M_\odot\mathrm{yr}^{-1}$: $\rho_{\rm p}/\rho_{\rm eq} \lesssim 5$). The latter values are valid for winds rotating at 85 % of the break-up velocity. The variation of terminal velocity as function of latitude, however, is only small.

In comparison to simplified models with *global averages* for the force-multiplier parameters, the selfconsistent calculation results in a density contrast $\rho_{\rm p}/\rho_{\rm eq}$ larger by roughly a factor of two, with a moderately enhanced concentration of wind material over the poles and a significant reduction in the equatorial plane. This difference is shown to be the consequence of ionization effects, related to the specific *radial* dependence of the mean radiation temperature over the poles and about the equatorial plane, respectively.

We conclude that a quantitatively correct description of line-driven winds from rapidly rotating hot stars requires a self-consistent approach if the variation of $T_{\rm rad}(\Theta)$ at the stellar surface can induce a (significantly) stratified ionization equilibrium and should be included especially for B-stars with lower luminosities and thinner winds.

Our most important finding with regard to the influence of rotation on *global* wind properties is that the total mass-loss rate $\dot{M}_{\rm total}$ deviates from its 1-D value $\dot{M}_{\rm 1-D}$ (for $v_{\rm rot} = 0$) by at most 10…20 %, even for very high rotation rates ($v_{\rm rot} \lesssim 0.85 v_{\rm crit}$), except for winds from supergiants close to the Eddington-limit, where differences up to a factor of 2 become possible. We explain this remarkable coincidence by appropriate scaling relations and finally discuss our results with special emphasis regarding the wind-momentum luminosity relation of rapidly rotating stars.

Key words: hydrodynamics – methods: numerical – stars: early-type, mass-loss, winds, rotation

1. Introduction

During the last three decades, the theory of line-driving has been successfully applied to the winds from early-type hot stars, which exhibit mass-loss rates $\dot{M} \lesssim 10^{-4}\,M_\odot\mathrm{yr}^{-1}$ and terminal velocities $v_\infty \lesssim 3000\,\mathrm{km\,s}^{-1}$. Based on the pioneering work by Lucy & Solomon (1970), Castor (1974) and Castor et al. (1975, hereafter CAK), Pauldrach et al. (1986, hereafter PPK) and Friend & Abbott (1986) established the so-called *standard model* as the quantitative basis for numerous successful applications of this theory (for a review, see Kudritzki 1997).

Send offprint requests to: J. Puls(uh101aw@usm.uni-muenchen.de)

The most promising application, which has been discovered originally on a completely *empirical* basis, is the wind-momentum luminosity relation (WLR) between the modified wind-momentum rate $\dot{M} v_\infty R_*^{1/2}$ and the stellar luminosity L_* (Kudritzki et al. 1995). This relation (with an additional dependence on stellar metallicity) has also been understood from a theoretical point of view (Puls et al. 1996, 1998), and has been successfully used in several investigations (McCarthy et al. 1995, 1997, Kudritzki et al. 1999, Venn et al. 1999). In order to use this relation, a reliable value for the mass-loss derived from the observation must be available. In general, a successful determination of $\dot{M}$ requires a detailed knowledge of the conditions in the stellar wind (see, e.g., Petrenz & Puls 1996, hereafter PP96, and the references given therein). All investigations carried out so far may suffer from the assumption of the standard model for the stellar wind, which comprises the most simple flow geometry possible, namely a radially expanding spherically-symmetric wind. Thus, the influence of stellar rotation, which breaks the radial symmetry, is neglected in the hydrodynamic treatment. However, a significant fraction of early-type stars shows projected rotational velocities $v_{\rm rot} \sin i$ up to 50...80 % of the critical value $v_{\rm crit}$ (cf. Conti & Ebbetts 1977). Additionally, their spectra often show time-dependent features clearly correlated with the estimated rotational period (for most recent advances, see Wolf et al. 1999).

Of course, also stellar evolution is affected by rotational effects. Herrero et al. (1992) detected a systematic "mass discrepancy" in their quantitative spectroscopic study of a large sample of galactic O-stars. They found that for evolved O-stars approaching the Eddington-limit the stellar masses derived from evolutionary tracks and stellar luminosities are significantly larger than the masses obtained from spectroscopic gravities. Additionally, all rapid rotators of their sample showed a severe surface He-enrichment, the so-called "He discrepancy". Although an analysis by means of unified model atmospheres accounting for the presence of winds (Herrero et al 2000) has mitigated the mass discrepancy (however not ruled it out), the He discrepancy could be confirmed. Recent evolutionary calculations by Langer and Heger (1998), Maeder (1999), Meynet (1998) have indicated that stellar evolution including rotation and rotationally induced interior mixing could enhance the luminosity significantly for given mass. In addition, enhanced mass-loss along the evolutionary track would further reduce the mass and bring the evolutionary masses into agreement with the spectroscopic (and wind) masses (Langer et al. 1994).

¿From all of these perspectives, the neglect of rotation in the description of hot star atmospheres (photosphere + wind!) seems questionable. In recent years, this problem has been addressed by several theoretical studies. PPK and Friend & Abbott (1986) estimated the influence of stellar rotation on the wind dynamics in a *global* sense by solving the 1-D equations of motions in the equatorial plane only, considering the additional centrifugal acceleration term there. In result, they obtained an upper limit for the *actual* mass-loss rate, which should range in between the polar ($v_{\rm rot} = 0$) and the equatorial value derived by this method. In general, they expected the effects of rotation to become decisive for $\Omega \equiv v_{\rm rot}/v_{\rm crit} \gtrsim 0.5$.

The assumption of spherical symmetry has been dropped the first time by Bjorkman & Cassinelli (1993, hereafter BC). Employing the supersonic approximation, they solved for the particle trajectories in the polar plane, thus adopting *azimuthal symmetry* about the rotational axis. Additionally to the inertial accelerations, they considered a *purely radial line force* in the equations of motion. In this way, they provided simple expressions for density structure and the radial, polar and azimuthal components of the velocity field (v_r, v_Θ, v_Φ). In their model, they calculated the line force within the force-multiplier concept, where the corresponding force-multiplier parameters $k_{\rm CAK}$, α, δ (cf. CAK, Abbott 1982) were assumed *to be constant throughout the wind*, i.e., independent both of r and Θ. In the *1-D* case, these force-multiplier parameters allow a very simple and accurate parameterization of the line force which depends on the contribution of several hundred thousand lines of metal ions (for a thorough physical discussion based on a detailed study of the underlying line statistics, see Puls et al. 2000).

The BC model predicts a *polar deflection of the wind material towards the equatorial plane*, owing to the combined effect of centrifugal, gravitational and radiative acceleration. Thus, the spherical symmetry is broken, and the density contrast between equatorial and polar wind increases with distance r from the star. For extreme rotation rates ($\Omega \gtrsim 0.9 (0.5)$ for O(B)-stars), one expects the formation of a wind-compressed disk (WCD) in the equatorial plane, caused by the collision of wind material deflected from both hemispheres with polar velocities $v_\Theta \lesssim 5\, v_{\rm sound}$, with $v_{\rm sound}$ the (isothermal) speed of sound. The matter is decelerated in a shock front about the equatorial plane and feeds a slowly outward propagating stationary disk. Owocki et al. (1994, "OCB") confirmed the principal validity of this model by detailed radiation hydrodynamic simulations, and recovered some interesting additional effects (e.g., an *accretion* of the innermost disk material onto the stellar surface). For an independent confirmation of their results (with some refinements), see Petrenz (1999).

So far, the analytical BC model has been applied, e.g., for simulating the formation of *wind-compressed zones (WCZ)* in the winds from Wolf-Rayet stars (Cassinelli et al. 1995), as a possible explanation for the shape of the Homonculus nebula around η Carinae (MacLow et al. 1996), as underlying hydrodynamic wind model for H_α line synthesis (PP96) and for the investigation of wind compression effects in different areas of the HRD (Ignace et al. 1996).

Owocki et al. (1997, 1998) extended the BC model and studied the effects of *non-radial line force* components (acting in the polar and azimuthal direction, respectively), where the azimuthal components had been discussed the first time by Grinin (1978), and *gravity darkening* (i.e., the polar gradient of the stellar surface temperature from hot poles to cooler equatorial regions) on the wind dynamics.

The non-radial components of the line force lead to an *inhibition of disk formation* and a *redistribution* of the wind mate-

rial *towards the poles*. Additionally, the gravity darkening implies an enhanced (reduced) photon flux over the poles (in the equatorial plane) generating a *prolate density structure* of the wind with a denser and faster outflow over the rotational poles and a slower and thinner wind about the equatorial plane.

These results are in entire contradiction to the predictions by the simple BC model and, meanwhile, have been independently confirmed by Petrenz (1999); for a recent review, see Puls et al. (1999). Although severely challenging the validity of the wind compression mechanism, the results by Owocki et al. and Petrenz do not exclude the possibility that this mechanism might be decisive for outflows driven by other physical processes than line-driving.

One of the major problems of the described investigations is their assumption of force-multiplier parameters $k_{\rm CAK}$, α, δ being constant throughout the wind. Moreover, these parameters have been taken from 1-D calculations, where, in the actual 2-D situation, they should be affected by at least two processes. Firstly, both density and ionizing radiation field are a function of co-latitude Θ, and secondly, the assumption of constant force-multiplier parameters (with respect to radius) is rather questionable even for a uniformly bright stellar surface (cf. Kudritzki et al. 1998).

Thus, global 1-D parameters do not correctly account for the influence of *local physical conditions* (density, velocity field) and the *non-local stellar radiation field* on ionization stratification and occupation numbers (line opacities) in the wind.

Maeder (1999) has suggested the interesting possibility that due to the specific dependence of the force-multiplier parameters on temperature, the enhanced polar mass ejection due to gravity darkening described above may be progressively compensated by the effects of larger bound-free *and line* opacities, which then might favour a larger mass-flux in the cooler equatorial regions. Whether this suggestion ("$\varkappa$-effect") actually works can be answered only by a more realistic 2-D non-LTE model which accounts for the complicated physical conditions in winds from rapidly rotating early-type stars.

In this paper, we will introduce a procedure providing a 2-D parameterization of the line acceleration by means of force-multiplier parameters that are *consistent* both with the local hydrodynamic properties of the flow and the non-local latitude-dependent radiation field.

With this improved model we will try to give an estimate both for the consequences of stellar rotation on the wind dynamics and on maximum errors introduced by the assumption of a spherically-symmetric wind when, e.g., using mean relationships as the WLR.

The paper is organized as follows: In Sect. 2 we introduce the wind model and discuss the basic simplifications and approximations. In Sect. 3, we provide the basic formulae for the vector line and continuum acceleration. Sect. 4 describes how we determine the ionization equilibrium and the occupation numbers in the wind. Sect. 5 gives an overview over the basic properties of the line force-multiplier M with respect to different physical quantities. On the basis of this investigation, in Sect. 6 we introduce an approximate method for the parameterization of the line force in 2-D winds. In Sect. 7, we present the results for winds from rapidly rotating hot stars and estimate the differences to corresponding models with global force-multiplier parameters. In Sect. 8, we finally discuss the results and give future perspectives.

2. The model

2.1. Physical processes

Our 2-D wind model (with photospheric boundary) comprises the following physical effects:

- We consider the inertial (pseudo) accelerations in the equations of motion, i.e., the centrifugal and coriolis terms.
- As a consequence of rotation, the stellar surface is oblated (Collins 1963, 1965). The stellar radius increases as function of latitude from pole to equator, and we account for this effect in our numerical hydrodynamic simulations. For basic formulae, see OCB (Appendix A), Cranmer & Owocki (1995, "CO95") and Petrenz (1999).
- As shown by Owocki et al. (1997, 1998), Petrenz (1999) and Gayley & Owocki (2000), the non-radial components of both the continuum and line acceleration have a significant impact on the wind dynamics and have to be taken into account.
- The gravity darkening effect (see, e.g., Kippenhahn & Weigert 1991) leads to an enhanced (diminished) radiative acceleration over the poles and in the equatorial plane, respectively (cf. CO95, Owocki et al. 1997, 1998 and Petrenz 1999).

- The most important point in our work concerns the ionization structure and occupation numbers in the wind, which will be determined consistently with both the local physical properties of the wind material and the non-local stellar radiation field.

2.2. Physical approximations

To limit the complexity of our model and to facilitate the required computational effort, we will adopt following simplifications:

- We neglect the instability of the radiative line force (e.g., Owocki 1991, Feldmeier 1995), i.e., we assume a *"smooth" wind* without clumps and shocks which may arise from this instability. For studies of the large-scale wind morphology, this assumption is reasonable since the values of both density and velocity field averaged over small spatial length scales correspond to a macroscopic description by a smooth wind. Moreover, the correct numerical treatment of line force instabilities would require at least 2-D simulations that exceed available computational capacities (see, however, Owocki 1999).

– For the calculation of the stellar surface shape, we neglect the variation of the Thomson acceleration with stellar co-latitude owing to the polar temperature gradient. This effect may be important at most for extremely rapidly rotating *OB-supergiants* and has been controversely discussed by Langer (1998) and Glatzel (1998). From the viewpoint of stellar evolution theory, however, there is a still ongoing, controversial debate about the stellar surface properties of early-type massive stars. In particular, the competing processes of shear turbulence and meridional circulation counteract on the transport of angular momentum inside the star, thus being crucial for chemical mixing and stellar surface properties (see Meynet 1998, Maeder 1999).
Since our present study concentrates on B-stars (cf. Sect. 3.3) with $\Gamma_{1-\mathrm{D}} \lesssim 0.1$, we consider the Thomson acceleration only in an averaged way for calculating the shape of the stellar surface and replace M_* by the corresponding effective mass $M_{\mathrm{eff}} = M_* (1 - \Gamma)$ (cf. OCB, CO95 and PP96).
– In analogy to prior investigations (e.g., CO95), gravity darkening is considered in the framework of the von Zeipel (1924) theorem. Detailed studies recently performed by Maeder (1999) have revealed that the accuracy of this approximation is much better than expected, of order 10 %.
– Since there is no observational evidence for a *lower limit* of the (global) magnetic field strength at the surface of early-type stars, we do not consider magnetic fields in our hydrodynamic simulations (for a review, see Mathys 1999).
– In this first paper, we consider only winds with an *optically thin continuum*, i.e., stars with moderate mass-loss. Rapidly rotating B-supergiants with larger mass-loss rates ($\dot{M} \gtrsim 10^{-6}\ M_\odot \mathrm{yr}^{-1}$) and increasing optical depth in the Lyman continuum, which are thought to be candidates for the B[e] phenomenon via the bi-stability effect (Lamers & Pauldrach 1991, Lamers et al. 1999) will be covered in a forthcoming paper.
– Since we are primarily interested in the consequences of stellar rotation for the *large scale wind morphology*, we will not consider explicitly time-dependent processes (e.g., non-radial pulsations, rotational modulation). Observations of non-stationary spectral features have indicated dynamic variability on only rather small spatial scales.

2.3. Geometry and co-ordinate systems

Adopting rotational symmetry about the polar axis, we can formulate the hydrodynamic equations in spherical polar co-ordinates (Θ, Φ, r) (see Fig. 1). r denotes the distance from the stellar center, Θ the co-latitude ($\Theta = 0$ at the pole) and Φ the stellar azimuthal angle. At every location $\boldsymbol{r}$, a local right-handed orthonormal system $\{\boldsymbol{e}_\Theta, \boldsymbol{e}_\Phi, \boldsymbol{e}_r\}$ is defined by:

$$\boldsymbol{e}_\Theta = \begin{pmatrix} \cos\Theta\cos\Phi \\ \cos\Theta\sin\Phi \\ -\sin\Theta \end{pmatrix} \qquad \boldsymbol{e}_\Phi = \begin{pmatrix} -\sin\Phi \\ \cos\Phi \\ 0 \end{pmatrix}$$

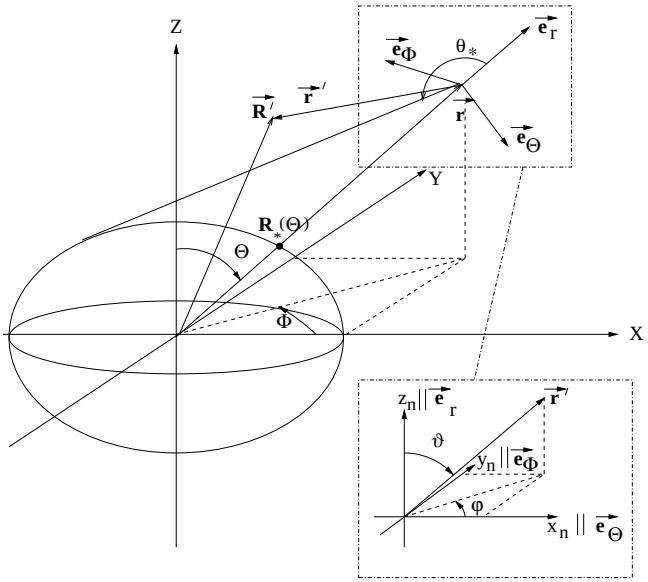

Fig. 1. Co-ordinate systems, see text.

$$\boldsymbol{e}_r = \begin{pmatrix} \sin\Theta\cos\Phi \\ \sin\Theta\sin\Phi \\ \cos\Theta \end{pmatrix} . \qquad (1)$$

The Cartesian co-ordinates of the stellar system are:

$$\boldsymbol{r} = \begin{pmatrix} X \\ Y \\ Z \end{pmatrix} = r \begin{pmatrix} \sin\Theta\cos\Phi \\ \sin\Theta\sin\Phi \\ \cos\Theta \end{pmatrix} \qquad (2)$$

In the local *"natural"* co-ordinate system (x_n, y_n, z_n), the local vector $\boldsymbol{r}'$ (which is needed, e.g., to calculate the cone angle subtended by the stellar disk) is given by:

$$\begin{aligned} \boldsymbol{r}'(\Theta, \Phi, r) &= r' \cdot (n_\Theta \boldsymbol{e}_\Theta + n_\Phi \boldsymbol{e}_\Phi + n_r \boldsymbol{e}_r) \\ &= r' \cdot \begin{pmatrix} \sin\vartheta\cos\varphi \\ \sin\vartheta\sin\varphi \\ \cos\vartheta \end{pmatrix} \equiv r' \cdot \boldsymbol{n} = \begin{pmatrix} x_n \\ y_n \\ z_n \end{pmatrix} . \end{aligned} \qquad (3)$$

Thus, the directional vector $\boldsymbol{n}$ is determined by the polar angles (ϑ, φ) in the system $(x_n, y_n, z_n) = (\boldsymbol{e}_\Theta, \boldsymbol{e}_\Phi, \boldsymbol{e}_r)$.

The stellar surface is given by the latitude-dependent stellar radius $R_*(\Theta)$ (Eq. 19 in PP96).

2.4. The hydrodynamic equations

We solve the *time-dependent* hydrodynamic equations for the wind. Their stationary solution is found if the numerical simulation has relaxed to a converged state. This procedure has the additional advantage that we may also perform simulations of non-stationary phenomena which can be described by time-dependent boundary conditions.

Due to azimuthal symmetry about the rotational Z-axis, the hydrodynamic equations reduce to the polar plane $(\Theta, r, \Phi \equiv 0)$. Their solution depends only on the polar co-ordinates (Θ, r), and all derivatives with respect to Φ vanish (for a deriva-

tion, see, e.g., Batchelor 1967):

$$\frac{\partial \rho}{\partial t} + \frac{1}{r^2}\frac{\partial r^2 \rho v_r}{\partial r} + \frac{1}{r\,\sin\Theta}\,\frac{\partial \rho v_\Theta\,\sin\Theta}{\partial \Theta} = 0 \tag{4}$$

$$\frac{\partial v_r}{\partial t} + v_r\,\frac{\partial v_r}{\partial r} + \frac{v_\Theta}{r}\,\frac{\partial v_r}{\partial \Theta} = \frac{{v_\Theta}^2 + {v_\Phi}^2}{r} - \frac{1}{\rho}\frac{\partial p}{\partial r} + g_r^{\rm ext} \tag{5}$$

$$\frac{\partial v_\Theta}{\partial t} + v_r\,\frac{\partial v_\Theta}{\partial r} + \frac{v_\Theta}{r}\,\frac{\partial v_\Theta}{\partial \Theta} = \frac{\cot\Theta {v_\Phi}^2}{r} - \frac{v_r v_\Theta}{r} - \frac{1}{\rho\, r}\,\frac{\partial p}{\partial \Theta} + g_\Theta^{\rm ext} \tag{6}$$

$$\frac{\partial v_\Phi}{\partial t} + v_r\,\frac{\partial v_\Phi}{\partial r} + \frac{v_\Theta}{r}\,\frac{\partial v_\Phi}{\partial \Theta} = -\frac{\cot\Theta v_\Theta v_\Phi}{r} - \frac{v_r v_\Phi}{r} + g_\Phi^{\rm ext} \tag{7}$$

$$p = v_{\rm sound}^2 \cdot \rho \tag{8}$$

with time t, velocity field (v_Θ, v_Φ, v_r), density ρ and pressure p. The external acceleration $\boldsymbol{g}^{\rm ext}$ is given by the sum of gravitational, line and Thomson acceleration

$$\boldsymbol{g}^{\rm ext} = \boldsymbol{g}^{\rm grav} + \boldsymbol{g}^{\rm lines} + \boldsymbol{g}^{\rm Th}. \tag{9}$$

Eq. 4 follows from mass conservation *(continuity)*, Eqs. 5-7 from momentum conservation *(equations of motion)*, and Eq. 8 is the isothermal *equation of state*. The use of the latter equation is justified (at least for a first qualitative study), since we do not account for line-driven instabilities that might generate strong shocks, and the time scales for other heating- and cooling processes are significantly smaller than typical flow times.

The velocity-dependent terms on the RHS of the equations of motion represent fictitious inertial accelerations arising from the curvi-linear nature of the spherical polar co-ordinates used to describe the flow. The only *true* body forces are pressure, gravitation and line force.

2.5. Numerical specifications

To solve the hydrodynamic equations Eqs. 4-8, we have adapted the time-dependent finite-difference 2-D Eulerian code ZEUS-2D (Stone & Norman 1992) to our specific problem. This well-tested and frequently used code allowed an *independent test* of the results published by OCB and Owocki et al. (1996,1997) who employed the hydrodynamic code VH-1 (developed by J. Blondin and collaborators) for their simulations.

ZEUS-2D solves the hydrodynamic equations for three velocity components (v_Θ, v_Φ, v_r) in the 2-D polar plane (Θ, r), i.e., for the 2.5-D geometry used to formulate our problem.

The flow variables are specified on a 2-D spatial grid $\{\Theta_j, r_i\}$ in radius r_i and co-latitude Θ_j. The mesh in radius is defined from an initial zone ($r_1 \approx R_{\rm p}$) out to a maximum zone at $r_{251} = r_{\rm max} \approx 14\,R_{\rm p}$. These zones are concentrated near the stellar surface where the flow gradients are steepest. The initial spacing ($r = 1.0...1.3\,R_{\rm p}$) is constant at $\Delta r = 0.002\,R_{\rm p}$. It then increases by 6% per zone out to the maximum radius $r_{\rm max}$. The *equidistant grid in co-latitude* Θ_j is defined from an initial zone ($j = 1$) adjacent to the pole ($\Theta = 0$) to a maximum zone ($j = 31$) adjacent to the equatorial plane ($\Theta = 90$).

As extensive test calculations have shown, this resolution of the computational domain is entirely sufficient for an investigation of the large-scale wind morphology. (Doubling the resolution both in radius and co-latitude only showed some correspondingly greater detail in small-scale flow structure.)

The most important numerical issue is to define an appropriate lower boundary condition, since the rotationally induced oblate stellar surface $R_*(\Theta)$ does not fit the curvi-linear *orthogonal* co-ordinate lines (Θ, r).

This issue has been addressed the first time by OCB who proposed to specify the lower boundary condition along a "staircase" that straddles the equipotential surface $R_*(\Theta)$ of the rigidly rotating star. We have chosen the same strategy, in accordance with the fact that this is the only "natural" way to treat the lower boundary condition for the geometry used to formulate our problem.

To guarantee a mildly subsonic inflow of wind material at the lower wind base which turned out to be essential for the stability of the flow and its convergence to a stationary state, we adjust the *base density* to a fixed value (if necessary, varying with co-latitude) and set the radial base velocity by constant slope extrapolation from the interior of the calculational domain.

To avoid meridional flows directly at the stellar surface, we assume a *no-slip* condition for the polar velocity component and rigid body rotation for the azimuthal velocity. Due to symmetry reasons, we choose reflecting boundary conditions along the polar axis and symmetric ones about the equatorial plane.

For a further discussion of specific technical details and problems, we refer the reader to OCB and Petrenz (1999, Sect. 6.).

3. The radiative acceleration

In this section, we introduce our notation and give a brief summary of basic expressions for the radiative acceleration. For detailed derivations, we refer the reader to the references cited in the following.

The general expression for radiative acceleration reads

$$\boldsymbol{g}^{\rm rad}(\boldsymbol{r},t) = \frac{1}{c}\int_0^\infty {\rm d}\nu \oint_{\Omega=4\pi} \kappa_\nu(\boldsymbol{r},\boldsymbol{n}',t)\, I_\nu(\boldsymbol{r},\boldsymbol{n}',t)\,\boldsymbol{n}'\,{\rm d}\Omega \equiv \boldsymbol{g}^{\rm lines}(\boldsymbol{r},t) + \boldsymbol{g}^{\rm cont}(\boldsymbol{r},t)\ . \tag{10}$$

with I_ν the specific intensity, $\kappa_\nu^{\rm lines\,(cont)}(\boldsymbol{r},\boldsymbol{n}',t)$ the mass-absorption coefficient for line (continuum) radiation, c the speed of light. $\boldsymbol{n}'$ denotes the direction vector $\boldsymbol{n}'$ which points from the considered location $\boldsymbol{r}$ into the direction of radiation and, thus, is anti-parallel to the direction vector $\boldsymbol{n}$ introduced in Fig. 1, i.e. $\boldsymbol{n}' = -\boldsymbol{n}$.

3.1. The continuum acceleration

As discussed above, we assume an *optically thin continuum* in the wind and neglect any diffuse radiation, i.e., the irradiation origins at the stellar surface and the corresponding intensity $I_\nu^{\rm c}(\boldsymbol{r},\boldsymbol{n}')$ experiences no attenuation between the star and $\boldsymbol{r}$. Thus, the intensity $I_\nu^{\rm c}(\boldsymbol{n}'=-\boldsymbol{n})$ is determined solely by the physical conditions at the location where the ray pointing from $\boldsymbol{r}$ to the stellar surface intercepts the latter for the first time.

In winds from early-type hot stars, the continuum radiative acceleration essentially arises from Thomson acceleration $\boldsymbol{g}^{\rm\ Th}$ and is a vector quantity given by (cf. CO95, Eq. 43)

$$\boldsymbol{g}^{\rm\ cont}(\boldsymbol{r}\,) = \begin{pmatrix} g_\Theta^{\rm cont} \\ g_\Phi^{\rm cont} \\ g_r^{\rm cont} \end{pmatrix} = \begin{pmatrix} \boldsymbol{g}^{\rm\ cont}\cdot\boldsymbol{e}_\Theta \\ \boldsymbol{g}^{\rm\ cont}\cdot\boldsymbol{e}_\Phi \\ \boldsymbol{g}^{\rm\ cont}\cdot\boldsymbol{e}_r \end{pmatrix}$$

$$= \frac{s_{\rm E}}{c}\int\limits_0^\infty {\rm d}\nu \int\limits_{\Omega=\Omega_{\rm c}} I_\nu^{\rm c}(\boldsymbol{r},\boldsymbol{n}')\,\boldsymbol{n}'\,{\rm d}\Omega \qquad (11)$$

$$= \frac{s_{\rm E}}{c}\int\limits_0^{2\pi}{\rm d}\varphi \int\limits_{\vartheta_*(\varphi)}^{\pi} \sin\vartheta{\rm d}\vartheta\,\frac{\sigma_{\rm B}T_{\rm eff}^4(\boldsymbol{r},\boldsymbol{n}')}{\pi}\begin{pmatrix} n'_\Theta \\ n'_\Phi \\ n'_r \end{pmatrix}, \qquad (12)$$

with L_* the stellar luminosity, $\rho s_{\rm E} = \sigma_{\rm Th}\cdot n_{\rm e}$ the electron scattering opacity, $\sigma_{\rm Th}$ the Thomson cross-section and $n_{\rm e}$ the electron number density. $\Omega_{\rm c}$ denotes the solid angle subtended by the stellar disk, and $\vartheta_*(\varphi)$ is the local polar angle confining $\Omega_{\rm c}$ (cf. Fig. 1). The electron density $n_{\rm e}$ follows from

$$n_{\rm e} = \frac{\rho}{m_{\rm p}}\left(\frac{1+I_{\rm He}Y_{\rm He}}{1+4Y_{\rm He}}\right), \qquad (13)$$

with $Y_{\rm He} = n_{\rm He}/n_{\rm H}$ the helium abundance, $m_{\rm p}$ the proton rest mass and $I_{\rm He}$ the number of free electrons per He atom (O-stars: $I_{\rm He}\approx 2$, B-stars: $I_{\rm He}\approx 1$, A-stars: $I_{\rm He}\approx 0$).

Note that the Thomson acceleration is a vector quantity and may have a *non-radial* component $g_\Theta^{\rm cont}$ in polar direction (if the stellar surface deviates from spherical symmetry or/and $T_{\rm eff}$ varies with co-latitude, see below), whereas the azimuthal component $g_\Phi^{\rm cont}$ vanishes due to symmetry about the rotational axis. In this case, both the polar and the radial component of the Thomson acceleration become a function of co-latitude Θ. Especially the latter implies some consequences for rapidly rotating supergiants with gravity darkening, as discussed in Sect. 3.3).

$T_{\rm eff}(\boldsymbol{r},\boldsymbol{n}')$ denotes the effective temperature at the stellar surface defined via the emerging frequency-integrated flux $F(\Theta_*)$ (see Sect. 3.3),

$$F(\Theta_*(\boldsymbol{r},\boldsymbol{n}')) \equiv \sigma_{\rm B}T_{\rm eff}^4(\boldsymbol{r},\boldsymbol{n}'). \qquad (14)$$

3.2. The line acceleration

By means of the *frequency-integrated* line opacity $\overline{\chi}_{\rm L}$

$$\overline{\chi}_{\rm L} = \frac{\pi e^2}{m_{\rm e}c}\,gf_{\rm L}((n_l/g_l)-(n_u/g_u)), \qquad (15)$$

with $gf_{\rm L}$ the gf-value, n_l, n_u, g_l, g_u the occupation numbers and statistical weights of the lower (l) and upper (u) levels, e the elementary charge and m_e the electron rest mass, we define the *line-strength* $k_{\rm L}$

$$k_{\rm L} = \frac{\overline{\chi}_{\rm L}}{\Delta\nu_{\rm D}\,\sigma_{\rm e}}, \qquad (16)$$

with $\nu_{\rm L}$ the line transition frequency and $\Delta\nu_{\rm D} = \nu_{\rm L}v_{\rm therm}/c$ the Doppler-width. $v_{\rm therm}$ denotes the thermal velocity.

As the continuum acceleration, the line acceleration is a vector quantity (cf. CO95, Eq. 44), defined in the Sobolev approximation as the sum over an ensemble of lines:

$$\boldsymbol{g}^{\rm\ lines}(\boldsymbol{r}\,) = \sum_{\rm lines\ L}\frac{\overline{\chi}_{\rm L}(\boldsymbol{r}\,)}{c\rho(\boldsymbol{r}\,)}$$

$$\times\int\limits_{\Omega_{\rm c}} I_\nu^{\rm c}(\boldsymbol{r},\boldsymbol{n}')\left(\frac{1-\exp(-\tau_{\rm S}(\boldsymbol{r},\boldsymbol{n}'))}{\tau_{\rm S}(\boldsymbol{r},\boldsymbol{n}')}\right)\boldsymbol{n}'{\rm d}\Omega, \qquad (17)$$

with $\tau_{\rm S}$ the optical depth in Sobolev approximation [1],

$$\tau_{\rm S}(\boldsymbol{r},\boldsymbol{n}') = k_{\rm L}\,\frac{s_{\rm E}\rho(\boldsymbol{r}\,)v_{\rm therm}}{|\boldsymbol{n}'\cdot\nabla(\boldsymbol{n}'\boldsymbol{v})|} \equiv k_{\rm L}\,t_{\rm S}\,. \qquad (18)$$

$t_{\rm S} = s_{\rm E}\rho(\boldsymbol{r}\,)v_{\rm therm}/|\boldsymbol{n}'\cdot\nabla(\boldsymbol{n}'\boldsymbol{v})|$ denotes the generalized depth parameter depending on the absolute value of the directional velocity derivative $|\boldsymbol{n}'\cdot\nabla(\boldsymbol{n}'\boldsymbol{v})|$, which, for spherical symmetry, collapses to the depth parameter introduced by CAK, $t_r = s_{\rm E}\rho(\boldsymbol{r}\,)v_{\rm therm}/({\rm d}v_r/{\rm d}r)$.

According to the findings by CAK, Abbott (1982) and Puls et al. (2000), the number distribution of spectral lines ${\rm d}N(\nu,k_{\rm L})$ with frequency $\nu\in[\nu,\nu+{\rm d}\nu]$ and line-strength $k_{\rm L}\in[k_{\rm L},k_{\rm L}+{\rm d}k_{\rm L}]$ can be approximated by a power-law *line-strength distribution function*

$${\rm d}N(\nu,k_{\rm L}) = -N_0\,f_\nu(\nu)\,k_{\rm L}^{\alpha-2}\,{\rm d}\nu\,{\rm d}k_{\rm L}\,\exp(-k_{\rm L}/k_{\rm max}), \qquad (19)$$

with $\alpha\in[0,1]$ and a frequency distribution $f_\nu(\nu)$ *independent* of line strength. The quantity N_0 normally varies with location $\boldsymbol{r}$.

The additional exponential factor with *maximum line-strength* $k_{\rm max}$ has been introduced by Owocki et al. (1988) in order to prevent the number of (strong) lines from becoming smaller than unity. Note that this parameterization does not consider line-overlaps and multi-line effects, i.e., we restrict ourselves to the *single-line* scattering case where the photons interact with the ions in such a way as if each line would be well separated from its neighbour, independently of line density.

Employing this line distribution function allows the transition from the sum in Eq. 17 to an integral. After some algebra, we obtain with Eq. 18 for $\tau_{\rm S}$ (cf. CO95) and assuming $k_{\rm max}\to\infty$

$$\boldsymbol{g}^{\rm\ lines}(\boldsymbol{r}\,) = \frac{s_{\rm E}^{1-\alpha}v_{\rm therm}N_0}{c^2}\,\frac{\Gamma(\alpha)}{1-\alpha}\int\limits_0^\infty {\rm d}\nu\,f_\nu(\nu)\,\nu\left(\frac{I_\nu^{\rm c}}{I^{\rm c}}\right)$$

[1] In order to simplify notation, we have omitted any time-dependence, although $\boldsymbol{v}$, ρ etc. are in general time-dependent quantities.

$$\times \int\limits_{\Omega_c} \mathrm{d}\Omega\, \boldsymbol{n}'\, I^{\mathrm{c}}(\boldsymbol{r},\boldsymbol{n}') \left(\frac{|\boldsymbol{n}'\cdot\nabla(\boldsymbol{n}'\boldsymbol{v})|}{\rho(\boldsymbol{r})v_{\mathrm{therm}}}\right)^{\alpha} . \quad (20)$$

In this expression, α is still considered as a *global* parameter *constant throughout the wind*, i.e., independent of the actual local physical conditions. We will drop this assumption below (see Sect. 6.3).

$I^{\mathrm{c}}(\boldsymbol{r},\boldsymbol{n}')$ is the frequency-integrated stellar intensity, and we have neglected the dependence of $(I^{\mathrm{c}}_{\nu}(\boldsymbol{r},\boldsymbol{n}')/I^{\mathrm{c}}(\boldsymbol{r},\boldsymbol{n}'))$ on direction $\boldsymbol{n}'$. In principle, the polar surface temperature gradient owing to gravity darkening may have an actual impact, if the intensities at the poles, respectively at the equator, have their maxima in different frequency ranges with a different number of contributing lines. However, we accept this approximation, in particular with respect to the line force parameterization proposed in Sect. 6.

To account for the dependence of the ionization structure on particle density and dilution of the stellar radiation field, Abbott (1982) introduced an additional factor which represents the largest part of variation of N_0,

$$\left(\frac{n_{\mathrm{e}}\cdot 10^{-11}}{W_{1-\mathrm{D}}}\right)^{\delta} , \quad (21)$$

with $W_{1-\mathrm{D}}$ the spherical dilution factor (the generalization for arbitrary stellar surfaces is given by Eq. 29),

$$W_{1-\mathrm{D}} = \frac{1}{2}\left[1-\left(1-(R_*/r)^2\right)^{1/2}\right] . \quad (22)$$

Introducing now the *force-multiplier parameter* k_{CAK} (cf. CAK, Puls et al. 2000)

$$k_{\mathrm{CAK}} = \frac{N_0 v_{\mathrm{therm}}}{c}\,\frac{\Gamma(\alpha)}{1-\alpha}\int\limits_0^{\infty}\mathrm{d}\nu\, f_{\nu}(\nu)\,\nu\left(\frac{I^{\mathrm{c}}_{\nu}}{I^{\mathrm{c}}}\right) , \quad (23)$$

the line force finally reads

$$\boldsymbol{g}^{\,\mathrm{lines}}(\boldsymbol{r}) = \frac{s_{\mathrm{E}}^{1-\alpha}k_{\mathrm{CAK}}}{c}\left(\frac{n_{\mathrm{e}}\cdot 10^{-11}}{W_{1-\mathrm{D}}}\right)^{\delta} \times \int\limits_{\Omega_c}\mathrm{d}\Omega\,\boldsymbol{n}' I^{\mathrm{c}}(\boldsymbol{r},\boldsymbol{n}')\left(\frac{|\boldsymbol{n}'\cdot\nabla(\boldsymbol{n}'\boldsymbol{v})|}{\rho(\boldsymbol{r})v_{\mathrm{therm}}}\right)^{\alpha} . \quad (24)$$

Like α, also k_{CAK} (essentially N_0) and δ are considered as *global parameters* so far. We will drop this approximation in Sect. 6.3.

Finally, we need the expression for the directional derivative $|\boldsymbol{n}\cdot\nabla(\boldsymbol{n}\boldsymbol{v})|$. Due to symmetry about the polar axis, this quantity simplifies to the expression given by CO95 (Eqs. 41/42) [2] (for a derivation, see, e.g., Batchelor 1967, Koninx 1992).

For a *spherically-symmetric* wind from a uniformly bright stellar surface, the line acceleration given by Eq. 24 reads (cf. CAK, PPK, Friend & Abbott 1986)

$$\boldsymbol{g}^{\,\mathrm{lines}}(\boldsymbol{r}) = \boldsymbol{e}_r\cdot\frac{s_{\mathrm{E}}L_*}{4\pi r^2 c}\,CF(r,v_r,\mathrm{d}v_r/\mathrm{d}r)\,M(t_r) \quad (25)$$

[2] Concerning the notation in their paper, the angles (Θ',Φ') correspond to (ϑ,φ) used in this paper.

$M(t_r)$ denotes the *force-multiplier*, given by the ratio of radial line to Thomson acceleration

$$M(t_r) = \frac{v_{\mathrm{therm}}}{c}\frac{1}{t_r}\sum_{\mathrm{lines\,L}}\frac{\nu_L F_{\nu_L}}{F}\left(1-e^{-k_{\mathrm{L}}t_r}\right) . \quad (26)$$

This quantity is usually parameterized by means of the force-multiplier parameters k_{CAK}, α, δ (for an alternative parameterization, see Gayley 1995):

$$M(t_r) = k_{\mathrm{CAK}}\,t_r^{-\alpha}\left(\frac{n_{\mathrm{e}}\cdot 10^{-11}}{W_{1-\mathrm{D}}(r)}\right)^{\delta} . \quad (27)$$

With the knowledge of k_{CAK}, α, δ as a function of effective temperature (and metallicity), the stellar mass-loss rate and the terminal velocity can be easily calculated for every evolutionary state of the star, e.g., by means of the analytical formulae provided by Kudritzki et al. (1989).

3.3. Impact of non-radial line forces and gravity darkening on the wind dynamics

The influence of non-radial line force components and gravity darkening on the radiative line and the wind dynamics has been investigated in detail by CO95, Owocki et al. (1996 , 1997) and, with some refinements, by Petrenz (1999). In all these investigations, the line force has been parameterized by *global* parameters k_{CAK}, α, δ adopted from 1-D non-LTE calculations. In the following, we only summarize the main results.

As a consequence of asymmetries in the local directional derivative of the velocity field, the line acceleration has non-radial components $g_{\Theta}^{\mathrm{lines}}$ along the polar and $g_{\Phi}^{\mathrm{lines}}$ along the azimuthal direction, which imply following effects: Firstly, the polar component $g_{\Theta}^{\mathrm{lines}}$ scales with the polar gradient of the radial velocity field $\partial v_r/\partial\Theta$. The latter is negative close to the star, where $g_{\Theta}^{\mathrm{lines}}$ is of the same order of magnitude as the inertial (centrifugal and coriolis) accelerations ($\sim 10^2\ldots10^3\mathrm{cm\,s^{-2}}$) and becomes decisive for the wind dynamics. As a result of the balance of these accelerations, the disk formation is inhibited and the wind material is redistributed towards the polar regions with maximum (absolute) polar velocities $v_{\Theta}\approx 80\ldots100\,\mathrm{km\,s^{-1}}$, whereas the radial component g_r^{lines} stabilizes the flow against gravity (with $g_r^{\mathrm{lines}}\gtrsim 10^3\ldots3\cdot10^4\,\mathrm{cm\,s^{-2}}$).

The density contrast between the equatorial and the polar wind $\rho_{\mathrm{eq}}/\rho_{\mathrm{p}}$ ranges in between 2...8, and typical terminal velocities $v_{\infty}(\Theta)$ are $v_{\infty}(0°)\approx 1300(2100)\,\mathrm{km\,s^{-1}}$ and $v_{\infty}(90°)\approx 350(1700)\,\mathrm{km\,s^{-1}}$ for B-(O-)star winds.

The azimuthal component $g_{\Phi}^{\mathrm{lines}}$ scales with the radial gradient of the azimuthal velocity field $\partial v_{\Phi}/\partial r$. If the latter is *smaller* than v_{Φ}/r (i.e., for any rotation law with v_{Φ} increasing with r smaller than for rigid body rotation), $g_{\Phi}^{\mathrm{lines}}$ becomes negative and *spins down the wind*. In the equatorial plane, where the maximum effects occur, $v_{\mathrm{rot}}(r)$ is diminished by up to $\lesssim 100\,\mathrm{km\,s^{-1}}$, in comparison with an angular momentum conservation law (for an analytical discussion of the spin-down effect, see Gayley & Owocki 2000).

In comparison to a non-rotating star with an uniformly bright surface, a star with gravity darkening is expected to show a higher (lower) mass-loss over the poles (at the equator) owing to the enhanced (diminished) radiative flux. Typical quantitative effects on the surface properties of rotating stars owing to gravity darkening become clear from the data listed in Tab. 1/2.

Isolating the pure effect of gravity darkening (still accounting for the inertial acceleration terms, however assuming only a radial line force) yields, again for constant force-multiplier parameters, a slightly oblate wind structure with a moderately compressed disk in the equatorial plane. The density contrast $\rho_{\rm eq}/\rho_{\rm p} \approx 3$ is much smaller than in the pure WCD model ($\rho_{\rm eq}/\rho_{\rm p} \approx 50 \ldots 100$), and terminal velocities of order $v_\infty(0^\circ) \approx 1400\,\mathrm{km\,s^{-1}}$, and $v_\infty(90^\circ) \approx 500\,\mathrm{km\,s^{-1}}$ are found for typical B-star parameters.

If one additionally accounts for the non-radial line force components, finally a *prolate* wind morphology results, with density contrasts $\rho_{\rm eq}/\rho_{\rm p}$ of order $0.2 \ldots 0.5$. For supergiants with considerable Eddington-luminosity, gravity darkening has an additional impact on the wind dynamics via Thomson acceleration $\boldsymbol{g}^{\rm cont} = \boldsymbol{g}^{\rm Th}$, which approximately scales with the fourth power of the mean radiation field temperature and, consequently, is more (less) effective over the poles (in the equatorial plane) than in the wind of a uniformly bright star. This behaviour induces an even stronger concentration of wind material over the poles, with $\rho_{\rm eq}/\rho_{\rm p} \approx 0.2$, where for a wind with purely radial 1-D Thomson acceleration, this ratio would be only ~ 0.5.

With respect to global wind properties, stellar rotation implies the following consequences: A comparison of surface-integrated mass-loss rates of 2-D models $\dot{M}_{\rm 2-D}$ with the value for $v_{\rm rot} = 0$ yields a maximum increase of $\dot{M}$ by a factor of 2.0…2.5. The ratio $v_\infty(0^\circ)/v_\infty(90^\circ)$ is $\lesssim 2$ for O-supergiants and $\lesssim 5 \ldots 6$ for main-sequence B-stars. However, these maximum effects require rotational velocities $v_{\rm rot} \approx 0.7 \ldots 0.8\, v_{\rm crit,2-D}$.

In view of the studies performed so far and their specific shortcomings (especially the use of globally defined force-multiplier parameters neglecting the 2-D situation, in particular if gravity darkening is accounted for), we will concentrate on the B-star domain ($T_{\rm eff} \approx 20000$ K) in our following investigations, and comment on hotter winds only when necessary. Briefly, the reasons for this strategy are:

- In the considered temperature range, the reaction of the ionization equilibrium on small variations of $T_{\rm eff}$ (as function of Θ, if gravity darkening is accounted for) is at maximum. Thus, also the effects resulting from a consistent 2-D NLTE treatment should be at maximum in this domain. Note that for O-star winds the variation of ionization structure with temperature is much weaker, and the assumption of constant force-multiplier parameters may be much better justified there.
- The generalization of our results to cases of higher mass-loss will allow for a future discussion concerning the formation of B[e] star disks, one of the most prominent manifestations of the inter-relation between wind, rotation and (2-D) radiative driving, at least if one follows the presently favoured scenario (cf. Lamers & Pauldrach 1991, Lamers et al. 1999, however also Owocki et al. 1997 for the counteracting rôle of gravity darkening).
- Finally, all prior investigations resulting in *detailed* (numerical) models have concentrated on the B-star regime, as a consequence of the work by BC, who suggested the wind-compression scenario as one possible explanation for the Be-star phenomenon. In order to compare our findings with those more simpler, however well-documented approaches, and to investigate the importance of a consistent description, an inspection of this parameter range is inevitable anyway.

4. Ionization equilibrium and occupation numbers

The parameterization of the line acceleration at location $\boldsymbol{r}$ requires the knowledge of the local force-multipliers $M(\boldsymbol{r})$ (Eq. 26 and Sect. 5). To calculate these quantities via the frequency and line strength distribution of the contributing lines, we determine the ionization structure and occupation numbers in the wind by employing an approximate method developed by Abbott & Lucy (1985), Schmutz (1991), Lucy (unpublished notes) and Springmann (1997). In contrast to the "exact" self-consistent non-LTE solution, this simplified Ansatz allows a comparatively fast *local* solution of the rate equations (within reasonable physical approximations). This is essential with respect to the substantial computational effort required by our multidimensional problem.

4.1. Basic formulae

Ionizing radiation field. We calculate the ionizing radiation field J_ν by

$$J_\nu(\boldsymbol{r}) = \frac{1}{4\pi} \int\limits_{\Omega=4\pi} I_\nu(\boldsymbol{r},\boldsymbol{n})\,\mathrm{d}\Omega \equiv W(\boldsymbol{r}) I_\nu(T_{\rm rad}(\boldsymbol{r},\nu))\,, \quad (28)$$

with *dilution factor*

$$W(\boldsymbol{r}) = (4\pi)^{-1}\hat{\Omega}_{\rm c},\ \hat{\Omega}_{\rm c} := \int_{\Omega_{\rm c}} \mathrm{d}\Omega\ , \quad (29)$$

accounting for the geometrical dilution of the incident stellar radiation field. For a spherical star, this expression simplifies to Eq. 22.

The intensity $I_\nu(T_{\rm rad}(\boldsymbol{r},\nu))$ with radiation temperature $T_{\rm rad}(\boldsymbol{r},\nu)$ describes the frequency-dependent photon distribution *emerging from the photosphere* and is taken either as Planckian or from Kurucz flux distributions (Kurucz 1992). Both flux distributions give rise to different ionization structures, since the frequency dependence $T_{\rm rad}(\nu)$ of the Kurucz flux distribution implies a drastically smaller ionizing flux for wavelengths shortward of the Lyman edge (see below).

The above approximation for J_ν, of course, is only valid in the case of an optically thin continuum in the wind, as discussed here.

Ionization equilibrium. With the electron temperature taken as a constant fraction of the effective temperature (typically 0.8) and the radiation temperature as either the effective one (Planck case) or significantly lower shortward of the flux maximum (Kurucz fluxes, see Sect. 5), the ionization equilibrium reads

$$\frac{n_{1,j+1}n_e}{n_{1,j}} = W\sqrt{\frac{T_\mathrm{e}}{T_\mathrm{rad}}}\left(\frac{n_{1,j+1}n_e}{n_{1,j}}\right)^*_{T_\mathrm{rad}} \times \{\zeta+\eta+W(1-\eta-\zeta)\}\,. \quad (30)$$

The asterisk denotes thermodynamic equilibrium values, and ζ and η are the fraction of recombination processes leading directly to the ground and meta-stable levels, respectively. For details, see Springmann (1997).

Occupation numbers. Having determined the ionization structure, we can calculate the occupation numbers (e.g., Puls et al. 2000). For the wind dynamics, we consider (in agreement with Abbott & Lucy 1985) only the crucial lines (giving rise to more than 90 % of the line acceleration), which are those with the lower level as a ground, meta-stable or so-called "1st order" subordinate state. The latter are defined as those subordinate levels which have a *direct* transition either to the ground or to a meta-stable state. Since we neglect stimulated emission, we only need the occupation numbers for the *lower* levels defined in this way.

Atomic data. In order to perform the above calculations, we employ the Munich atomic data bank provided by A. Pauldrach and collaborators. For a description, see Pauldrach et al. (1998).

5. Properties of the force-multiplier

In a perfect numerical model, one would determine the line force at location $\boldsymbol{r}$ by summing up the contribution of some 10^5 lines, which is presently not possible because of computational restrictions. As mentioned before in Sect. 3.2, the calculation of the line force becomes feasible by utilizing the force multiplier concept with corresponding parameters k_CAK, α, δ, which in earlier investigations were treated as constant throughout the entire wind (see however Kudritzki et al. 1998)

Usually, however, detailed 1-D non-LTE calculations (cf. Pauldrach et al. 1994) yield *depth-dependent* force-multiplier parameters. Only *a posteriori*, it is possible to find representative global values $<k_\mathrm{CAK}>, <\alpha>, <\delta>$ which can reproduce the results of the hydrodynamic simulation with depth dependent force-multiplier parameters. Unfortunately, the knowledge of these global parameters requires enormous computational effort, and moreover, these force-multiplier parameters have been calculated *only for spherically-symmetric winds*. To allow for a realistic parameterization of the line force in winds from rapidly rotating stars, we generalize the *depth-dependent* approach for 1-D winds proposed by Kudritzki et al. (1998).

For this purpose, we (re)investigate the behaviour of the force-muliplier as function of different physical quantities.

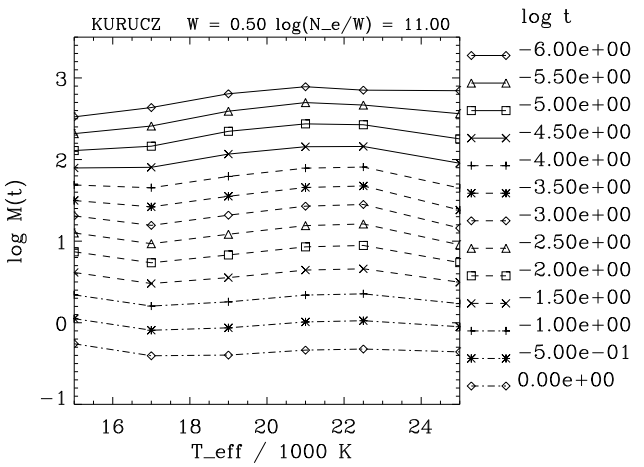

Fig. 2. Force-multiplier M as a function of temperature, for different values of optical depth parameter t_S. Irradiation by Kurucz flux distributions for $\log g = 3.0$.

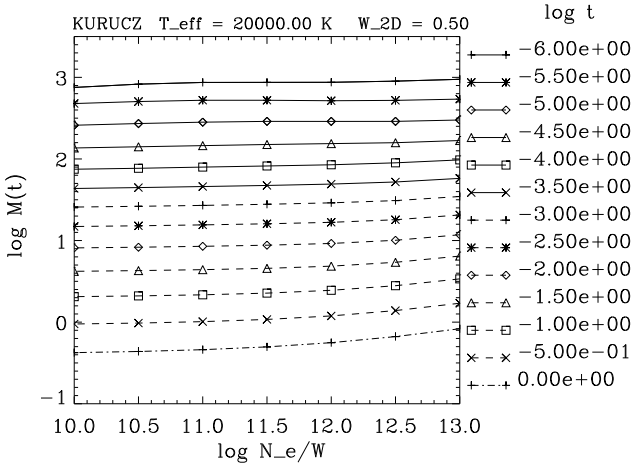

Fig. 3. Dependence of force-multipliers M on effective wind density n_e/W for different values of t_S. Irradiation by Kurucz fluxes, $T_\mathrm{eff} = 20000$ K and $\log g = 3.0$.

Since we will concentrate primarily on B-star winds, as outlined in Sect. 3.3, we will restrict ourselves to the according parameter space.

Dependence on temperature. Even with our significantly extended line list, we recover the earlier result by Abbott (1982) that the force-multiplier M varies only mildly with temperature (at most by a factor of 2...3) in the B star domain[3] ($T_\mathrm{eff} \approx 15\ldots25$ kK), as shown in Fig. 2 for an irradiation by Kurucz fluxes. The reason for this remarkable constancy – note that the ionization balance is changing significantly throughout the considered temperature range – is given by the fact that the strongest driving lines remain concentrated close to the maximum of the ionizing radiation field ($\sim \nu F_\nu$). This coincidence arises from the *influence of the radiation field on the ionization balance*: For wind densities typical for OB-stars the ionization potential of the major ionization stage is approximately $E_\mathrm{ion} \approx 20\ldots30\,k_\mathrm{B}T_\mathrm{eff}$, and the wavelength of reso-

[3] Actually, this is also true for O-stars.

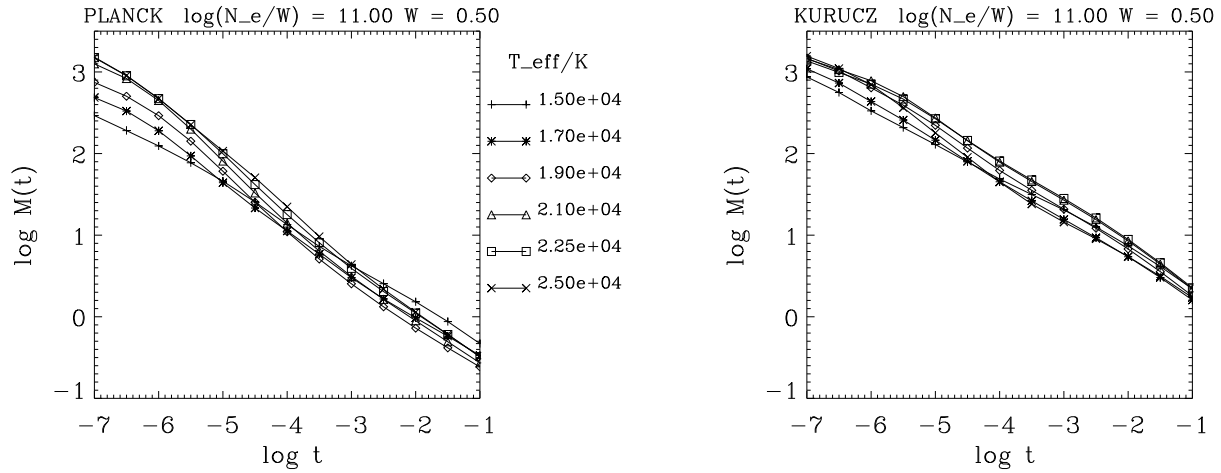

Fig. 4. Force-multiplier $M(t_{\rm S})$. Illumination with Planck spectrum (left) and Kurucz flux distribution for $\log g = 3.00$ (right). Note that $\log t_{\rm S}$ is usually a decreasing function of radial wind velocity.

nance transitions from the major ionization stage is of the order $\sim E_{\rm ion} \approx 5 \ldots 7\, k_{\rm B} T_{\rm eff}$. Since the maximum of the function νB_ν approximately equals $4\, k_{\rm B} T_{\rm eff}$, the *strongest* lines are situated close to this value, almost independent on the actual ionization structure.

For temperatures $T_{\rm eff} \lesssim 10000$ K, the flux maximum shifts to the Paschen continuum, whereas the most important transitions (even if neutral elements would play a rôle) are still in the Balmer continuum. As a consequence, the line acceleration rapidly decreases for temperatures below 10000 K.

Dependence on density. The quantity $g^{\rm lines}$ and thus the force-multiplier depends on density in two different ways: Firstly, $g^{\rm lines}$ scales inversely with density via $g^{\rm lines} \sim 1/\rho^{\alpha-\delta}$ (see Eq. 24) because the atoms that absorb radiation in the frequency interval $\Delta\nu_{\rm D}$ have a mass per unit area of $\rho v_{\rm therm}/(\mathrm{d}\, v_r/\mathrm{d}\, r)$. This *explicit* dependence is absorbed in the optical depth parameter $t_{\rm S}$ [4] and the δ term, i.e., the larger $t_{\rm S}$ the smaller is the resulting force-multiplier $M(t_{\rm S})$, as shown in Fig. 4. Secondly, $g^{\rm lines}$ *implicitly* depends on density via the ionization structure. Because lower ionization stages have more lines (close to the flux maximum), the line force grows with enhanced density for given $t_{\rm S}$. Note, that the *effective* wind density controlling the ionization balance is given by $n_{\rm e}/W$ (Eq. 30). This ratio varies significantly only in the lowest part of the wind and becomes almost constant for larger radii, since the electron density as well as the dilution factor asymptotically scale with $1/r^2$. Fig. 3 illustrates this implicit dependence of the force-multiplier.

Dependence on dilution factor. As already shown by Springmann (1997, Fig. 4.4), the force-multiplier varies with W via the contribution of subordinate lines. For these lines, the occupation numbers of the corresponding levels explicitly depend on W. However, photoionizations from subordinate levels affect the ionization equilibrium only close to the star ($W \gtrsim 0.1$), and subordinate lines contribute anyway less than 10% to the line force in the considered temperature range (see Abbott 1982). Accordingly, the explicit dependence of M on W is only weak.

Dependence on ionization structure. The ionization structure is determined by the ionizing radiation field (and the effective density) and is decisive for the force-multiplier. In the following, we discuss some physical consequences for M as the result of different temperatures and/or ionization structures

Fig. 4 displays the quantity M in the relevant $t_{\rm S}$ range for $\log(n_{\rm e}/W) = 11$, $W = 0.5$ and Planck (left) and Kurucz (right) flux distributions ($\log g = 3.0$), respectively, as function of $T_{\rm eff} = 15000 \ldots 25000$ K. For fixed $\log t_{\rm S}$, M varies with temperature by a factor less than $2 \ldots 3$ ($\lesssim 0.5$ dex) in both cases and is a monotonically decreasing function of $t_{\rm S}$, as already pointed out. Note that $\log t_{\rm S}$ is usually a decreasing function of radial wind velocity, i.e., the right parts of the figures correspond to the situation in the inner wind.

For Planck irradiation, the force-multipliers show the strongest variations for different temperatures at low $\log t_{\rm S}$ ($\Delta \log M \lesssim 0.7$, for $\log t_{\rm S} \lesssim -6$), whereas for Kurucz flux distributions this behaviour is not found, and M is markedly larger (roughly 0.8 dex) for large values of $\log t_{\rm S}$.

To understand these differences, let us take a closer look at the underlying physics. The contribution of the various elements to the total line acceleration is displayed in Fig. 5 ($W = 0.5$ and $\log(n_{\rm e}/W) = 11$), where we have plotted the logarithm of the quantity

$$N_{\rm eff} = \sum_{\rm lines\ L} \frac{\nu F_\nu}{F} (1 - e^{-k_{\rm L} t_{\rm S}}) \qquad (31)$$

[4] In the following, we denote this parameter by $t_{\rm S}$, independently of any direction, since M is an explicit function only of $t_{\rm S}$ and not of any distinct direction.

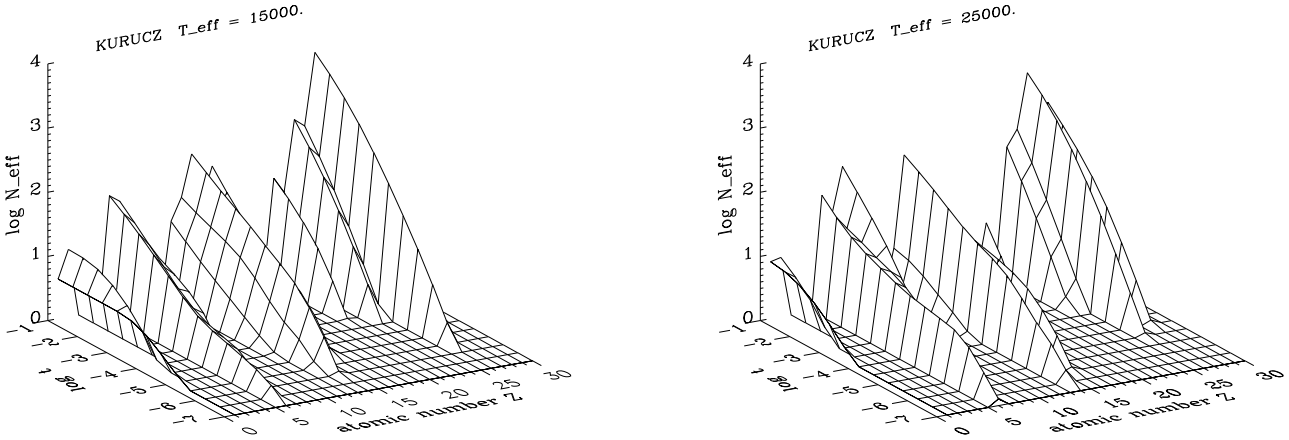

Fig. 5. Contribution of different atomic species to the line acceleration for $T_{\rm eff} = 15000$ K (left) and 25000 K (right), plotted over atomic number Z and optical depth parameter $t_{\rm S}$. For the defi nition of $N_{\rm eff}$, see text. Kurucz irradiation, $W = 0.5$, $\log(n_{\rm e}/W) = 11$.

over the atomic number Z and $\log t_{\rm S}$[5]. In both cases, the largest contributors are the CNO group (Z = 6 ... 8), the elements silicon, phosphorus, sulfur and argon (Z = 14, 15, 16, 18), and the elements of the iron group (chromium, manganese, iron and nickel (Z = 24, 25, 26, 28). For very small values of $\log t_{\rm S}$ ($\log t_{\rm S} \lesssim -6$), only the CNO group (for $T_{\rm eff} = 25000$ K, additionally phosphorus and sulfur) contributes significantly to $N_{\rm eff}$. For large $\log t_{\rm S}$ ($\log t_{\rm S} \gtrsim -2$), iron dominates the other elements by far (note the logarithmic scale for $N_{\rm eff}$!) (cf. Puls et al. 2000).

Since the considered parameter space represents winds which are not optically thick yet, the line transitions of the most abundant elements are mostly unsaturated (except for single meta-stable and resonance transitions), and $N_{\rm eff}$ follows closely the adopted abundance pattern (solar abundances, taken from Anders & Grevesse 1989 and Grevesse et al. 1996).

For *Kurucz irradiation*, the force-multipliers are markedly larger than for the black body case, owing to systematically *lower ionization stages* in the former. Fig. 6 shows the major ionization stages for $T_{\rm eff} = 20000$ K, $W = 0.5$ and $\log(n_{\rm e}/W) = 11$ present in both cases. For Kurucz fluxes, in particular the major ionization stages of the most contributing elements are one stage below the ones in the Planck case. Since the lower ionization stages provide more driving lines, also the force-multipliers are larger. This behaviour is a consequence of the reduced ionizing flux below the Lyman edge (911 Å).

Fig. 7 displays the frequency dependent radiation temperature $T_{\rm rad}(\nu)$ of the adopted Kurucz fluxes: the radiation temperatures at the decisive transitions (see Figure) are much smaller than in the Planck case, of course due to line-blocking, which is one of the most important physical ingredients which has to be accounted for in calculating *realistic* stellar model

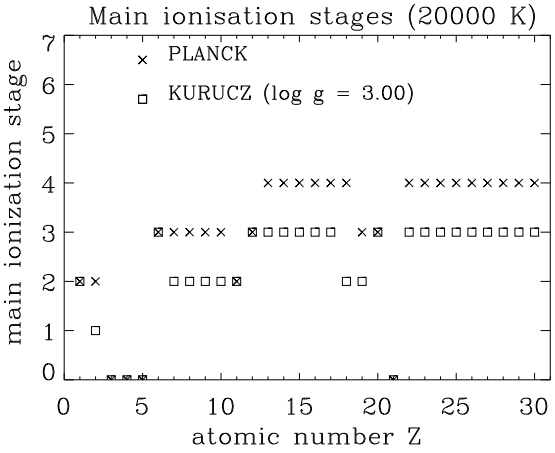

Fig. 6. Major ionization stages for illumination with black-body and Kurucz fluxes for $T_{\rm eff} = 20000$ K and $\log g = 3.0$.

fluxes in the EUV. As a consequence, lower ionization stages dominate for Kurucz irradiation.

As mentioned above, the considered line transitions are divided into three groups: resonance lines, lines with a meta-stable lower level and subordinate lines with a lower level leading directly to a ground or meta-stable level. An inspection of the contribution from these groups in the temperature range around 20000 K shows that the CNO group contributes most at small $\log t_{\rm S}$ via only a few resonance transitions and transitions to meta-stable levels, whereas the iron group dominates via numerous transitions to meta-stable levels at large $t_{\rm S}$ (cf. Abbott 1982 and Puls et al. 2000). Note that this behaviour of the different line groups is very similar for irradiation with Planck or line-blocked fluxes, respectively.

The properties of the force-multiplier can be summarized as follows: The force-multiplier mainly depends on the optical depth parameter $t_{\rm S}$ and the effective wind density $n_{\rm e}/W$. For fixed $n_{\rm e}/W$, M varies comparatively weakly with temperature

[5] With Eq. (26), we then have $M(t) = (v_{\rm therm}/c)(N_{\rm eff}/t)$. Thus, $N_{\rm eff}$ can be interpreted as the effective number of optically thick driving lines (cf. Abbott 1980, Eq. 8).

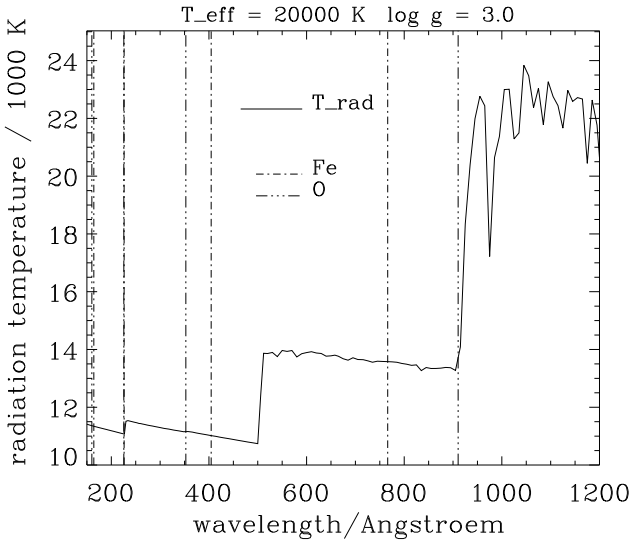

Fig. 7. Radiation temperature $T_{\rm rad}(\nu)$ for Kurucz fluxes at $T_{\rm eff}$ = 20000 K. We have marked the ionization energies of iron, FeV/VI (164.22 Å), FeIV/V (226.26 Å), FeIII/IV (404.53 Å), FeII/III (766.14 Å), and oxygen, OIV/V (160.16 Å), OIII/IV (225.64 Å), OII/III (352.67 Å), OI/II (910.44 Å).

(except in certain cases) and dilution factor W. For large $t_{\rm S}$ (i.e., high densities and/or small velocity gradients), numerous unsaturated transitions of the iron group elements (in particular, iron itself) dominate the line acceleration; for small $t_{\rm S}$ (i.e., low densities) a few strong resonance or quasi-resonance transitions (especially from the CNO group) are decisive. The contribution from subordinate lines has only minor impact in the temperature range considered here. (Those lines become more important for $T_{\rm eff} \gtrsim 40000$ K when the corresponding levels are stronger populated).

The *irradiation* of the wind material is crucial for the *ionization structure*: Since Kurucz flux distributions show a drastically reduced ionizing flux for wavelengths shortward of the Lyman edge, they give rise to systematically lower stages than in the black-body case. As a consequence, the force-multipliers are larger up to one order of magnitude.

In the first place, the *magnitude* of the force-multiplier is determined by the *ionization structure* present, rather than by the flux weighting factor F_ν/F. As numerous test calculations have shown, the differences in M are only marginal if one uses either Planck B_ν/B or Kurucz F_ν/F flux weighting factors, if one assumes identical *ionizing* fluxes in both cases. This fact will turn out to be of importance for our further proceeding of calculating consistent force-multiplier parameters, described in the next section.

6. The line force parameterization

Based on the properties of the force-multiplier M, we will develop now the parameterization of the line acceleration.

6.1. Minor simplifications

To this end and in order to reduce the computational effort, we adopt the simplifications described in the following.

In our approach, we neglect any diffuse radiation, i.e., we account only for the *direct* stellar radiation originating from the stellar surface. In a spherically-symmetric and radially expanding wind, the material around a specific location $\boldsymbol{r}$ *expands locally* into all directions. If we superimpose a differential rotation law to the radial expansion, we cannot exclude that the matter experiences a *compression* along certain directions $\boldsymbol{n}$, provided that the additional velocity components are large enough compared to the radial one. In such a case, a purely local formulation of the line acceleration may be questionable if there are non-local resonance points in the wind with zero projected velocity relative to $\boldsymbol{r}$. The set of all these resonance points forms the so-called *common point* (CP) resonance zone referring to $\boldsymbol{r}$ (cf. Rybicki & Hummer 1978).

If a ray pointing from the stellar surface to $\boldsymbol{r}$ intercepts this CP zone at $\boldsymbol{r}'$ before it hits $\boldsymbol{r}$, then the intensity changes (in Sobolev approximation) as $I_\nu^{\rm post} = I_\nu^{\rm pre} e^{-\tau_\nu(\boldsymbol{r}',\boldsymbol{n})} + S_{\rm L}(\boldsymbol{r}')\left(1-e^{-\tau_\nu(\boldsymbol{r}',\boldsymbol{n})}\right)$ (with the local source function $S_{\rm L}(\boldsymbol{r}')$). Consequently, the purely local expression for the line force (Eq. 24) has to be replaced by a formulation of radiative transfer that accounts for the influence of non-local processes (see Rybicki & Hummer 1978, Mazzali 1990).

However, a parameter study performed by Petrenz (1994) has clarified that such CP resonance zones may arise in rotating winds only for very shallow radial expansion laws combined with extreme rotation rates ($v_{\rm rot} \gtrsim 0.5\, v_\infty$). Even then, the CP zones subtend only a minor part of $\Omega_{\rm c}$. Therefore, the local description of the radiative transfer is a fairly good approximation and we assume the incident intensity $I_\nu^{\rm c}(\boldsymbol{r},\boldsymbol{n}')$ ($\boldsymbol{n}' \in \Omega_{\rm c}$) to depend only on the physical conditions on the stellar surface. For our test calculations, the radiation field at location $\boldsymbol{r}$ on the surface follows either a black-body law (with $T_{\rm eff} \equiv T_{\rm eff}(\Theta_*)$, see Sect. 3.1) or is taken from a model flux distribution (corresponding to the local values of $T_{\rm eff}(\Theta_*)$ and $\log g(\Theta_*)$).

In principle, one might also consider the rotational Doppler shift of the photospheric spectrum when calculating $I_\nu^{\rm c}(\boldsymbol{r},\boldsymbol{n}')$. However, this shift has significant values only close to the equatorial plane and majorly leads to a moderate broadening of ionization edges in the ionizing flux. This in turn might cause a small change in the ionization balance. The computational effort required for this exact description, however, is considerable, and we will neglect this secondary effect. In the same spirit, we neglect the directional dependence of $I_\nu^{\rm c}(\boldsymbol{r},\boldsymbol{n}')$ resulting from limb darkening.

In our time-dependent 2-D simulations, the local force-multiplier parameters $k_{\rm CAK}(\boldsymbol{r})$, $\alpha(\boldsymbol{r})$, $\delta(\boldsymbol{r},)$ are repeatedly updated in the course of the hydrodynamic evolution to guarantee their convergence consistently with the flow. At every co-latitude Θ of the hydrodynamic grid, this procedure requires the force-multipliers M to be calculated at a certain number (≈ 10) of radial grid points $\boldsymbol{r}_{\rm SG} = (\Theta, r_{\rm SG})$ (SG = "subgrid", see below). These values have to be determined

before every update of $k_{\rm CAK}$, α, δ. Despite our simplified NLTE formalism, the computation of the sum in Eq. 26 for such a large number of grid points would be very cumbersome. Therefore, we determine the force-multipliers $M(\boldsymbol{r}')$ by interpolation on tables which cover the parameter space of maximum width $[\overline{T}_{\rm eff\,min}, \overline{T}_{\rm eff\,max}] \times [\log t_{\rm S\,min}, \log t_{\rm S\,max}] \times [\log(n_{\rm e}/W)_{\rm min}, \log(n_{\rm e}/W)_{\rm max}] \times [W_{\rm min}, W_{\rm max}]$ (with effective temperatures $\overline{T}_{\rm eff}$ as defined further below). Once computed, these force-multiplier tables can be employed for any other or additional time-dependent hydrodynamic simulation.

6.2. Quantities of the radiation field

According to Eq. 26, the force-multiplier $M(\boldsymbol{r})$ depends on several quantities related to the radiation field: Firstly, on the ionizing flux $\boldsymbol{F}_\nu$ and secondly on the line strengths $k_{\rm L}$. $\boldsymbol{F}_\nu$ is a *direction-weighted* vector quantity, $\boldsymbol{F}_\nu = \int_{\Omega_{\rm c}} I^{\rm c}_\nu(\boldsymbol{r},\boldsymbol{n})\boldsymbol{n}\,{\rm d}\Omega$, whereas the line strengths $k_{\rm L}$ depend implicitly – via occupation numbers – on the mean intensity $J_\nu = (1/4\pi)\int_{\Omega_{\rm c}} I^{\rm c}_\nu\,{\rm d}\Omega$, which is an *angle-weighted* scalar. Both $\boldsymbol{F}_\nu(\boldsymbol{r})$ and $J_\nu(\boldsymbol{r})$ depend on radiation temperatures $T_{\rm rad}(\Theta_*(\boldsymbol{r},\boldsymbol{n}'))$ ($\boldsymbol{n}' \in \Omega_{\rm c}$) at the stellar surface. With present computational capacities, a simultaneous exact integration of $\boldsymbol{F}_\nu$ and J_ν over solid angle and frequency is not possible. Since we have seen that it is the frequency dependence of $T_{\rm rad}$ which is crucial for the resulting force-multipliers (cf. Sect. 5), we have to account for this dependence at least in an appproximate way. To this end, we will define below *angle-averaged, frequency-independent* effective temperatures, at every location $\boldsymbol{r}$.

For these averaged effective temperatures (which can be regarded to represent different atmospheric models), we take the according flux distributions from a grid of plane-parallel Kurucz fluxes (as function of $T_{\rm eff}$), which, in course, finally provide the *frequency-dependent* radiation temperatures $T_{\rm rad}(\boldsymbol{r},\nu)$ required to establish the local ionization structure. [6]

6.2.1. Radiation temperatures for black-body irradiation

Before we define the mean effective temperatures mentioned before, we investigate how strongly the radiation temperature varies throughout the wind if the stellar surface emits as a black-body. Neglecting limb darkening, we can simultaneously account for the dependence of $I^{\rm c}_\nu(\boldsymbol{r},\boldsymbol{n}') = B_\nu[T_{\rm rad}(\Theta_*(\boldsymbol{r},\boldsymbol{n}'))]$ on $\boldsymbol{n}'$ *and* ν: In this case, the mean intensity

$$J_\nu(\boldsymbol{r}) = \frac{1}{4\pi}\int\limits_{\boldsymbol{n}'\in\Omega_{\rm c}} B_\nu[T_{\rm rad}(\Theta_*(\boldsymbol{r},\boldsymbol{n}'))]\,{\rm d}\Omega \equiv W B_\nu(\overline{T}_{\rm rad}(\boldsymbol{r},\nu)) \quad (32)$$

[6] This approach (one flux distribution for one *mean* effective temperature $\overline{T}_{\rm eff}(\boldsymbol{r})$) allows the corresponding force-multipliers to be interpolated from a *model-independent* table (cf. Sect. 6.1), in contrast to the case of an exact procedure.

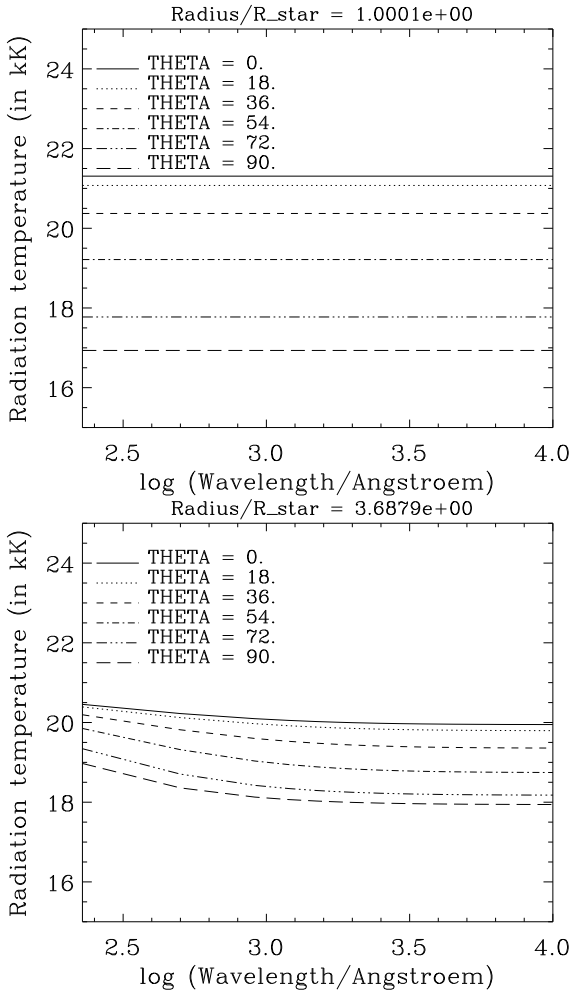

Fig. 8. Averaged radiation temperatures $\overline{T}_{\rm rad}(\boldsymbol{r},\nu)$ for a rapidly rotating B2 main-sequence star with $T_{\rm eff} = 20000$ K, $v_{\rm rot} = 350$ km s^{-1} and black-body surface at two radii ($r = R_*(\Theta)$, $r = 3.68\,R_*(\Theta)$). Stellar oblateness and gravity darkening based on the von Zeipel law have been considered. Other relevant parameters are $v_{\rm crit} = 486$ km s^{-1}, $R_{\rm eq}/R_{\rm p} = 1.21$, effective temperature at the pole $T_{\rm eff,p} = 21300$ K and at the equator $T_{\rm eff,eq} = 16940$ K, polar gravity $\log g_{\perp,{\rm p}} = 4.11$ and normal gravity at the equator $g_{\perp,{\rm eq}} = 3.71$.

provides the radiation temperature $\overline{T}_{\rm rad}(\boldsymbol{r},\nu)$ averaged over $\Omega_{\rm c}$:

$$\overline{T}_{\rm rad}(\boldsymbol{r},\nu) = \frac{h\nu}{k_{\rm B}}\frac{1}{\ln\left(1+(2h\nu^3\,W/(c^2 J_\nu)\right)} \quad (33)$$

J_ν can be computed numerically via Eq. 32, with $T_{\rm rad}\,(\Theta_*(\boldsymbol{r},\boldsymbol{n}')) = T_{\rm eff}(\Theta_*(\boldsymbol{r},\boldsymbol{n}'))$. For the model of a rapidly rotating B2 dwarf (corresponding to the "S-350" model discussed by OCB), Fig. 8 displays the frequency dependence of $\overline{T}_{\rm rad}(\boldsymbol{r},\nu)$ for two representative radii r at different co-latitudes Θ. At the stellar surface ($r \approx R_*$), the mean intensity J_ν is determined entirely by local conditions with radiation temperature independent of frequency, given by $T_{\rm eff}(\Theta = \Theta_*)$. For larger distances, different surface elements covering a wider temperature range contribute to J_ν. In consequence, $\overline{T}_{\rm rad}$ decreases over the poles because cooler regions near the equator contribute to the

radiation field, and, vice versa, $\overline{T}_{\rm rad}$ increases over the equator. Simultaneously, the difference of $\overline{T}_{\rm rad}(\Theta)$ for different Θ becomes smaller.

$\overline{T}_{\rm rad}$ varies only weakly with frequency, even in the short wavelength range where the sum of the different local Wien law emissions causes a slight increase of $\overline{T}_{\rm rad}$. For large λ, B_ν follows the Rayleigh-Jeans law, and $\overline{T}_{\rm rad}$ does not longer vary with wavelength.

6.2.2. Mean effective temperatures

In the following, we will account for the simultaneous dependence of $I^{\rm c}_\nu(\boldsymbol{r},\boldsymbol{n}')$ on physical properties of the stellar surface (i.e. at $(\Theta_*(\boldsymbol{r},\boldsymbol{n}'))$) and on frequency ν in an approximate way.

Our method uses quantities depending either on the angle-weighted mean intensity J_ν (for calculating ionization structure, occupation numbers) or on the direction-weighted radiative flux $\boldsymbol{F}_\nu$ (for calculating force-multipliers). To describe the frequency dependence of $J_\nu(\boldsymbol{r})$ and $F_\nu(\boldsymbol{r})$, respectively, we define two different effective temperatures being independent of frequency, in the spirit of our introductory remarks above.

1. According to Eq. 26, the force-multiplier M is a flux-weighted quantity with factor $\nu F_\nu/F$, which is finally absorbed in the force-multiplier parameter $k_{\rm CAK}$ (see Eq. 46).

If the radiative flux $F_\nu(\boldsymbol{r}) \equiv |\boldsymbol{F}_\nu(\boldsymbol{r})|$ is taken from a model atmosphere flux distribution, the latter should correspond to a local "continuum effective temperature" $\overline{T}_{\rm eff,cont}$ which ensures that the total flux given by the flux distribution, $F(\boldsymbol{r}) = \int_{\nu=0}^{\infty} F_\nu(T=\overline{T}_{\rm eff,cont})\mathrm{d}\nu$, equals the stellar flux given by integration over $\Omega_{\rm c}$. In other words, the definition of $\overline{T}_{\rm eff,cont}(\boldsymbol{r})$ should follow from *radiative flux conservation in* $\boldsymbol{r}$. Thus we have on the one side

$$\begin{aligned} F(\boldsymbol{r}) \;&=\; |\boldsymbol{F}(\boldsymbol{r})| = \left| \int\limits_{\boldsymbol{n}'\in\Omega_{\rm c}} \int\limits_{0}^{\infty} B_\nu[T_{\rm rad}(\Theta_*(\boldsymbol{r},\boldsymbol{n}'),\nu)]\mathrm{d}\nu\,\boldsymbol{n}'\,\mathrm{d}\Omega \right| \\ &=\; \left| \frac{\sigma_{\rm B}}{\pi} \int\limits_{\boldsymbol{n}'\in\Omega_{\rm c}} T^4_{\rm eff}(\Theta_*(\boldsymbol{r},\boldsymbol{n}'))\boldsymbol{n}'\,\mathrm{d}\Omega \right| \\ &\equiv\; \left| \int\limits_{\boldsymbol{n}'\in\Omega_{\rm c}} \boldsymbol{n}'\,\mathrm{d}\Omega \right| \frac{\sigma_{\rm B}}{\pi}\,\overline{T}^4_{\rm eff,cont} \quad . \end{aligned} \tag{34}$$

(Note the *vector* character of $\boldsymbol{F}(\boldsymbol{r})$ = $\boldsymbol{F}(\Theta, r)$, which guarantees that $\boldsymbol{F}$ is oriented perpendicularly to the stellar surface, thus having both a radial and a non-vanishing polar component.)

On the other side, frequency integration of the local photospheric flux distribution on the stellar surface, $F_\nu(\Theta_*)$, yields the local radiative flux $F(\Theta_*(\boldsymbol{r},\boldsymbol{n}')) = \sigma_{\rm B}T^4_{\rm eff}(\Theta_*(\boldsymbol{r},\boldsymbol{n}'))$. Comparing both sides, we obtain the desired effective temperature $\overline{T}_{\rm eff,cont}(\boldsymbol{r})$

$$\overline{T}_{\rm eff,cont}(\boldsymbol{r}) \;=\; \left\{ \left| \int_{\boldsymbol{n}'\in\Omega_{\rm c}} \boldsymbol{n}'\,\mathrm{d}\Omega \right|^{-1} \left| \int\limits_{\boldsymbol{n}'\in\Omega_{\rm c}} T^4_{\rm eff}(\Theta_*(\boldsymbol{r},\boldsymbol{n}'))\,\boldsymbol{n}'\,\mathrm{d}\Omega \right| \right\}^{1/4} , \tag{35}$$

which can be easily calculated in dependence on the surface deformation. For constant surface temperature, $\overline{T}_{\rm eff,cont}(\boldsymbol{r}) = T_{\rm eff}$, of course.

2. In a slightly different way, we address the question for the flux distribution providing the radiation temperatures $T_{\rm rad}(\boldsymbol{r},\nu)$ which determine ionization structure (Eq. 30) and occupation numbers (line strengths $k_{\rm L}$). The crucial quantity here is the angle-weighted mean intensity J_ν.

In analogy to $\overline{T}_{\rm eff,cont}$, the effective temperature for the ionizing flux distribution should follow from averaging the surface temperatures $T_{\rm rad}(\Theta_*(\boldsymbol{r},\boldsymbol{n}'),\nu)$ over $\Omega_{\rm c}$.

$\overline{T}_{\rm eff,cont}$ followed from the requirement of flux conservation, by averaging the fourth power of the stellar surface temperature $T_{\rm eff}(\Theta_*(\boldsymbol{r},\boldsymbol{n}'))$. In contrast to F, J_ν is a *frequency-dependent* quantity, and the local radiation temperature $T_{\rm rad}(\Theta_*(\boldsymbol{r},\boldsymbol{n}'),\nu)$ should depend differently on frequency at various co-latitudes Θ_*, in particular, if the stellar surface does not emit a black-body spectrum.

With $J_\nu(\boldsymbol{r}) = \int_{\boldsymbol{n}'\in\Omega_{\rm c}} I^{\rm c}_\nu(\boldsymbol{r},\boldsymbol{n}')\mathrm{d}\Omega$, we can at first define an average temperature $\overline{T}_{\rm rad}(\boldsymbol{r},\nu)$,

$$B_\nu(\overline{T}_{\rm rad}(\boldsymbol{r},\nu)) \equiv \frac{1}{\hat{\Omega}_{\rm c}} \int\limits_{\boldsymbol{n}'\in\Omega_{\rm c}} B_\nu(T_{\rm rad}(\Theta_*(\boldsymbol{r},\boldsymbol{n}'),\nu))\mathrm{d}\Omega, \tag{36}$$

with $\hat{\Omega}_{\rm c}$ from Eq. 29. Requiring the conservation of radiative flux $F = \int_{\nu=0}^{\infty} F_\nu \mathrm{d}\nu$ yields the local effective temperature $\overline{T}_{\rm eff,occ}(\boldsymbol{r})$:

$$F(\boldsymbol{r}) = \pi \int\limits_{\nu=0}^{\infty} B_\nu(\overline{T}_{\rm rad}(\boldsymbol{r},\nu))\mathrm{d}\nu \equiv \sigma_{\rm B}\overline{T}^4_{\rm eff,occ}(\boldsymbol{r})\,. \tag{37}$$

If we insert now the expression for $B_\nu(\overline{T}_{\rm rad}(\boldsymbol{r},\nu))$ (Eq. 36) into Eq. (37) and change the order of integration over Ω and ν, we find

$$\sigma_{\rm B}\overline{T}^4_{\rm eff,occ} = \frac{1}{\hat{\Omega}_{\rm c}} \int\limits_{\Omega_{\rm c}} \left\{ \int\limits_{0}^{\infty} \mathrm{d}\nu\, B_\nu(T_{\rm rad}(\Theta_*(\boldsymbol{r},\boldsymbol{n}'),\nu)) \right\} \mathrm{d}\Omega \tag{38}$$

The integration over ν on the RHS of Eq. (38) yields $(\sigma_{\rm B}/\pi)$ $T^4_{\rm eff}$ $(\Theta_*(\boldsymbol{r},\boldsymbol{n}'))$. Thus, the effective temperature $\overline{T}_{\rm eff,occ}(\boldsymbol{r})$ reads

$$\overline{T}_{\rm eff,occ} = \left[\frac{1}{\hat{\Omega}_{\rm c}} \int\limits_{\boldsymbol{n}'\in\Omega_{\rm c}} T^4_{\rm eff}(\Theta_*(\boldsymbol{r},\boldsymbol{n}'))\mathrm{d}\Omega \right]^{1/4} . \tag{39}$$

In contrast to the direction-weighted temperature $\overline{T}_{\rm eff,cont}$, we have to integrate over $\mathrm{d}\Omega$ rather than over $\boldsymbol{n}'\mathrm{d}\Omega$, due do the different angular weighting process inherent to mean intensity and flux, respectively. Fig. 9 displays both effective temperatures, $\overline{T}_{\rm eff,cont}$ and $\overline{T}_{\rm eff,occ}$, and their difference for the above

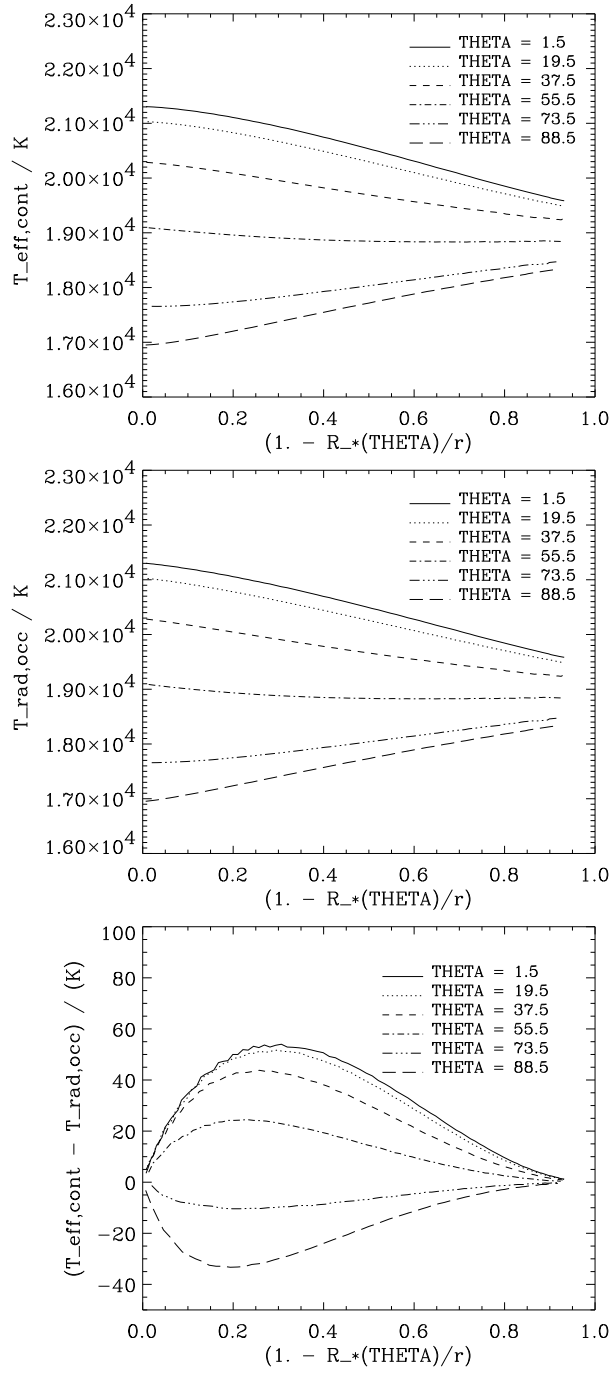

Fig. 9. Mean effective temperatures $\overline{T}_{\rm eff,cont}$ and $\overline{T}_{\rm eff,occ}$ for the same model as in Fig. 8. Top panel: averaged continuum effective temperature $\overline{T}_{\rm eff,cont}$; middle panel: averaged effective temperature $\overline{T}_{\rm eff,occ}$; bottom panel: difference $\overline{T}_{\rm eff,cont} - \overline{T}_{\rm eff,occ}$.

B2 dwarf model. Primarily, both quantities are a function of co-latitude Θ. For $r \approx R_*$, they are identical since they depend on purely local conditions, with $\overline{T}_{\rm eff,cont} = \overline{T}_{\rm eff,occ} = T_{\rm eff}(\Theta_*)$. For larger radii r, the polar wind is illuminated by additional cooler surface elements and both $\overline{T}_{\rm eff,cont}$ and $\overline{T}_{\rm eff,occ}$ drop (and vice versa for the equator). As for the black-body case (Sect. 6.2.1), even for large distances from the surface the mean radiation field remains strongly affected by the physical conditions at the foot point $(\Theta_*, R_*(\Theta_*))$: An easy geometrical consideration shows that no radiation exactly from the pole contributes at locations in the equatorial plane and that the polar wind remains unaffected from equatorial radiation.

Compared to their variation with co-latitude, the difference between $\overline{T}_{\rm eff,cont}$ and $\overline{T}_{\rm eff,occ}$ is surprisingly small. Its order of magnitude can be easily checked, if one assumes a spherical stellar surface and a linear dependence on μ,

$$T_{\rm eff}(\mu) \;=\; T_{\rm eff}(\mu=1) + (\Delta T/\Delta\mu)(\mu-1)/(\mu_*-1)\,, \quad (40)$$

which is justified by Fig. 9 (top and middle panel).

E.g., over the pole ($\Theta = 0$) at $r = 1.5\,R_*$ we obtain $\overline{T}_{\rm eff,occ} = \int_{\mu_*}^1 T_{\rm eff}(\mu){\rm d}\mu / \int_{\mu_*}^1 {\rm d}\mu$ = 42450 K and $\overline{T}_{\rm eff,cont} = \int_{\mu_*}^1 T_{\rm eff}(\mu)\mu{\rm d}\mu / \int_{\mu_*}^1 \mu{\rm d}\mu$ = 42560 K. Thus, the difference between both temperatures has the same order of magnitude as the exact numerical result, and $\overline{T}_{\rm eff,cont}$ slightly exceeds $\overline{T}_{\rm eff,occ}$.

For intermediate radii, the direction-weighted temperature $\overline{T}_{\rm eff,cont}$ is slightly more influenced by the local temperature at the surface point $(\Theta, R_*(\Theta))$ (respectively, by the temperature at neighbouring surface elements, since the surface is not entirely spherical). Thus, $\overline{T}_{\rm eff,cont}$ is larger (smaller) than the angle-weighted quantity $\overline{T}_{\rm eff,occ}$ over the poles (in the equatorial plane). The larger r, the more the radiation field becomes radial, and the difference between both temperatures vanishes.

The fact that these effective temperatures vary much stronger with co-latitude Θ than with distance r justifies also our concept of a representative illuminating flux distribution taken for a mean effective temperature: In $\boldsymbol{r} = (\Theta, r)$, this flux distribution is in accordance with a spectrum at least similar to the emission at $(\Theta, R_*(\Theta))$.

The flux distribution is a function not only of effective temperature $T_{\rm eff}$, but also of gravity $\log g$. Since the Kurucz fluxes depend only weakly on the variations of $\log g$ we are interested in, we take, for all $\boldsymbol{r}$ in the wind, the surface-averaged value $\log g \equiv \log g_\perp^{\rm av}$ (PP96, Eq. 30).

6.2.3. The dilution factor

Owing to stellar oblateness, the dilution factor W (Eq. 29) becomes a function not only of r but also of Θ. Fig. 10 displays the ratio $W/W_{1-\rm D}$ ($W_{1-\rm D}$ from Eq. 22) for our B2-dwarf model. $W_{1-\rm D}$ is normalized to the *polar* radius $R_{\rm p}$.

For all Θ, $R_*(\Theta)$ is greater or equal $R_{\rm p}$, and W always exceeds $W_{1-\rm D}$. Due to oblateness, this discrepancy between W and $W_{1-\rm D}$ is largest close to the star with the maximum effect in the equatorial plane. The radial variation of $W/W_{1-\rm D}$ for constant Θ is caused both by curvature and asphericity of the stellar surface.

Over the poles, the surface curvature is weaker than in the spherical case (see Collins 1963, Fig. 1). Therefore, the solid angle $\Omega_{\rm c}$ always exceeds the value for a spherical star with $R_* = R_{\rm p}$ (except for $\Theta = 0, r = R_{\rm p}$). For larger r, $\Omega_{\rm c}$ grows compared to the spherical value, due to the enlarged surface.

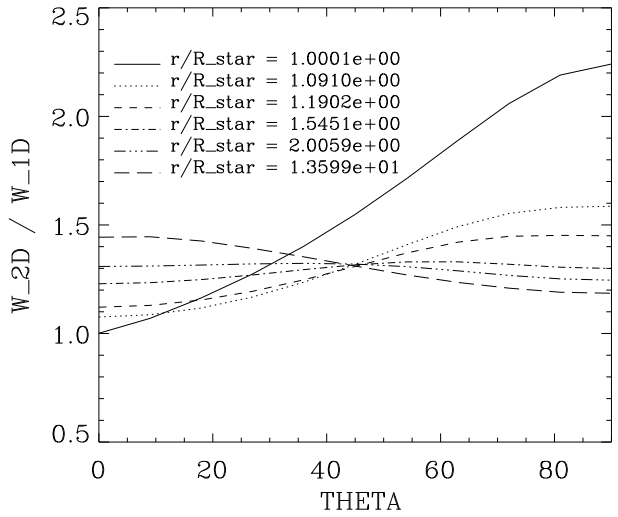

Fig. 10. The ratio $W/W_{1-\mathrm{D}}$ for the B2-star from Fig. 8 with $T_{\mathrm{eff}} = 20000$ K, $v_{\mathrm{rot}} = 350$ km s^{-1}, at different radii r and co-latitudes Θ.

At the equator, the surface curvature is stronger than in the spherical case, and the significant discrepancy between W and $W_{1-\mathrm{D}}$ for $R_*(\Theta = \pi/2)$ decreases for larger r.

Far away from the star, the solid angle subtended by the stellar disk observed equator-on is smaller than viewed pole-on. In the latter case, one looks upon a rotationally-symmetric object with the same maximum extent for all azimuthal angles φ (cf. Fig. 1).

As Fig. 10 clarifies, the difference between W and $W_{1-\mathrm{D}}$ only marginally exceeds a factor of 2. With respect to the weak dependence of the force-multiplier M on W (see Sect. 5), this difference is not relevant for qualitative studies.

6.3. Depth-dependent force-multiplier parameterization

Fig. 3 and 4 show a clearly non-linear dependence of the force-multiplier $\log M$ on $\log t_{\mathrm{S}}$ and $\log(n_{\mathrm{e}}/W)$. The physical reason for this is, on the one hand, that the approximation of the line distribution function by a power law with constant exponent α is not entirely sufficient. As shown by Puls et al. (2000), α varies systematically as function of line strength k_{L}, thus implying a curvature of $M(t_{\mathrm{S}})$ as function of t_{S}. On the other hand, the exponent δ depends also on the ionization structure, and, as a consequence, $\log M$ becomes a non-linear function of $\log(n_{\mathrm{e}}/W)$.

Because of this non-linear behaviour, the classical fit with global k_{CAK}, α, δ may lead to severe discrepancies between the fit values M_{param} and the actual force-multipliers M (see Kudritzki et al. 1998, hereafter Ku98, Fig. 5).

For this reason, Ku98 proposed an improved parameterization of the force-multiplier, using the most simple fit formula of higher order for $\log M$ which allows for a linear dependence of α and δ on $\log t_{\mathrm{S}}$ and $\log(n_{\mathrm{e}}/W)$,

$$\log M(t_{\mathrm{S}}, n_{\mathrm{e}}/W) = \log k_0 - \alpha \log t_{\mathrm{S}} + \delta \log \hat{n} \quad (41)$$

$$\alpha = \alpha_0(1 + \alpha_1 \log t_{\mathrm{S}}) \quad (42)$$

$$\delta = \delta_0(1 + \delta_1 \log \hat{n}) + \gamma_0 \log t_{\mathrm{S}} \ , \quad (43)$$

with $\hat{n} = 10^{-11}(n_{\mathrm{e}}/W)$ and k_0 corresponding to the CAK parameter k_{CAK}. The fit is performed via the least-square solution of the over-determined system of linear equations for the unknown k_0, α_0, α_1, δ_0, δ_1, γ_0:

$$\begin{aligned} \log M(t_{\mathrm{S}i}, \hat{n}_j) &= \log k_0 - \alpha(t_{\mathrm{S}i}) \log t_{\mathrm{S}i} \\ &+ \delta(t_{\mathrm{S}i}, \hat{n}_j) \log(\hat{n}_j), \\ &(i \in 1 \ldots N_t, j \in 1 \ldots N_{\hat{n}}), \end{aligned} \quad (44)$$

with N_t, $N_{\hat{n}}$ the number of input points of $\log t_{\mathrm{S}}$ and $\log(n_{\mathrm{e}}/W)$, respectively.

As shown by Ku98, this parameterization provides fits of the force-multipliers with errors smaller than $\lesssim 0.1$ dex in $\log M$, where those fits cover completely the ranges in $\log t_{\mathrm{S}}$ and $\log(n_{\mathrm{e}}/W)$ relevant for the corresponding spectral type of the star.

Since we will determine the parameters k_{CAK}, α, δ in our hydrodynamic simulations by means of Eq. 41 – 43, we have to check how well these values agree with the actual ones, i.e., those obtained by a piecewise differentiation of $\log M$ with respect to $\log t_{\mathrm{S}}$ and $\log(n_{\mathrm{e}}/W)$, respectively. For some typical cases, Fig. 11 demonstrates that the new parameterization reproduces α and δ in the correct order of magnitude and also succeeds in a qualitative reproduction of δ as function of $\log t_{\mathrm{S}}$.

At this point of reasoning, the obvious question arises why we employ this particular method to determine k_{CAK}, α, δ instead of deriving them directly by piecewise differentiation of M, moreover since the latter method yields results with higher precision. Briefly, there are two reasons:

(1) During the hydrodynamic evolution of the flow, one does not know a priori whether the *momentary* local values of k_{CAK}, α, δ will guarantee hydrodynamic stability for *subsequent* time steps. Since local variations of t_{S} by two orders of magnitudes are quite possible (e.g., if a disturbance propagates through the wind), one needs a *globally* valid description for k_{CAK}, α, δ which covers the *entire range of possible values* for t_{S} and n_{e}/W.

(2) Secondly, the line acceleration $\boldsymbol{g}^{\,\mathrm{lines}}(\boldsymbol{r})$ can vary drastically on relatively small spatial scales due to strong variations of $M(\boldsymbol{r})$ and the corresponding force-multiplier parameters α and δ if a piecewise differentiation of M is employed. This lack of a "smooth" acceleration may cause severe disturbances of the flow and prevent the flow from converging to its stationary solution. Test calculations, both for 1-D and 2-D winds, have confirmed this behaviour.

If, on the other hand, we formulate $\boldsymbol{g}^{\,\mathrm{lines}}$ by means of globally fitted parameters as described above, we avoid these problems, of course at the expense of variations in α and δ not reproduced very precisely (cf. Fig. 11). This lack of precision results from our approximation of using only linear functions in $\log t_{\mathrm{S}}$ and $\log(n_{\mathrm{e}}/W)$ for α and δ, respectively, and from the notion that the fit procedure has to cover a relatively broad range in $\log t_{\mathrm{S}}$ and $\log(n_{\mathrm{e}}/W)$.

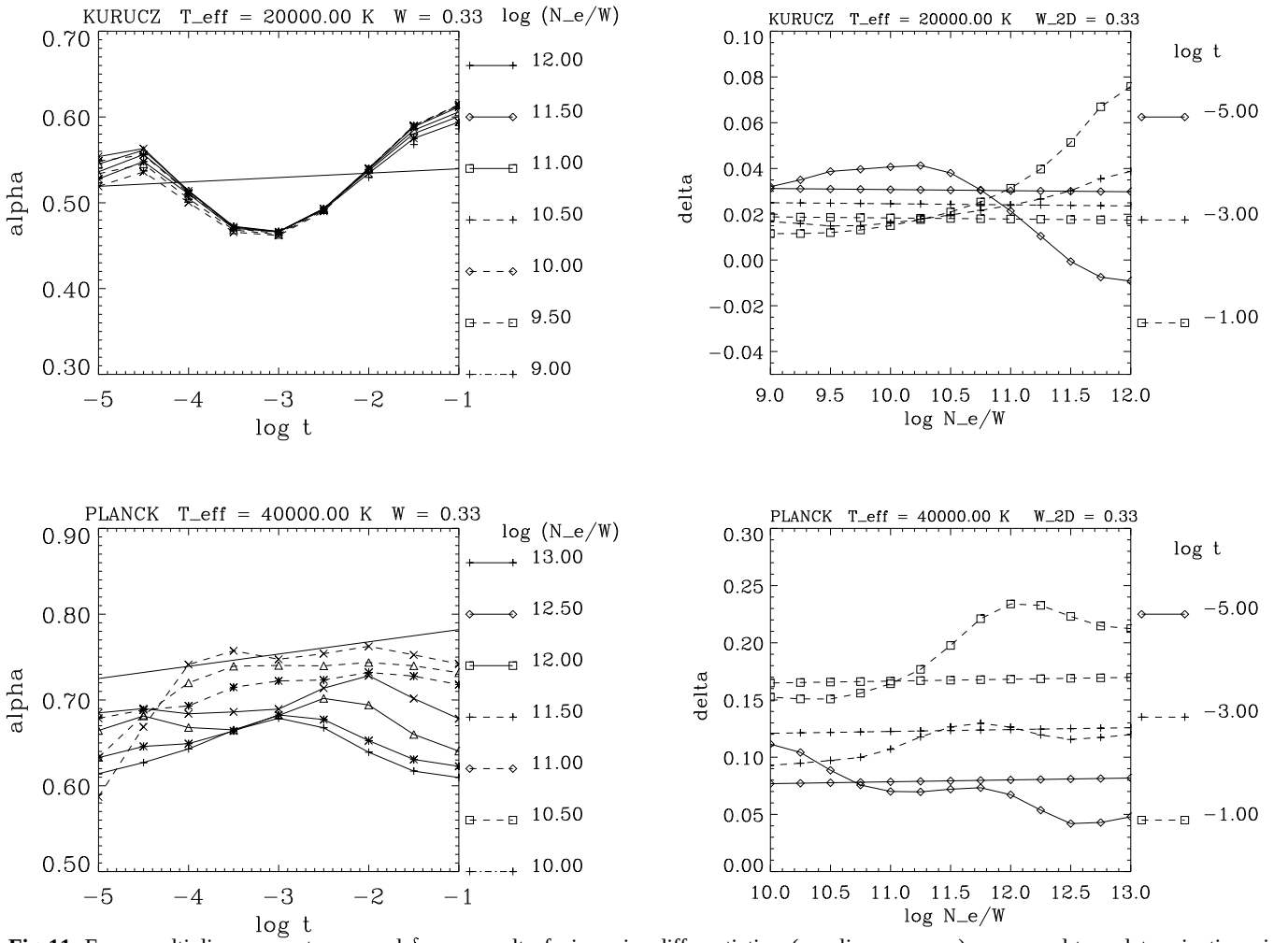

Fig. 11. Force-multiplier parameters α and δ as a result of piecewise differentiation (non-linear *curves*), compared to a determination via Eqs. 42/43 (*linear* functions, being degenerate for $\alpha = \alpha(t_{\rm S})$). Top panel: $T_{\rm eff}$ = 20000 K, irradiation by Kurucz flux distribution ($\log g$ = 3.0); bottom panel: $T_{\rm eff}$ = 40000 K, Planck fluxes.

As pointed out already above, however (see Ku98), the multiplication of the three factors $k_{\rm CAK}$, $t_{\rm S}^{-\alpha}$ and $\hat{n}^{\delta}$ finally yields a good reproduction of the force-multiplier itself: On the average, local discrepancies in α and δ are compensated by the fit value of $k_{\rm CAK}$. Fig. 13 clearly demonstrates this behaviour.

The actual procedure to determine $k_{\rm CAK}\,(\boldsymbol{r})$, $\alpha(\boldsymbol{r})$ and $\delta(\boldsymbol{r})$ in our hydrodynamical simulations is described in the next section. By means of these quantities then, the line acceleration

$$\boldsymbol{g}^{\rm lines} \sim k_{\rm CAK}(\boldsymbol{r})\hat{n}^{\delta(\boldsymbol{r})} \int_{\boldsymbol{n}'\in\Omega_{\rm c}} t_{\rm S}(\boldsymbol{r},\boldsymbol{n}')^{-\alpha(\boldsymbol{r})}\,\boldsymbol{n}'{\rm d}\Omega$$

is calculated. Inaccurately determined values of α may lead to a biased direction-weighting of the contributions $t_{\rm S}(\boldsymbol{r},\boldsymbol{n}')^{-\alpha}$, if $t_{\rm S}$ varies strongly as function of $\boldsymbol{n}'$. In our 2-D approach, however, we will restrict ourselves to this conceptionally simple representation of the force-multiplier parameters, especially in view of problem (**2**) discussed above.

As an obvious advantage, our parameterization is *consistent for all spectral types* and requires *minimum computational effort* during the hydrodynamic calculation. In particular – and contrasted to previous 2-D approaches (models by BC and Owocki and collaborators, restricted to constant line-force parameters) – it allows for a quantitatively reasonable description of the line force that accounts both for *local* physical conditions and the *non-local* stellar radiation field.

6.4. Local line force parameterization in 2-D winds

In the following, we generalize the parameterization introduced in Sect. 6.3 to 2-D winds from rotating stars, in particular accounting for the *polar gradient of the surface temperature* $T_{\rm eff}(\Theta_*(\boldsymbol{r},\boldsymbol{n}'))$ $(\boldsymbol{n}' \in \Omega_{\rm c})$. Considering the line acceleration (Eq. 24), the generalized expression obviously would read (cf. Sect. 3.2)

$$\boldsymbol{g}^{\rm lines}(\boldsymbol{r}) = \frac{s_{\rm E}}{c}\int\limits_{\Omega_{\rm c}} {\rm d}\Omega\,\boldsymbol{n}' I^{\rm c}(\boldsymbol{r},\boldsymbol{n}')k_{\rm CAK}(\boldsymbol{r},\boldsymbol{n}')$$
$$\times\left(\frac{n_{\rm e}(\boldsymbol{r})\cdot 10^{-11}}{W(\boldsymbol{r})}\right)^{\delta(\boldsymbol{r},\boldsymbol{n}')} \times\left(\frac{|\boldsymbol{n}'\cdot\nabla(\boldsymbol{n}'\boldsymbol{v})|}{s_{\rm E}\rho(\boldsymbol{r})v_{\rm therm}}\right)^{\alpha(\boldsymbol{r},\boldsymbol{n}')}, \quad (45)$$

with direction-dependent CAK parameter

$$k_{\rm CAK}(\boldsymbol{r},\boldsymbol{n}') = \frac{N_0 v_{\rm therm}}{c} \frac{\Gamma(\alpha(\boldsymbol{r},\boldsymbol{n}'))}{1-\alpha(\boldsymbol{r},\boldsymbol{n}')} \times \int_0^\infty {\rm d}\nu\, f_\nu(\nu)\,\nu \left(\frac{I^{\rm c}_\nu(\boldsymbol{r},\boldsymbol{n}')}{I^{\rm c}(\boldsymbol{r},\boldsymbol{n}')}\right) . \quad (46)$$

Since we neglect the dependence of the ratio $I^{\rm c}_\nu(\boldsymbol{r},\boldsymbol{n}')/I^{\rm c}(\boldsymbol{r},\boldsymbol{n}')$ on direction, we can replace this expression by the *average flux weighting* factor F_ν/F and extract $k_{\rm CAK}(\boldsymbol{r},\boldsymbol{n}')$ from the integral. Also $\alpha(\boldsymbol{r},\boldsymbol{n}')$ and $\delta(\boldsymbol{r},\boldsymbol{n}')$ are replaced by average values $\alpha(\boldsymbol{r})$, $\delta(\boldsymbol{r})$, so that the line force is finally given by

$$\boldsymbol{g}^{\rm lines}(\boldsymbol{r}) = \frac{s_{\rm E}}{c} k_{\rm CAK}(\boldsymbol{r}) \left(\frac{n_{\rm e}(\boldsymbol{r})\cdot 10^{-11}}{W(\boldsymbol{r})}\right)^{\delta(\boldsymbol{r})} \times \int\limits_{\boldsymbol{n}'\in\Omega_{\rm c}} {\rm d}\Omega\, \boldsymbol{n}' I^{\rm c}(\boldsymbol{r},\boldsymbol{n}') \left(\frac{|\boldsymbol{n}'\cdot\nabla(\boldsymbol{n}'\boldsymbol{v})|}{s_{\rm E}\rho(\boldsymbol{r})v_{\rm therm}}\right)^{\alpha(\boldsymbol{r})} . \quad (47)$$

This approximation – compared to the "exact" expression (Eq. 45) – can by justified as follows:

With respect to employing an average value for $k_{\rm CAK}$, we avoid otherwise severe problems with normalization, since the flux distribution F_ν/F will be taken at an effective temperature $\overline{T}_{\rm eff,cont}$ (Eq. 35) which ensures flux conservation in $\boldsymbol{r}$.

For δ, the formal dependence on direction is actually redundant, since δ parameterizes the force-multiplier as a function of ionization structure. The latter depends only on *isotropic* quantities, $n_{\rm e}(\boldsymbol{r})$ and $W(\boldsymbol{r})$, and we can extract the factor $\hat{n}^\delta$ from the angular integral. Thus, δ becomes a function of $\boldsymbol{r}$ only.

α describes the reaction of the force-multiplier on changes in $\log t_{\rm S}$. In the expression for $\boldsymbol{g}^{\rm lines}$ (Eq. 47), we integrate over different values of $t_{\rm S}(\boldsymbol{n}')$ as function of direction. The force-multiplier M is an explicit function of $t_{\rm S}$, and does not depend explicitly on any particular direction $\boldsymbol{n}'$. Therefore, the integral

$$\int_{\Omega_{\rm c}} I^{\rm c}(\boldsymbol{r},\boldsymbol{n}')\boldsymbol{n}' t_{\rm S}(\boldsymbol{n}')^{\alpha(\boldsymbol{r})}{\rm d}\Omega\,,$$

evaluated with a value of α that has been determined from *representative 1-D force-multipliers* (see below) constitutes a plausible approximation of the "exact" expression

$$\int_{\Omega_{\rm c}} I^{\rm c}(\boldsymbol{r},\boldsymbol{n}')\boldsymbol{n}' t_{\rm S}(\boldsymbol{n}')^{\alpha(\boldsymbol{r},\boldsymbol{n}')}{\rm d}\Omega,$$

with $\alpha(\boldsymbol{r})$ as an average value of the directional dependent quantities $\alpha(\boldsymbol{r},\boldsymbol{n}')$.

The actual (average) values of $k_{\rm CAK}(\boldsymbol{r})$, $\alpha(\boldsymbol{r})$, $\delta(\boldsymbol{r})$ are now calculated in the following way:

At first, we derive *local* force-multipliers

$$M(t_r) = (1/t_r)\sum_{\rm lines\ L}(\nu F_\nu/F)(1-\exp(-k_{\rm L}t_r))$$

(with *radial* depth parameter t_r) at typically 10...12 radial grid points $r_{\rm SG}$ and all co-latitudes Θ, which are a subset of the numerical 2-D hydro grid $\{\Theta_j, r_i\}$, with $r_{\rm SG}$ between $R_*(\Theta)$ and a maximum radius $r_{\rm max} \approx 6R_*(\Theta)$ (see also Sect. 7.1). This calculation bases on our approximate NLTE solution described in Sect. 4.

The radiation field for the flux weighting factor F_ν/F is given by the flux distribution at (direction averaged) effective temperature $\overline{T}_{\rm eff,cont}$ (Sect. 6.2.2), thus ensuring flux conservation in $\boldsymbol{r}$. The *ionizing* radiation field (decisive for ionization structure and line strengths $k_{\rm L}$) is taken for the angle-averaged effective temperature $\overline{T}_{\rm eff,occ}$ (Sect. 6.2.2), thus accounting for its crucial frequency-dependence. Since $\overline{T}_{\rm eff,cont}$ and $\overline{T}_{\rm eff,occ}$ are frequency-independent effective temperatures *locally* averaged over $\Omega_{\rm c}$, our model also accounts for the dependence of the radiation field on location.[7]

Therefore, the force-multipliers $M(\boldsymbol{r})$ determined in this way may be regarded as *representative* quantities (indirectly) averaged over $\Omega_{\rm c}$. Consequently, the according parameters (as function of $\boldsymbol{r}$ only) derived from these force-multipliers represent average values of the corresponding direction-dependent quantities $k_{\rm CAK}(\boldsymbol{r},\boldsymbol{n}')$ etc.

To save computational time, the $M(\boldsymbol{r})$ are interpolated from a *pre-calculated* table as function of $\overline{T}_{\rm eff,cont}(\boldsymbol{r}) \approx \overline{T}_{\rm eff,occ}(\boldsymbol{r})$, $W(\boldsymbol{r})$, $t_r(\boldsymbol{r},t)$ and $(n_{\rm e}/W)(\boldsymbol{r},t)$, with time t (cf. Sect. 6.1).

As shown in Fig. 9, $\overline{T}_{\rm eff,cont}$ and $\overline{T}_{\rm eff,occ}$ vary much weaker with radius r (for constant Θ) than with co-latitude Θ (for constant r). Thus, the anyhow weak temperature dependence of M (cf. Sect. 5) for constant Θ is negligible compared to its dependence on $\log t_{\rm S}$ and $\log(n_{\rm e}/W)$, respectively. In so far, it is sufficient to parameterize $\log M$ as a function of $\log t_r$ and $\log(n_{\rm e}/W)$ *along a radial ray at constant co-latitude* Θ.

For all Θ then, we determine the force multipliers $M(t_r)$ at the radial subgrid described above, and *additionally* the values $M(\log t_r(\boldsymbol{r}_{\rm SG}) + \Delta\log t_r,\ \log\hat{n}(\boldsymbol{r}_{\rm SG}) + \Delta\log\hat{n})$, with $\Delta\log\hat{n} = \pm 0.25, \pm 0.5 \ldots \pm (\Delta\log\hat{n})_{\rm max}$ and $\Delta\log t_r = \pm 0.5, \ldots \pm(\Delta\log t_r)_{\rm max}$. These additional force-multipliers allow us to include the possible range of the non-radial depth parameters $t_{\rm S}(\boldsymbol{r},\boldsymbol{n}' \neq \boldsymbol{e}_r)$.

By means of these M-values, we determine the six parameters $k_0(\Theta) = k_{\rm CAK}$, $\alpha_0(\Theta)$, $\alpha_1(\Theta)$, $\delta_0(\Theta)$, $\delta_1(\Theta)$, $\gamma_0(\Theta)$ *separately for every co-latitude* Θ via Eq. 44. Inserting these parameters into Eq. 42 and 43 provides $\alpha(\boldsymbol{r},t)$ and $\delta(\boldsymbol{r},t)$, which depend on time via $t_r(\boldsymbol{r},t)$ and $(n_{\rm e}/W)(\boldsymbol{r},t)$, and allows to calculate finally the line acceleration $\boldsymbol{g}^{\rm lines}(\boldsymbol{r},t)$ via Eq. 47.

During the temporal evolution of our simulations, the above procedure is repeated typically each 100 time steps Δt, for each co-latitude Θ.

With the local values of $M(\boldsymbol{r})$ as central values of the squares in the $\log t_r$-$\log\hat{n}$-subspace defined above, we force the fit range to be concentrated about the *actual* values of

[7] Since $\overline{T}_{\rm eff,cont}$ and $\overline{T}_{\rm eff,occ}$ differ by less than 1% of their absolute value (see Fig. 9), we do not discriminate between these two temperatures in our hydrodynamic simulations.

$\log t_r(\boldsymbol{r})$ and $\log \hat{n}(\boldsymbol{r})$, which are the only input quantities of our procedure that evolve with time (in contrast to the fixed quantities $\overline{T}_{\rm eff,cont}(\Theta, r) \approx \overline{T}_{\rm eff,occ}(\Theta, r)$ and $W(\Theta, r)$). Thus, the adaptation of the force-multiplier parameters to the flow becomes more consistent as if one determines a set of "global" values k_0, α_0 etc. for the *entire* range of possible $\log t_r$ and $\log \hat{n}$ *before* the simulation.

As extensive numerical tests have shown, satisfying fits of the force multipliers require a certain minimum width of the intervals $[-(\Delta \log t_r)_{\max}, +(\Delta \log t_r)_{\max}]$ and $[-(\Delta \log \hat{n})_{\max}, +(\Delta \log \hat{n})_{\max}]$. In particular, if the $\log t_r$ interval is too narrow, the errors in k_0, α_0 etc. may become much larger than the resulting parameters, and the resulting $k_{\rm CAK}(\boldsymbol{r})$, $\alpha(\boldsymbol{r})$ and $\delta(\boldsymbol{r})$ may obtain unphysical values, preventing a stable convergence of the flow. Empirically, we found a width of 1.5...2.0 (1.0...1.5) for the intervals in $\log t_r$ and $\log \hat{n}$, respectively.

6.5. Synopsis: Calculation of a consistent 2-D line force by means of the force-multiplier concept

At every co-latitude Θ, our procedure provides six constant parameters $k_0(\Theta)$, $\alpha_0(\Theta)$, $\alpha_1(\Theta)$, $\delta_0(\Theta)$, $\delta_1(\Theta)$, $\gamma_0(\Theta)$ by means of local force-multipliers $M(\boldsymbol{r})$ and the values on neighbouring coordinates in the $\log t_r$-$\log \hat{n}$ subspace. With these parameters, which are repeatedly updated in the course of the hydrodynamic evolution, directional independent values of $k_{\rm CAK}(\boldsymbol{r})$, $\alpha(\boldsymbol{r})$ and $\delta(\boldsymbol{r})$ are determined. These latter values parameterize the line acceleration $\boldsymbol{g}^{\rm lines}(\boldsymbol{r})$ and depend on the local, time-dependent quantities $\log t_r(\boldsymbol{r}, t)$ and $\log \hat{n}(\boldsymbol{r}, t)$.

Since the force-multipliers $M(\boldsymbol{r})$ are computed for flux distributions evaluated at local effective temperatures $\overline{T}_{\rm eff,cont}$ and $\overline{T}_{\rm eff,occ}$ averaged over $\Omega_{\rm c}$, the resulting force-multiplier parameters can be regarded as representative values averaged over $\Omega_{\rm c}$.

The primarily *polar* variation of $\overline{T}_{\rm eff,cont}$ and $\overline{T}_{\rm eff,occ}$ suggests a fit for k_0, α_0 etc. along radial rays for fixed co-latitudes Θ. It is obvious that the directional independent values of $\alpha(\boldsymbol{r})$ and $k_{\rm CAK}(\boldsymbol{r})$ may differ from the "exact" ones $\alpha(\boldsymbol{r}, \boldsymbol{n}')$ and $k_{\rm CAK}(\boldsymbol{r}, \boldsymbol{n}')$ for distinct directions $\boldsymbol{n}'$. However, this problem may occur only in intermediate wind regions, i.e., at locations where the incident radiation field originates from surface elements with different temperatures. For larger distances, the irradiation becomes radial and its representation by an adequate flux distribution is certainly reasonable. Close to the star, the incident intensity is characterized by purely local conditions. The only effect that would lead to a directional dependence is the rotational Doppler shift of the illuminating photospheric spectrum, which is a second order effect and neglected in our approach, as discussed in Sect. 6.1.

7. Self-consistent models

In this section, we present our numerical results for self-consistent wind models accounting for both the *local* physical conditions and the *non-local* ionizing radiation field, as described in Sect. 6.4. To clarify to what extent a self-consistent 2-D parameterization of the line force influences the physical signatures/quantities in the wind, we will differentially compare the properties of these new models with those following from more simple 1-D/2-D simulations using global values for $k_{\rm CAK}$, α, δ.

7.1. Numerical aspects and tests for 1-D models

While the models evolve to their stationary state, the force-multiplier parameters consistently adapt to the flow, implying an additional time-dependence of $\boldsymbol{g}^{\rm lines}(\boldsymbol{r})$, which is anyway a function of the hydrodynamic variables $\boldsymbol{v}(t)$, $\rho(t)$ and $[\boldsymbol{n} \cdot \nabla\,(\boldsymbol{n}\boldsymbol{v})](t)$. Since $k_{\rm CAK}$, α, δ are determined separately for every co-latitude Θ, they are coupled with all force-multipliers $M(\Theta = \text{const}, r)$ within the radial fit range. To facilitate flow convergence, the points of the radial mesh $(\Theta, r_{\rm SG})$ are distributed over a range $r_{\rm SG} = R_*(\Theta) \ldots 6\,R_*(\Theta)$.[8] After initial disturbances originating at the wind base have been advected to radii $r > 6\,R_*$, the force-multiplier parameters and thus the total force-multiplier relax to their stationary value.

The effective temperatures $\overline{T}_{\rm eff,cont}$ (Eq. 35) and the line force components $(g_\Theta^{\rm lines}, g_\Phi^{\rm lines}, g_r^{\rm lines})$ (Eq. 24) are determined (the latter ones for *every* time step) by a standard quadrature over 9×5 equidistant integration points in $\varphi \in [0, 2\pi] \times \vartheta \in [\vartheta_*, \pi]$. To avoid numerical inaccuracies in the outer wind region, it turned out that ϑ_* has to be fixed very accurately ($\Delta\vartheta_*/\vartheta_* \lesssim 10^{-5}$).

For $4 \cdot 10^6$ s physical evolution time (roughly 50 days), the computation of a self-consistent 2-D model typically required $\lesssim 100$ CPU hours on a 400 Mflops machine.

Model atmospheres. The flux distributions F_ν are taken from plane-parallel LTE Kurucz model atmospheres (Kurucz 1992), computed by N. Przybilla (Univ. Observatory, Munich). For our preferentially considered temperature range ($T_{\rm eff} \approx 20000$ K), these fluxes provide the presently best approximation (compromise flux-blocking/blanketing vs. NLTE), although for low gravities the grid becomes incomplete due to the problem of too large line accelerations, being inconsistent with the hydrostatic assumption inherent to those models. In such cases, we used the fluxes from a model atmosphere with the lowest value of $\log g$ possible for given $T_{\rm eff}$. Note, however, that this problem occurs only for very rapidly rotating supergiants (low $\log g$ and high temperatures over the poles).

1-D models. In a first step and as a test of our method, we have computed a number of non-rotating 1-D models in the considered parameter range. The convergence time of self-consistent models is larger by a factor 5...10, compared to

[8] For computing the force-multiplier parameters, our standard grid is $r_{\rm SG}/R_*(\Theta) = \{1.022,\ 1.034,\ 1.046,\ 1.125,\ 1.25,\ 1.5,\ 2.0,\ 3.0,\ 4.0,\ 6.0\}$. Additional grid points at larger radii lead, if at all, to only small corrections for v_∞, but do not change the surface-integrated mass-loss rate $\dot{M}$.

models with constant $k_{\rm CAK}$, α, δ, owing to their additional "time-dependence". A comparison with the results by Kudritzki et al. (1998, based on the alternative stationary approach) showed an almost perfect agreement.

For *very* thin winds ($\dot{M} \lesssim 10^{-9}\,M_\odot{\rm yr}^{-1}$), however, our method as proposed in this paper does not work: Due to the maximum value of line strength $k_{\rm L} \approx 10^7 \ldots 10^8$ present in any wind plasma, the force-multipliers M *saturate* for $\log t_{\rm S} \lesssim -8$,

$$M(t_{\rm S}) = \frac{v_{\rm therm}}{c}\frac{1}{t_{\rm S}}\sum_{\rm lines\,L}\frac{\nu_L F_{\nu_L}}{F}\left(1-e^{-k_{\rm L}t_{\rm S}}\right) \longrightarrow \frac{v_{\rm therm}}{c}\sum_{\rm lines\,L}\frac{\nu_L F_{\nu_L}}{F}k_{\rm L}\,. \quad (48)$$

In consequence, the slope of $\log M$ (i.e., α) approaches zero for $\log t_{\rm S} \lesssim -7 \ldots -8$, and shows a significant *curvature* in this transition region, in contrast to our assumption of being a *linear* function of $\log t_{\rm S}$. Thus, the values for α arising from our procedure become inaccurate in this regime, and are mostly drastically overestimated for the lowest values of $\log t_{\rm S}$. A solution of this problem is to restrict the fit range to some minimum value of $\log t_{\rm S}$ and to continue with an analytical solution for $M(t_{\rm S})$ in the outer wind, where $\log t_{\rm S} \lesssim -7 \ldots -8$.

In view of the additional uncertainties present for thin winds (e.g., the supposed decoupling of the accelerated metal ions from the rest material of the wind, see Springmann & Pauldrach 1992, Porter 1999) and the notion that winds with such small mass-loss rates are too thin to have any observable effect on optical/IR emission lines and IR/radio continua, we did not follow this possibility, however restricted our further studies to winds with minimum mass-loss rates $\dot{M} \gtrsim 10^{-8}\,M_\odot{\rm yr}^{-1}$.

7.2. 2-D models

As outlined in Sect. 3.3, we have concentrated our investigations on the consequences of rotation for the winds of B-(super)giants. A thorough understanding of these physical effects will allow a future application to the analysis of H$_\alpha$ and IR emission lines as well as the investigation of additional problems discussed there.

In a first step, we will analyze some basic effects by means of a self-consistent reference model. One of the most important issues concerns the question whether our description accounting for 2-D processes still predicts a concentration of wind material above the poles (as is true when using global line-force parameters). With regard to a subsequent application to line diagnostics, we will also quantify the density contrast between equatorial and polar wind.

In a second step, then, we will present the results for a model grid comprising very rapidly rotating B-stars (mostly $v_{\rm rot}/v_{\rm crit} \approx 0.85$). The model parameters have been chosen in such a way that a broad range of luminosities ($\log L/L_\odot = 4.2 \ldots 5.7$) is covered and the (anticipated) mass-loss rates are well above the minimum value discussed in the last section. This investigation will facilitate an estimate of *maximum effects* of stellar rotation on the resulting wind structure and the corresponding deviations from the mean 1-D wind-momentum luminosity relation, both in a global sense and for the polar and equatorial wind. Table 1 introduces this model grid, and Tab. 2 tabulates the according parameters related to rotation. Note, that different rotation rates have been adopted for model B30-30, which will serve as our reference model described in the following.

Model	$T_{\rm eff,1-D}$	Γ	$\log g_{\perp,\rm pole}$	$\log(L/L_\odot)$	$R_{\rm p}/R_\odot$	$M_*/M_\odot$
B10-7.5	20000	0.046	3.31	4.16	10.0	7.5
B15-10	20000	0.078	3.09	4.51	15.0	10.0
B15-15	20000	0.051	3.26	4.51	15.0	15.0
B20-20	20000	0.069	2.14	4.76	20.0	20.0
B30-30	**20000**	**0.104**	**2.96**	**5.11**	**30.0**	**30.0**
B45-30	20000	0.233	2.61	5.47	45.0	30.0
B60-30	20000	0.414	2.36	5.72	60.0	30.0

Model	$v_{\rm sound}$	$H_*/R_{\rm p}$	$v_{\rm esc,spher}$	$v_{\rm crit,spher}$	$v_{\rm crit,2-D}$
B10-7.5	16.1	1.90	522	369	302
B15-10	16.1	2.21	484	342	280
B15-15	16.1	1.43	601	425	347
B20-20	16.1	1.46	596	421	344
B30-30	**16.1**	**1.52**	**585**	**413**	**338**
B45-30	16.1	2.66	442	312	255
B60-30	16.1	4.64	334	236	193

Table 1. Model grid: Stellar and wind parameters. $T_{\rm eff,1-D}$: effective temperature for $v_{\rm rot}$ = 0; Γ: Eddington-Γ; $\log g_{\perp,\rm pole}$: normal gravity at the pole; $v_{\rm esc,spher} = \sqrt{2GM_*(1-\Gamma)/R_*}$: escape velocity for spherical stellar surface; $v_{\rm crit,spher} = v_{\rm esc,spher}/\sqrt{2}$: critical velocity for spherical stellar surface; $v_{\rm crit,2-D}$: critical velocity for a-spherical stellar surface (given by PP96, Eq. 20). Velocities in km s^{-1}, and solar helium abundance $Y_{\rm He} = 0.1$ assumed for all models. Bold: Reference model B30-30.

Model	$v_{\rm rot}$	$\frac{v_{\rm rot}}{v_{\rm crit,2-D}}$	$\log g_{\perp,\rm eq}$	$v_{\rm esc,eq}$	$R_{\rm eq}$	$T_{\rm eff,eq}$	$T_{\rm eff,p}$
B10-7.5	250	0.83	2.70	292	1.30	15258	21773
B15-10	230	0.82	2.48	275	1.29	15381	21745
B15-15	300	0.87	2.54	303	1.33	14483	21928
B20-20	300	0.87	2.39	292	1.34	14282	21963
B30-30	100	0.30	2.91	559	1.03	19595	20120
B30-30	200	0.59	2.72	471	1.13	18146	20856
B30-30	**290**	**0.86**	**2.26**	**299**	**1.33**	**14605**	**21906**
B45-30	220	0.85	1.89	223	1.33	14513	21923
B60-30	160	0.83	1.74	187	1.30	15155	21774

Table 2. Model grid: Parameters related to rotation. Equatorial radius $R_{\rm eq}$ in units of $R_{\rm p}$, polar/equatorial effective temperature $T_{\rm eff,p}$, $T_{\rm eff,eq}$ in K, $v_{\rm rot}$ in km s^{-1}. $g_{\perp,\rm eq}$ and $v_{\rm esc,eq}$ denote the equatorial normal gravity and escape velocity, respectively (for 1-D Thomson acceleration). The corresponding polar values $\log g_{\perp,\rm pole}$ and $v_{\rm esc,spher}$ are listed in Tab. 1. Bold: Reference Model B30-30 with $v_{\rm rot} = 290$km s^{-1}.

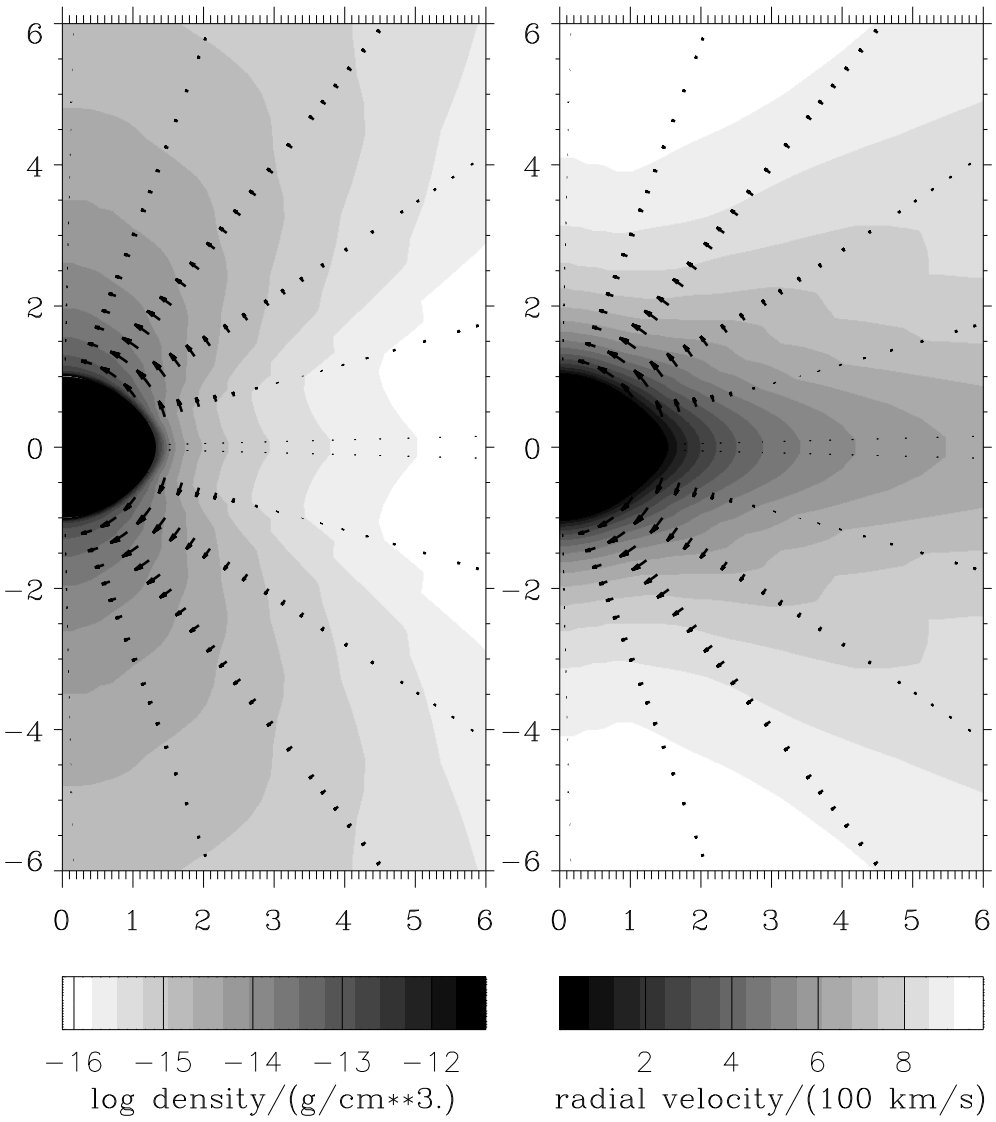

Fig. 12. Density and radial velocity component for the wind model B30-30 (KU) and $v_{\rm rot}$ = $0.86\,v_{\rm crit,2-D}$ = 290 km s^{-1}, with *consistent* force-multiplier parameters. The arrows indicate the polar velocities, with a maximum (absolute) value $|v_\Theta|_{\rm max} \approx 50$ km s^{-1}.

Model	$v_{\rm rot}$	$v_{\rm rot}/v_{\rm crit}$	$\dot{M}_{\rm p}(1)$	$\dot{M}_{\rm p}(6)$	$\dot{M}_{\rm eq}(6)$	$\dot{M}_{\rm total}$	$\dot{M}_{1-\rm D}$	$v_{\infty,1-\rm D}$	$v_\infty(0°)$	$v_\infty(90°)$	$\max(\lvert v_\Theta\rvert)$
B10-7.5	250	0.83	1.53(−1)	1.99(−1)	8.10(−3)	5.42(−2)	6.03(−2)	989	833	793	34
B15-10	230	0.82	5.72(−1)	7.67(−1)	3.85(−2)	2.15(−1)	2.20(−1)	940	820	604	37
B15-15	300	0.87	5.40(−1)	5.32(−1)	2.00(−2)	1.40(−1)	1.48(−1)	1171	1020	798	51
B20-20	300	0.87	7.45(−1)	1.24	4.89(−2)	3.24(−1)	3.30(−1)	1197	1048	710	50
B30-30	100	0.30	1.52	1.33	9.75(−1)	1.11	1.15	1186	1087	1161	22
B30-30	200	0.59	1.61	2.42	5.88(−1)	1.07	1.15	1186	1081	1012	31
B30-30 (KU)	**290**	**0.86**	**2.43**	**4.41**	**1.92(−1)**	**1.12**	**1.15**	**1186**	**1031**	**727**	**50**
B30-30 (GL)	290	0.86	2.56	3.76	5.50(−1)	1.47	1.15	1186	930	753	45
B30-30 (P)	290	0.86	1.06(−1)	1.24(−1)	5.24(−3)	3.85(−2)	4.41(−2)	2267	1253	1787	48
B45-30	220	0.85	18.5	28.7	1.78	7.80	6.23	917	746	447	47
B60-30	160	0.83	78.1	111.6	9.89	34.2	16.8	925	559	411	37

Table 3. Numerical results for 2-D wind models. $\dot{M}_{\rm total}$: total (i.e., surface-integrated) mass-loss rate in $10^{-6}\ M_\odot {\rm yr}^{-1}$; $\dot{M}_{\rm p}(1)$: polar mass-loss rate at the wind base; $\dot{M}_{\rm p\,/\,eq}(6)$: polar/equatorial mass-loss rate for $r = 6\,R_{\rm p}$; rotational velocities $v_{\rm rot}$ in km s^{-1}; $v_\infty(\Theta)$ taken at $r_{\rm max}$. P/KU: irradiation with Planck/Kurucz fluxes, GL: Model with global f.-m. parameters. Bold: Reference Model B30-30(KU) with $v_{\rm rot} = 290$km s^{-1}.

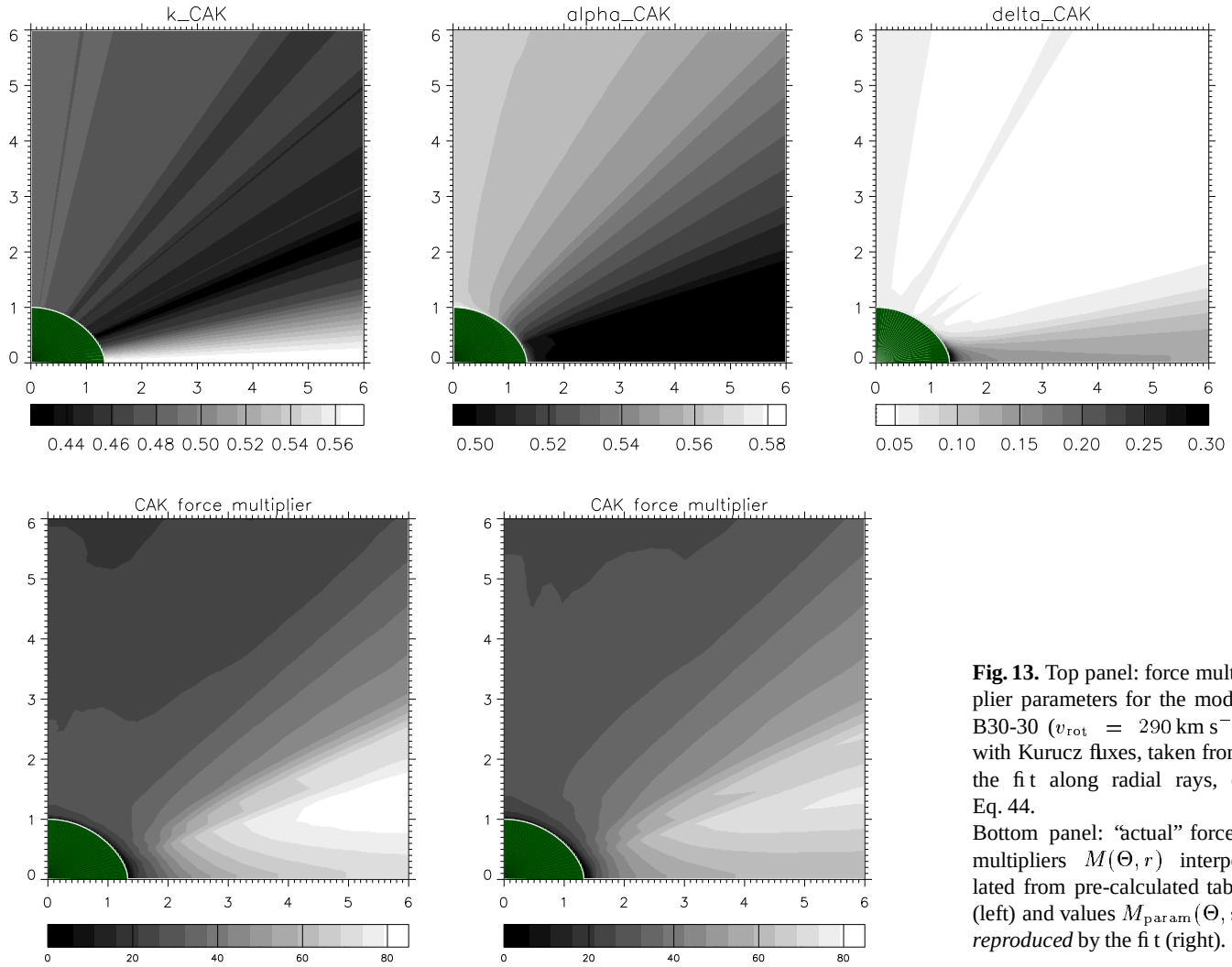

Fig. 13. Top panel: force multiplier parameters for the model B30-30 ($v_{\rm rot} = 290\,{\rm km\,s^{-1}}$) with Kurucz fluxes, taken from the fit along radial rays, cf. Eq. 44.
Bottom panel: "actual" force-multipliers $M(\Theta, r)$ interpolated from pre-calculated table (left) and values $M_{\rm param}(\Theta, r)$ *reproduced* by the fit (right).

Model	$\tau_{\rm L}(0°)$	$\tau_{\rm L}(22°)$	$\tau_{\rm L}(45°)$	$\tau_{\rm L}(67°)$	$\tau_{\rm L}(90°)$
B10-7.5	0.04	0.03	0.02	0.01	0.005
B15-10	0.20	0.17	0.13	0.06	0.03
B15-15	0.07	0.043	0.035	0.009	0.009
B20-20	0.10	0.10	0.08	0.017	0.019
B30-30 (100)	0.15	0.13	0.085	0.085	0.09
B30-30 (200)	0.21	0.17	0.16	0.11	0.09
B30-30 (290)	**0.42**	**0.37**	**0.28**	**0.07**	**0.04**
B30-30 (P)	$3.3\ 10^{-4}$	$2.7\ 10^{-4}$	$1.3\ 10^{-4}$	$2.8\ 10^{-5}$	$7.2\ 10^{-6}$
B45-30	9.8	8.3	13.5	11.5	25.4
B60-30	119	89	96	93	61

Table 4. Optical depth in the Lyman continuum $\tau_{\rm L}$, according to Lamers & Pauldrach (1991, Eq. 7) for the different B-star wind models at different co-latitudes Θ.
The assumption of an optically thin continuum is invalid for the models B45-30 and B60-30, since $\tau_{\rm L}$ is larger than unity for all co-latitudes. P: Planck irradiation. Bold: Reference Model B30-30 with $v_{\rm rot} = 290{\rm km\,s^{-1}}$.

7.2.1. 2-D reference model for a B-supergiant wind

In this section, we investigate basic effects of rotation on the wind structure for a distinct B-star wind model in the framework of our self-consistent theory. From our grid, we have chosen the model "B30-30" with $T_{\rm eff}$ = 20000 K, $\log L/L_\odot = 5.11$, $M_*/M_\odot = 30$ and a polar radius $R_{\rm p}/R_\odot$ = 30 (all other parameters can be found in Tables 1 and 2) as a typical representative with moderate mass-loss.

Since we concentrate on winds with an *optically thin continuum* in the present investigation, we have to check whether the (final) mass-loss rate lies well below the critical value for which the wind becomes optically thick in the Lyman continuum. Otherwise, an abruptly enhanced mass-loss at co-latitudes Θ with $\tau_{\rm L}(\Theta) \gtrsim 1$ at the wind base (owing to the bi-stability effect, see Sect. 2.2) is to be expected. For our reference model with $v_{\rm rot}$ = 0.86 $v_{\rm crit,2-D} = 290\,{\rm km\,s^{-1}}$, we have $\tau_{\rm L} < 1$ ($\forall\,\Theta$), and the assumption of an optically thin continuum is justified. (Eq. 7 from Lamers & Pauldrach 1991 yields $\tau_{\rm L}(0°) = 0.42$ at the pole and $\tau_{\rm L}(90°) = 0.04$ at the equator, cf. Tab. 4). Fig. 12 displays the resulting density structure and the radial velocity field for our model with Kurucz fluxes, after a flow time of $2 \cdot 10^6$ s. Characteristic numerical results of this and further simulations are summarized in Tab. 3.

The wind structure is clearly *prolate*, and the polar density contrast significantly increases towards larger radii, with maxi-

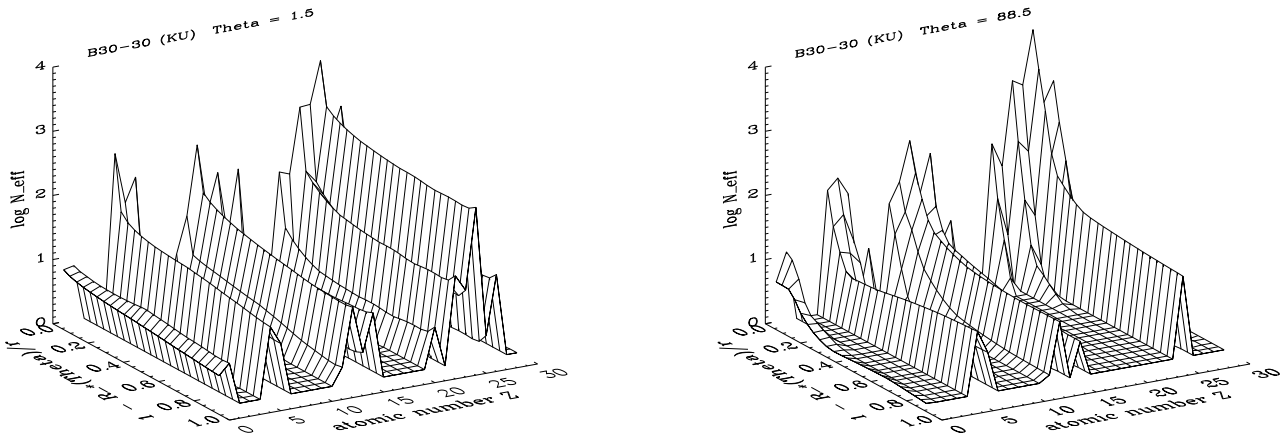

Fig. 14. Model B30-30 (KU): Contribution of various elements to the line acceleration over the pole (left) and in the equatorial plane (right), as function of $1 - R_*(\Theta)/r$.

mum values $\rho_{\rm p}/\rho_{\rm eq} \approx 15$. (Note that from here on we use *polar* density contrasts, i.e., the inverse of the equatorial density contrast introduced in Sect. 3.3.) The wind is fast over the poles, with $v_\infty(0°) \approx 1030\,\mathrm{km\,s^{-1}}$, and slowest in the equatorial plane, with $v_\infty(90°) \approx 730\,\mathrm{km\,s^{-1}}$. The matter is deflected towards the polar regions, and the *negative* polar velocity reaches a maximum (absolute) value of $|v_\Theta|_{\max} \approx 50\,\mathrm{km\,s^{-1}}$. Responsible for this deflection is, as mentioned in Sect. 3.3, the negative polar component $g_\Theta^{\rm lines}$ arising from local asymmetric line resonances: For this model, $\partial v_r/\partial\Theta$ is negative in the major part, and consequently also $g_\Theta^{\rm lines}$.

To illustrate both the order of magnitude of the force-multiplier parameters and the quality of our fit procedure, Fig. 13 (top panel) displays these quantities as function of Θ and r. The lower panel shows the total force-multipliers $M(\Theta, r)$, either taken from our pre-calculated table as function of local variables $\log t_r$, $\log \hat{n}$, W and $\overline{T}_{\rm eff,cont}$ (i.e., the "actual" force-multiplier; left) and the corresponding values resulting from the fit along radial rays, $M_{\rm param} = k_{\rm CAK}\, t_r^{-\alpha}\, \hat{n}^{\delta}$ (right). Interestingly, the force-multiplier M is a *non-monotonic* function of co-latitude (for fixed r). We will explain this behaviour in section 7.2.4.

The resulting parameters $k_{\rm CAK}$, α, δ correspond, to order of magnitude, to the values one would expect from detailed 1-D non-LTE calculations for the considered temperature range (e.g., α decreases for lower temperatures, as discussed in Puls et al. 2000). Considering the complexity of the covered parameter space, our fit procedure yields a very good reproduction of the actual values M by $M_{\rm param}$, with maximum errors of 5…10%.

Physical properties. Fig. 14 displays the contribution from various elements to the line force as function of radius over the pole and in the equatorial plane, respectively, for our self-consistent 2-D model. As in Sect. 5, we have plotted $N_{\rm eff}$ (roughly the number of optically thick driving lines, see Eq. 31) over atomic number Z and radius.

At first, let us discuss some general features. Over the pole, the contribution from the iron group (in particular, iron itself) clearly dominates for all radii. In the outer wind and with increasing co-latitude Θ, however, the *relative* acceleration from iron (although always dominating) significantly decreases, compared to the one from other species. This global behaviour results mainly from the decreasing (effective) wind density $n_{\rm e}/W$ for larger r and Θ (cf. Fig. 12, left). The contribution from iron is mainly due to several hundred thousand unsaturated meta-stable lines, whereas a few saturated resonance lines are decisive for the CNO group (in particular, in the outer wind), as discussed in section 5. Consequently, iron is more important in the dense wind over the poles than in the equatorial plane, where the wind is thinner and the unsaturated meta-stable lines are less effective than the strong resonance lines (see also Puls et al. 2000).

For all elements, $N_{\rm eff}$ is maximum close to the star, where the density is highest, and decreases with radius (with the exception of carbon in the equatorial plane, see below), however to a much larger extent at the equator than over the pole. This effect is readily understood if one accounts for the increasing radiation temperature as function of radius in equatorial regions (cf. Fig. 9): the larger the distance to the star, the more also hot surface elements near the pole contribute to the mean radiation field there. In combination with the decreasing density, this effect supports *higher ionization stages* with a smaller line number: Thus, $N_{\rm eff}$ decreases drastically with radius. In polar regions, vice versa, the decreasing density is partly compensated by a decreasing radiation temperature, and the ionization remains much more constant, with the result that also $N_{\rm eff}$ remains much more constant as function of radius.

For the remaining discussion, we will restrict ourselves to iron and carbon which are the two elements contributing most to the line force.

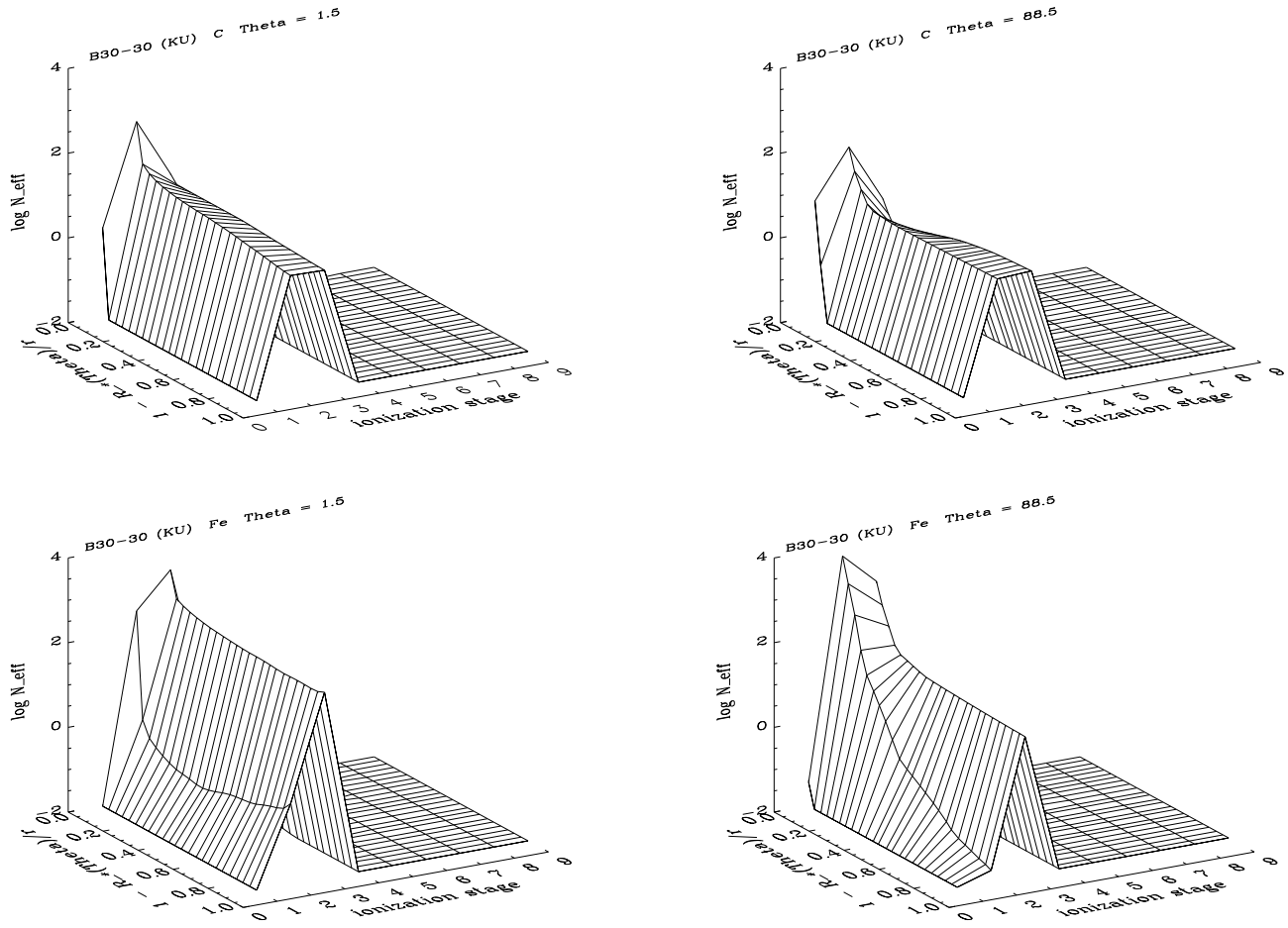

Fig. 15. As Fig. 14, however contribution of various ionization stages of carbon (top) and iron (bottom).

Concerning these elements, two aspects are striking in the equatorial plane (see Fig. 14, right panel): Firstly, close to the star, the contribution from iron is significantly larger than over the pole (note the logarithmic scale!), and secondly, $N_{\rm eff}$ increases for carbon for larger r, as mentioned already above.

To understand the first point, we have plotted the corresponding *polar ionization structure* at the wind base in Fig. 16 (top panel). Shown are the ionization fractions

$$f_{jk} = n_{jk}/n_k\,, \qquad k = 6, 26,\ j = 1 \ldots 6, \tag{49}$$

with n_k the number density of element k and n_{jk} the one of ionization stage j.

The polar variation of these fractions is essentially controlled by the variation of the mean radiation field, which decreases from pole to equator (with $\overline{T}_{\rm eff,cont}\,(\Theta) \approx T_{\rm eff}(\Theta)$ for $r \approx R_*(\Theta)$). Throughout the entire wind, FeIII is the major ionization stage. For $\Theta \to 90^\circ$ and close to the star, however, the fraction of FeII significantly increases, providing much more driving lines than FeIII[9]. In consequence, FeIII dominates over the hot pole (all radii), whereas FeII is decisive for the line force at the equator (lower wind, compare the left and right bottom panels of Fig. 15).

For minor ionization stages, f_{jk} strongly varies with colatitude only close to the star, as is obvious from the sequence in Fig. 16: The larger r, the more $f_{jk}(\Theta)$ becomes constant, since $\overline{T}_{\rm eff,cont}$ varies only mildly with Θ in the outer wind (cf. Fig. 9).

To illuminate the behaviour of carbon in the equatorial plane ($N_{\rm eff}$ increases with r in the outer wind), let us concentrate on Fig. 15, upper panel. Over the pole (left), the contribution from CII exceeds the one from CIII, since the spectrum of CII has numerous unsaturated lines which are most effective in the dense part of the wind. Because of the counteracting rôle of decreasing density and decreasing radiation temperature, the ionization structure remains roughly constant, and $N_{\rm eff}$ is only mildly varying. In the equatorial plane, however, the ionization fraction of CIII is continuously increasing (decreasing density and increasing temperature working in the same direction), and the strong resonance lines of CIII become crucial for the line driving in the thinner wind (cf. AB82, Tab. 5). Thus, $N_{\rm eff}$ increases with r for carbon.

[9] The contribution of FeII of course, decreases again for larger radii, as discussed above

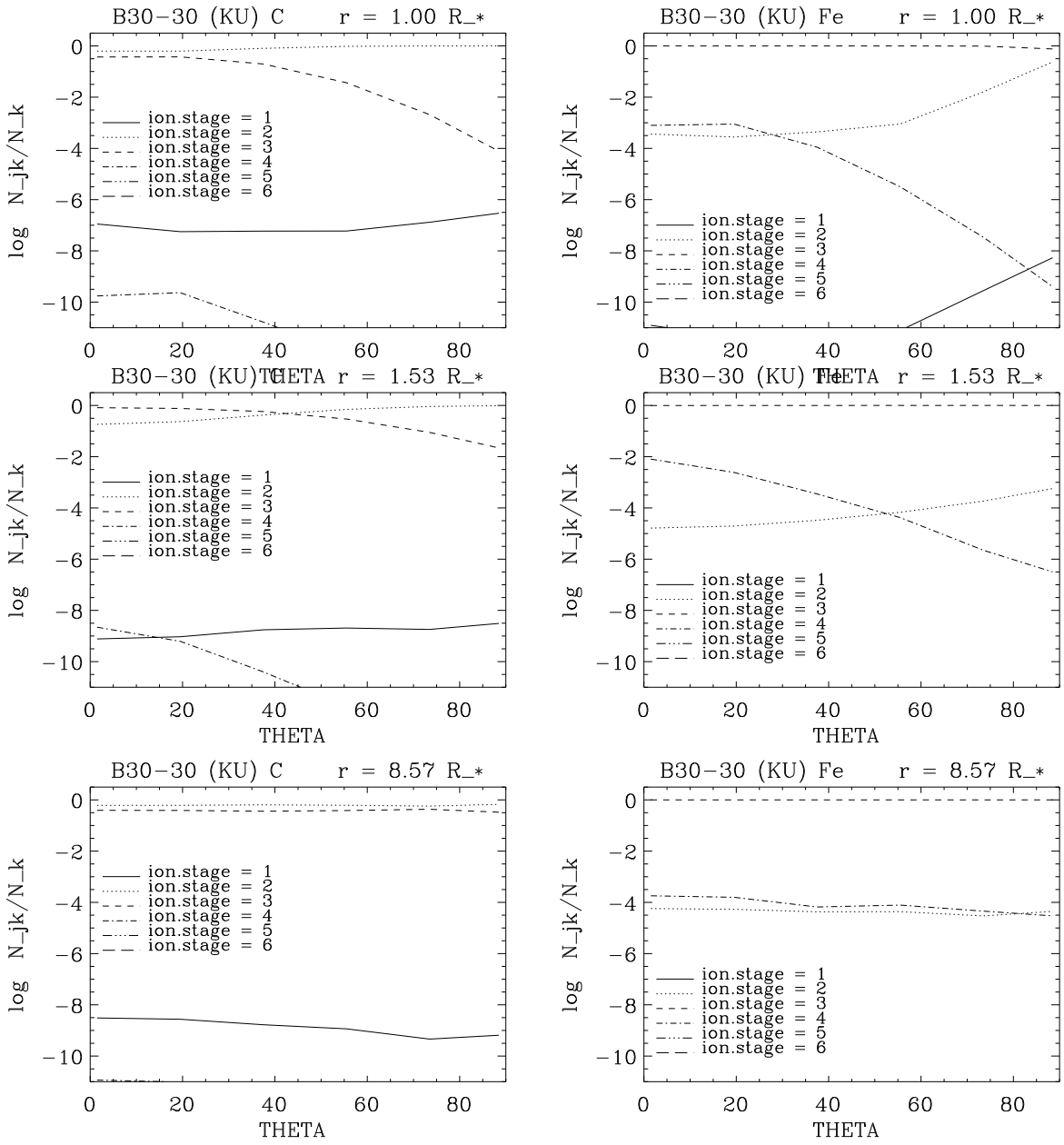

Fig. 16. Model B30-30(KU): Ionization fractions of carbon (left) and iron (right) at distinct radial points $r/R_*(\Theta)$, as function of co-latitude.

To underline and summarize our findings, Fig. 17 shows the *radial ionization structure* of carbon and iron , over the pole and in the equatorial plane. Very close to the star, the *effective* wind density is largest and favours low ionization stages. In polar regions, however, the local effective temperature $\overline{T}_{\rm eff,cont}$ is at maximum and supports higher ionization stages.

Over the pole and for larger r, both $n_{\rm e}/W$ and $\overline{T}_{\rm eff,cont}$ decrease (with $n_{\rm e}/W$ less variable than at the wind base), and the balance of their opposite effect determines the ionization equilibrium, keeping it roughly constant in the "high" state. Trace ions show rather constant ionization fractions, too.

In the equatorial plane, the density decreases for larger r, while $\overline{T}_{\rm eff,cont}$ grows. Both effects support higher ionization stages, and the degree of ionization is monotonically increasing with r.

Since close to the star the ionization is lower for equatorial regions, also the number of driving lines ($N_{\rm eff}$) is larger than over the poles, due to the larger number of lines being present. Nevertheless, as we have seen, the wind is slow and thin in the equatorial plane and fast and dense over the poles.

This morphology is a consequence of the dependence of the total illuminating flux on $\overline{T}^4_{\rm eff,cont}$ (which over-compensates the larger number of driving lines, $g_{\rm rad} \propto N_{\rm eff} \times {\rm flux}$!) and the lack of an *abrupt* transition to lower ionization stages, when going from pole to equator. Such an effect (as supposed to be present in the bi-stability scenario) might induce a significantly

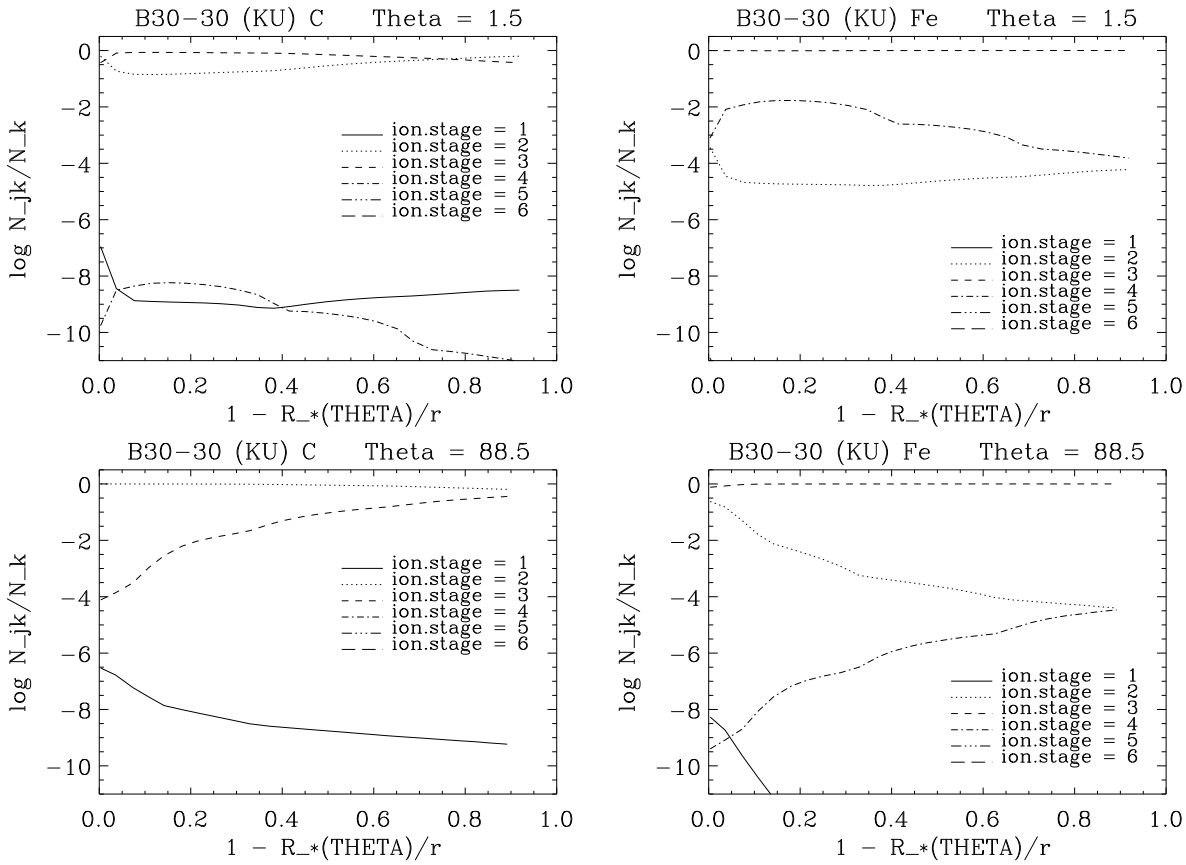

Fig. 17. Model B30-30(KU): Ionization fractions of carbon (right) and iron (left) over the pole (top) and in the equatorial plane (bottom), as function of radius.

enhanced equatorial mass-loss, if the lower ionization stages begin to dominate from a certain co-latitude on, with $N_{\rm eff}$ increasing much more than in the models we have considered here.

Specific effects due to 2-D NLTE description: Comparison with models based on global force-multiplier parameters. So far, we have discussed some major results of our self-consistent 2-D NLTE description. In the following, we will investigate the extent to which these models differ from those utilizing *global* force-multiplier parameters (including, of course, the same assumptions, i.e., allowing for gravity darkening and non-radial radiative forces). This comparison will allow to estimate the importance of a self-consistent approach.

Such global parameters represent estimated *averages* of the corresponding parameters for our self-consistent model, and have been derived from the results of our previous section. For the model described above, Fig. 13 (top panel) shows that $k_{\rm CAK} = 0.50$, $\alpha = 0.54$ and $\delta = 0.10$ can be considered as appropriate average values .

Using these global parameters at first in a *1-D* simulation at $T_{\rm eff} = 20000$ K, the differences between the self-consistent and the global approach turned out to be of only minor nature, related to the same *unique* radiation temperature in both models which causes an almost identical ionization structure and effective line-number $N_{\rm eff}(Z, r)$. The only differences we have found concern the density stratification and are marginal.

On the other side, the differences for a *2-D* model are much more severe, thus immediately pointing to the dominant rôle of the radiation temperature (varying as function of (r, Θ)). The results for the corresponding 2-D simulation with global force-multiplier parameters (as given above) are listed in Tab. 3 and 5, and Figs. 22, 23, 24 compare, among others, the density and velocity stratification of our self-consistent and the "global" model. The total mass-loss rate $\dot{M} = 1.47 \cdot 10^{-6}\, M_\odot {\rm yr}^{-1}$ of the latter agrees at least qualitatively with the value found for the self-consistent model ($\dot{M} = 1.12 \cdot 10^{-6}\, M_\odot {\rm yr}^{-1}$).[10] Compared to the model with global mean [11] force-multiplier parameters, however, our self-consistent model reveals a moderately

[10] Since we are mainly interested in differential effects which are independent of the absolute mass-loss rate, e.g., the polar/equatorial density contrast, we have not performed any further rescaling.

[11] Strictly speaking, the designation "mean parameters" is not entirely correct for the values used in our second simulation, since δ has values up to $\delta \lesssim 0.3$ in the equatorial regions and ranges in between $0.05 \ldots 0.07$ elsewhere. An over- or underestimate of this parameter, respectively, affects mainly the radial expansion (the smaller $(\alpha - \delta)$, the slower the wind-expansion), and leads to a stronger or weaker density contrast $\rho_{\rm eq}/\rho_{\rm p}$. An erroneous estimate of the average

enhanced concentration of wind material over the poles and a significant evaporation of the wind in the equatorial plane; the corresponding density contrast $\rho_{\rm p}/\rho_{\rm eq}$ is amplified by roughly a factor of three.

This difference in density structure is related to the fact that any model using global line-force parameters *cannot* react on ionization gradients, which are mostly a function of co-latitude, as discussed above.

For the converged global model, we have also calculated the radial ionization structure and the effective number of optically thick driving lines $N_{\rm eff}$ as posteriori, which are then, of course, in no way self-consistent. A comparison with the corresponding values from our self-consistent approach reveals that the differences over the pole are almost negligible. In the equatorial plane, however, the self-consistent model shows stronger radial ionization gradients than present in the global model, and $N_{\rm eff}$ is much smaller, especially for iron. Again, these differences arise from the additive effect of increasing radiation temperature and decreasing density, where the latter is significantly lower in the self-consistent model (cf. Tab. 3).

Thus, we see that our self-consistent treatment is especially important in *equatorial regions*, since any disturbance of the hydrodynamical stratification is effectively amplified via the back-reaction of the induced disturbance of the ionization structure, whereas the counteracting effects of density and radiation field near the pole lead to a much smoother behaviour.

In conclusion, it is the specific radial dependence of density and mean radiation field (acting in opposite or parallel) which leads to a density contrast between polar and equatorial wind which is even stronger than for any global model: For larger distances from the star, higher ionization stages with fewer driving lines are favoured near equatorial regions, whereas over the poles the line acceleration remains efficient over a larger radius interval, as a consequence of a much more constant ionization structure.

Note, that these results should apply under fairly general conditions, with the only exception of iron, if a transition from FeIII to FeIV (which has an extremely rich spectrum, cf. Springmann & Puls 1998) would occur in the lower wind region where the mass-loss rate is adjusted. In the temperature region discussed here, however FeIV is completely unimportant.

Thus, our new and quantitative approach of the wind dynamics does not weaken the prolate wind structure arising from non-radial line forces and gravity darkening or even induce the formation of an oblate structure, but rather suggests the contrary effect, i.e., increases the degree of "prolateness"! Of course, this conclusion concerns only those cases with an optically thin Lyman continuum everywhere.

values causing a change in $\rho_{\rm eq}/\rho_{\rm p}$ by a factor of two, however, seems rather unlikely.

GLOBAL			
r	$\rho_{\rm p}/\rho_{\rm eq}$	$\dot{M}_{\rm p}$	$\dot{M}_{\rm eq}$
1	2.25	2.56	2.00(−1)
2	8.37	3.28	4.88(−1)
4	8.73	3.66	5.37(−1)
6	9.59	3.76	5.54(−1)
8	10.1	3.83	5.63(−1)
	$\min(v_\Theta)$	$v_{\infty,\rm p}$	$v_{\infty,\rm eq}$
	−45	930	753

noNRF			
r	$\rho_{\rm p}/\rho_{\rm eq}$	$\dot{M}_{\rm p}$	$\dot{M}_{\rm eq}$
1	7.64	3.64	−7.3(−2)
2	0.69	2.87	1.31
4	0.81	2.76	1.21
6	0.92	2.73	1.24
8	1.37	2.72	1.02
	$\max(v_\Theta)$	$v_{\infty,\rm p}$	$v_{\infty,\rm eq}$
	45	1316	371

Table 5. Characteristic results for stellar winds utilizing different approximations, for stellar model B30-30. GLOBAL: 2-D model with global force-multiplier parameters. No NRF: self-consistent force-multiplier, however purely radial radiation force. r in $R_\star(\Theta)$, mass-loss rates over the pole and in the equatorial plane $\dot{M}_{\rm p\,/\,eq} = 4\pi r^2 v_r(\Theta,r)\rho_{\rm p\,/\,eq}(\Theta,r)$ in $10^{-6}\,M_\odot{\rm yr}^{-1}$, velocities in km s^{-1}.

7.2.2. Gravity darkening alone

As we have mentioned a number of times, two effects control the wind morphology and the actual degree of asphericity: The polar component of the line acceleration, $g_\Theta^{\rm lines}$, causes a polewards redistribution of wind matter. Gravity darkening increases the polar flux and amplifies the polar density contrast. Additionally, it controls the ionization structure in such a way that this contrast becomes even stronger than in models with constant radiation temperature (as function of (r,Θ)).

It is interesting to isolate the pure effect of gravity darkening from the impact of the non-radial line-forces and to investigate the resulting wind- and especially ionization structure. The according model (with $g_\Theta^{\rm lines} = g_\Phi^{\rm lines} = g_\Theta^{\rm cont} \equiv 0$, stellar parameters as for B30-30(KU), *consistent force-multipliers*) is shown in Fig. 18, and characteristical results are summarized in Tab. 5.

The *density* structure of this model again is *globally prolate*, however with an *equatorwards directed* polar velocity of maximum value $v_{\Theta,\rm max} \approx 45\,{\rm km\,s^{-1}}$ (supersonic) near the equatorial plane. Thus, a wind compressed disk is formed.

The radial outflow of the disk matter is markedly slower $v_\infty(90°) \approx 470\,{\rm km\,s^{-1}}$ than the outflow of polar material ($v_\infty(0°) \approx 1350\,{\rm km\,s^{-1}}$).[12] The polar density contrast never exceeds a factor of roughly three, to be compared with the much higher values suggested for the original WCD model for the winds of main sequence stars, cf. Sect. 3.3. This rather small value is the consequence of the increased polar mass-loss due to gravity darkening, the reduced values of v_Θ arising in parallel and the lower values of δ valid for our supergiant model, resulting in a faster acceleration of the lower wind material.

[12] The numerical simulation of this model caused some problems, arising from the high density of the disk very close to the star. The line acceleration $g^{\rm lines} \sim 1/\rho$ becomes very small, and inner disk material is accreted onto the stellar surface, with an accretion speed of order $v_r \approx -v_{\rm sound}$ directly above this surface.

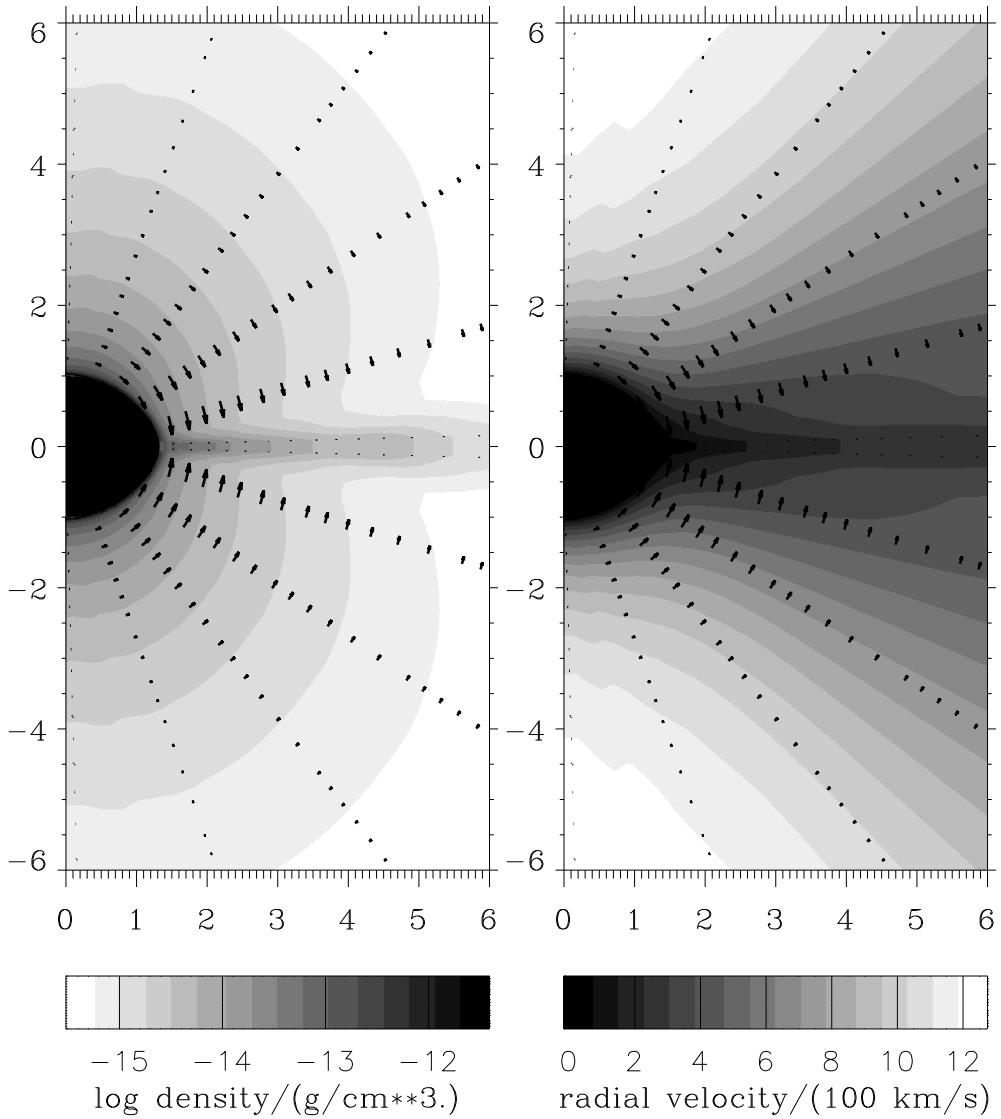

Fig. 18. Density and radial velocity field for the wind of model B30-30, with a *purely radial* radiative acceleration. The arrows indicate the polar velocity component (directed equatorwards) with a maximum value $v_{\Theta,\max} \approx 45\,\mathrm{km\,s^{-1}}$.

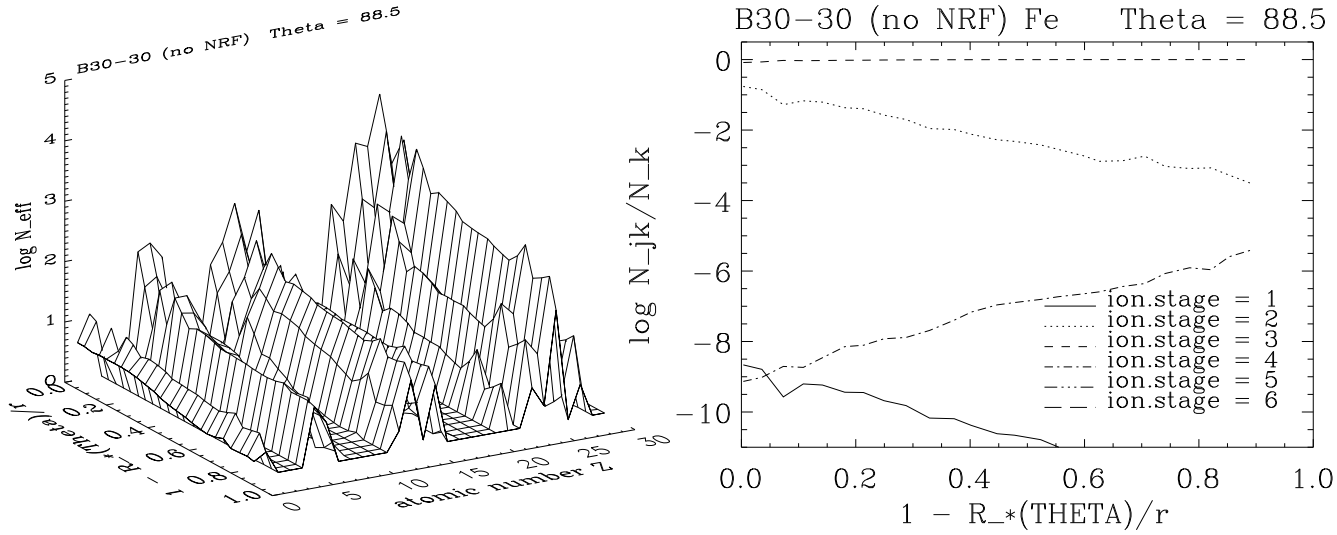

Fig. 19. Model B30-30, with purely radial radiative acceleration. $N_{\mathrm{eff}}(Z, r)$ (left) and ionization fractions of iron (right) in the equatorial plane.

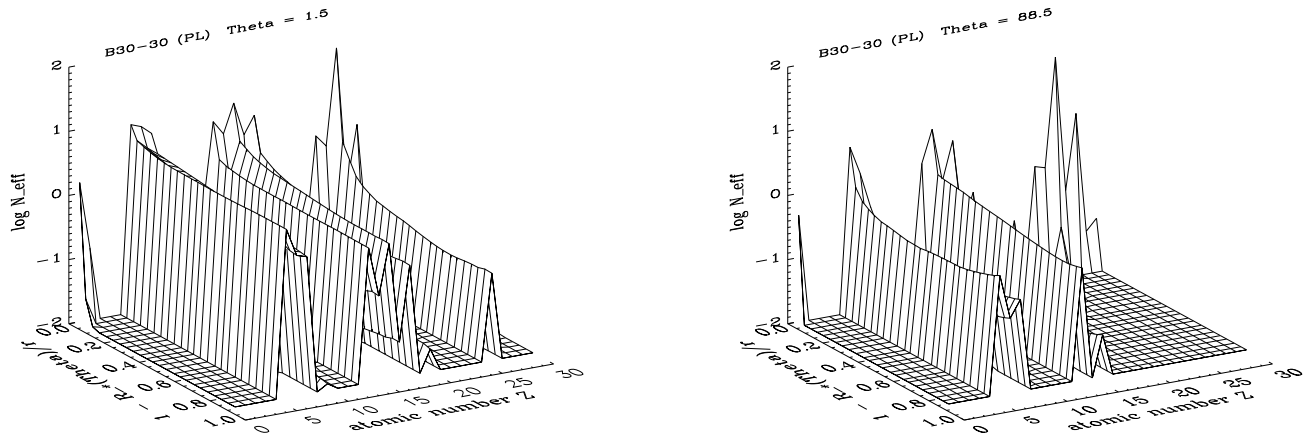

Fig. 20. As Fig. 14, however for model B30-30 illuminated by Planck fluxes. Note the different scaling for $\log N_{\rm eff}$.

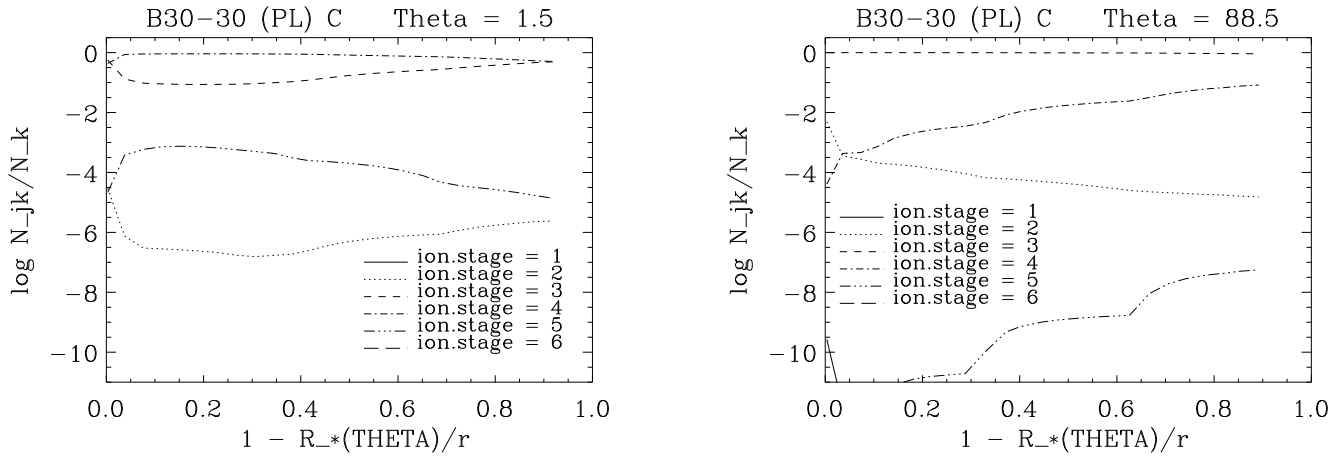

Fig. 21. Model B30-30 for Planck irradiation. Ionization fractions f_{jk} for carbon at the pole and the equator.

Additionally, this density contrast behaves non-monotonically as function of radius, since the disk evaporates relatively faster than the polar wind for larger radii.

The ionization structure close to the stellar surface (Fig. 19, right) and the contribution from the various ionization stages in the equatorial plane (Fig. 19, left) show an interesting behaviour: Compared to the original model B30-30 including non-radial line/continuum accelerations, we find a significantly enhanced contribution from the iron group in the equatorial disk. (The small disturbances in $N_{\rm eff}(Z,r)$ are due to the fact that this model has been calculated for only 10^6 s of physical time, and has not entirely converged yet.) In accordance with the higher density in the disk, FeII (FeIV) is slightly more (less) abundant. However, FeIII behaves almost identical and is the major ionization stage in in both models. This result illustrates very clearly that the *ionization equilibrium is mainly determined* by the non-local *radiation field* rather than by the local density (provided that the local densities of the individual models do not differ by several orders of magnitude).

With respect to these findings, the influence of *X-rays* generated in the shock zones confining the equatorial disk (neglected in our approach) might be of importance. In particular for (very) high ionization stages, the ionization equilibrium will be changed considerably (cf. MacFarlane et al. 1993, Pauldrach et al. 1994), and we have to admit that our modeling is not entirely self-consistent yet concerning this point.

In any case, this model impressively demonstrates the importance of non-radial line-forces for the wind morphology. Only if these forces are included, an *unambiguously* prolate wind structure is formed, whereas their neglect gives rise to an equatorial disk even for models with a self-consistent line force parameterization. Induced by the polewards directed line-acceleration $g_\Theta^{\rm lines}$, matter is redistributed towards the polar regions, and the corresponding azimuthal component $g_\Phi^{\rm lines}$ spins down the wind rotation in the vicinity of the equator, thus additionally weakening the compression mechanism.

7.2.3. Irradiation by Planck flux distributions

Employing a realistic illuminating energy distribution is essential for the wind dynamics, as demonstrated in the following by means of a wind model similar to model B30-30, however

irradiated by Planck fluxes. The numerical results of this simulation are listed in Tab. 3.

A comparison of these data (B30-30, PL) with those obtained for an irradiation by Kurucz fluxes (B30-30, KU) yields the following differences: In the Planck case, the mass-loss rate $\dot{M} = 3.85 \cdot 10^{-8}\, M_\odot \mathrm{yr}^{-1}$ is smaller by roughly a factor 30, whereas the velocities are significantly higher, especially at the equator (1790 km s^{-1} vs. 730 km s^{-1} for the KU-model). Note also that for Planck-fluxes the equatorial wind is faster than the polar one, in contrast to our reference model (see below).

The major ionization stages are, for Planck irradiation and on the average, one stage higher than in the Kurucz case, in agreement with our findings from Sect. 5 (esp. Fig. 6). In consequence, the number of accelerating lines is smaller, implying a significantly reduced mass-loss rate. Fig. 20 displays N_{eff} for different elements over the pole and in the equatorial plane. Now, the major contribution is due to the CNO group and silicon, sulfur and argon (Z=14, 16, 18) rather than to iron, in agreement with the findings by Puls et al. (2000) that these light ions are the effective ones in such thin winds. Only close to the stellar surface, iron dominates because of the higher density.

Almost throughout the entire wind, CIII is the dominant ion (again one stage higher than for Kurucz irradiation) and one of the major contributors to the line force. The behaviour of CIV, however, is more interesting. Note at first that at the wind base a strong polar gradient in the ionization fraction of this ion is present (Fig. 21), leading to a significantly smaller contribution from CIV in the equatorial plane than over the poles. Due to the increasing radiation temperature and decreasing density, the contribution of CIV increases with radius in equatorial regions (as was true for CIII in the Kurucz case). For the thin wind studied here, however, carbon is essential for the acceleration, and the increasing contribution by CIV acts as an "after-burner" for the equatorial flow. This explains the higher terminal velocities found above.

7.2.4. Dependence of wind properties on rotation rate.

So far, we have investigated the physical properties for our reference model and an extremely high rotation rate, $v_{\mathrm{rot}} \approx 0.85\, v_{\mathrm{crit}}$, to estimate *maximum* rotational effects on and differences between the polar and the equatorial wind, with special emphasis on the NLTE aspect. In the following, we will study the wind morphology as function of rotation rate, again for model B30-30 (KU). Additionally, we will check basic predictions from simple scaling arguments.

Fig. 22 displays the density contrast $\rho(\Theta)/\rho_{\mathrm{eq}}$ for three different values of v_{rot} at $r = 4\, R_*$, where the flow has become more or less purely radial and, therefore, $\rho_{\mathrm{p}}/\rho_{\mathrm{eq}}$ has already converged to its maximum value. For $v_{\mathrm{rot}} = 100\,\mathrm{km\,s^{-1}}$ ($0.3\, v_{\mathrm{crit}}$), the data indicate only a minor deviation from unity, $\rho_{\mathrm{p}}/\rho_{\mathrm{eq}} \approx 1.5$, and mass-loss rates $\dot{M}(\Theta)$ varying by the same factor, as shown in Fig. 24. For this low rotation rate, the latitudinal dependence of $v_\infty(\Theta)$ is marginal ($\lesssim 100$km s^{-1}; see Fig. 23).

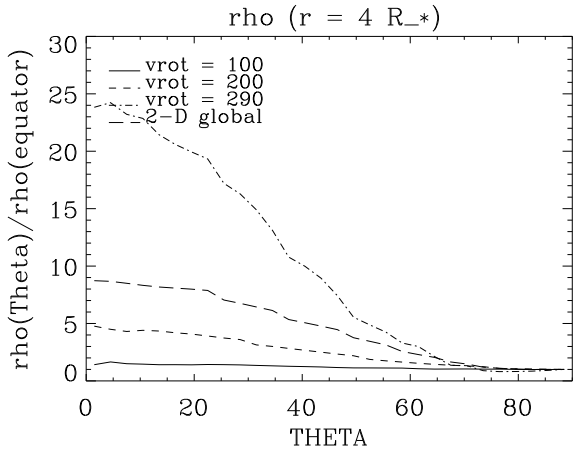

Fig. 22. Ratio of local density $\rho(\Theta, r = 4R_*(\Theta))$ to the corresponding equatorial value, $\rho(\Theta = 90°, r = 4R_{\mathrm{eq}})$, for model B30-30 (KU) and different rotational velocities. Additionally, the results for the 2-D model with global force-multiplier parameters (B30-30 GL) are displayed (long dashes).

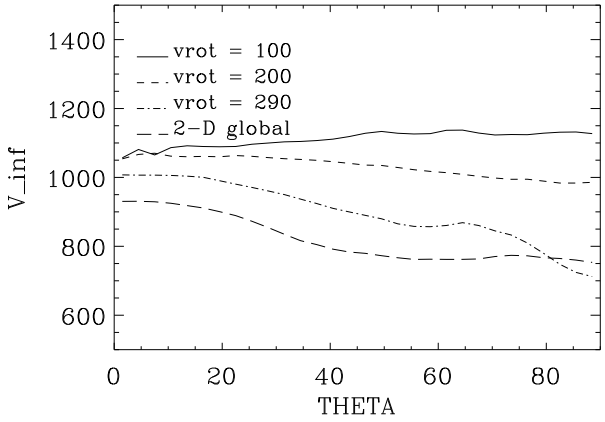

Fig. 23. As above, however for the terminal velocity, $v_\infty(\Theta)$.

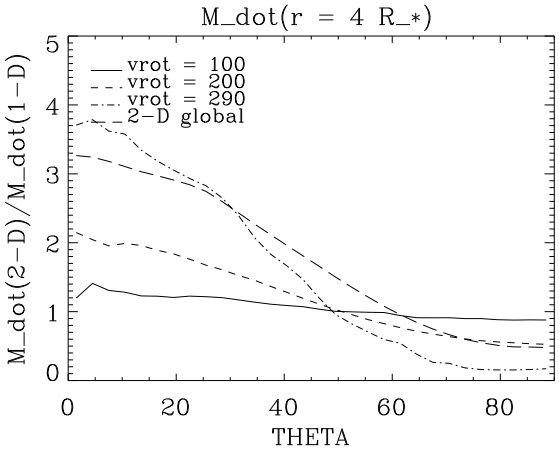

Fig. 24. As above, however ratio of local mass-loss rates $\dot{M}(\Theta, r = 4\, R_*)$ to the value resulting from 1-D self-consistent calculations, with $\dot{M}_{1-\mathrm{D}} \equiv \dot{M}(v_{\mathrm{rot}} = 0)$.

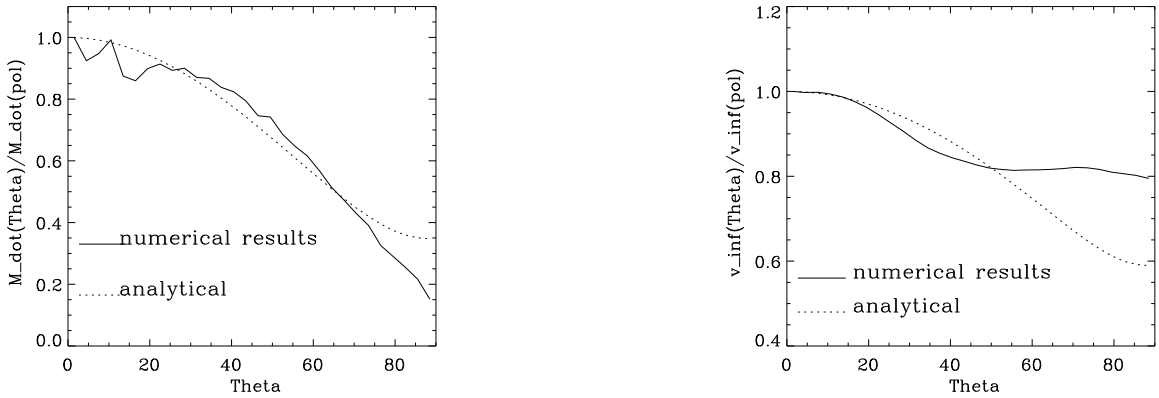

Fig. 25. Model B30-30 (GL). Left: Comparison of local mass-loss rates at the wind base, $\dot{M}(\Theta, r \approx R_*)$, normalized to the polar value, with analytical prediction Eq. 50. Right: The same for $v_\infty(\Theta)$, compared with Eq. 51.

The concentration of wind material toward the poles becomes more significant for $v_{\rm rot} = 200\,{\rm km\,s^{-1}}$ ($0.6\,v_{\rm crit}$), with $\rho(\Theta)/\rho_{\rm eq} \lesssim 5$ of the same order of magnitude as for models with global force-multiplier parameters and comparable rotation rates (cf. Petrenz 1999, Tab. 7.6). For extreme rotation rates ($v_{\rm rot} = 290\,{\rm km\,s^{-1}} \approx 0.86\,v_{\rm crit}$), the density contrast becomes very large ($\rho(\Theta)/\rho_{\rm eq} \lesssim 25$!). Note, that for all rotation rates the density contrast increases monotonically towards the pole, as expected for models with gravity darkening and negative values of v_Θ throughout the entire wind.

For comparison, Fig. 22 shows also the density contrast for our model with global force-multiplier parameters, B30-30 (GL). As discussed already in Sect. 7.2.1, this quantity is significantly smaller than for the self-consistent simulation, related mostly to processes near the equator. The evident difference points again to the importance of a self-consistent treatment, at least in the case of extreme rotation and if equatorial regions are of interest.

For the same model sequence, Fig. 23 displays the run of terminal velocity, $v_\infty(\Theta)$. For all rotation rates, it decreases from pole to equator.[13] The difference between its polar and equatorial value, however, is only small for all considered cases. ($\lesssim 100\,{\rm km\,s^{-1}}$). This is also true for the GL-model, where the terminal velocity changes by $\sim 150\,{\rm km\,s^{-1}}$ from pole to equator.

The most interesting quantity to be analyzed, of course, is the mass-loss rate. Before going in further details, we like to stress one of the major results of our present investigation, following already from the data listed in Tab. 3:

For any rotation rate, the surface-integrated mass-loss rate does almost not differ from the corresponding value for a non-rotating wind, $\dot{M}_{1-\rm D}$.

Due to gravity darkening, the equatorial mass-loss is diminished and the polar one enhanced, compared to the non-rotating case. Both effects, however, almost entirely compensate each other!

In Fig. 24, we have displayed the ratio $\dot{M}(\Theta)/\dot{M}_{1-\rm D}$ at $r = 4\,R_*$ for model B30-30 (KU) and different $v_{\rm rot}$. For $v_{\rm rot} \gtrsim 200\,{\rm km\,s^{-1}}$, this ratio varies by a factor of 4 or larger, with an according value for the contrast between polar and equatorial mass-loss rate. Such variations will have considerable impact on the formation of optical (or IR) recombination lines, and have to be accounted for in any analysis of observed line profiles, in particular for the determination of local and global mass-loss rates. Note, e.g., that for such large latitudinal variations ($\gtrsim 4$) of density or mass-loss rate, $\dot{M}$ derived by means of a conventional 1-D $\rm H_\alpha$-analysis might overestimate the actual value by $\lesssim 70\%$, as shown by PP96.

Before proceeding further, we will at first try to understand our finding $\dot{M}_{\rm total}(2-{\rm D}) \approx \dot{M}_{1-\rm D}$ by means of simple scaling arguments, which also show the validity and limitations of such relations.

For models with *constant* force-multiplier parameters, it is easy to show that the combined effect of centrifugal accelerations reducing the effective gravity on the one side and the dependence of flux on latitude due to gravity darkening on the other lead to a scaling of

$$\dot{M}(\Theta) = \dot{M}_{\rm polar}\left(1 - \left(\frac{v_{\rm rot}}{v_{\rm crit}}\right)^2 \sin^2\Theta\right) \qquad (50)$$

(cf. Owocki et al. 1997, Puls et al. 1999), which should be valid under the condition that the latitudinal redistribution of the mass-flux is irrelevant, or, in other words, v_Θ is small. To a lesser degree of precision, the terminal velocity should scale as

$$v_\infty(\Theta) = v_\infty^{\rm polar}\left(1 - \left(\frac{v_{\rm rot}}{v_{\rm crit}}\right)^2 \sin^2\Theta\right)^{\frac{1}{2}}. \qquad (51)$$

(A more accurate expression has been given by Puls et al. 1999, Eq. 4, which is, however, of no interest for the following discussion). Fig. 25 compares now these predictions with the results from our numerical simulation for model B30-30 (GL), which, because we have used global line-force parameters, just fulfills the above requirements. For the comparison of mass-loss rates as function of Θ, we have used the values in the *sonic region*

[13] Only for $v_{\rm rot} = 100\,{\rm km\,s^{-1}}$, v_∞ seems to increase marginally. This behaviour, however, is a numerical artifact since the model has not completely converged in the outer layers of the wind.

(with $\dot{M}_{\rm polar}(R_*) = 2.46 \cdot 10^{-6}\, M_\odot {\rm yr}^{-1}$), to avoid any disturbance by the latitudinal redistribution of matter. In particular, the polar mass-loss rate increases with r if gravity darkening is accounted for. For all models we have calculated, however, the radial variation of $\dot{M}$ has never exceeded a factor of two (cf. Tab. 3, column 4 vs. 5).

The comparison clearly shows that our numerical model is in close agreement with the analytical predictions, except for equatorial regions ($\Theta \gtrsim 80°$), where the actual mass-loss rate is lower, with a maximum deviation by a factor of two. Since the considered model has been entirely converged in the inner wind regions, we are convinced that this difference is real. We attribute it to the increasing influence of the radial dependence of the centrifugal acceleration, which is maximum in equatorial regions and has been neglected in the analytical approach leading to Eq. 50.[14] In agreement with the lower mass-loss rate in equatorial regions, the terminal velocities of our simulations are higher there.

Since Eq. 50 is valid at least for the major part of the lower wind and constant $k_{\rm CAK}$, α and δ, we can integrate $\dot{M}(\Theta)$ over $\sin\Theta\,{\rm d}\Theta$ and find for the total mass-loss rate

$$\dot{M}_{\rm total} = \dot{M}_{\rm polar}(R_*) \left(1 - \frac{2}{3}\left(\frac{v_{\rm rot}}{v_{\rm crit}}\right)^2\right), \qquad (52)$$

which is independent of radius due to its global conservation.

We have to relate now $\dot{M}_{\rm polar}$ with the appropriate 1-D value. The polar radius of our 2-D models corresponds to the 1-D stellar radius and the local gravities are equal by definition. Thus, we have to account only for the different illuminating fluxes by means of the well-known scaling relations for radiatively driven winds (e.g., Puls et al. (1996),

$$\dot{M}_{\rm polar}(R_*) = \dot{M}_{\rm 1-D}\left(\frac{T_{\rm eff}(0°)}{T_{\rm eff,1-D}}\right)^{\frac{4}{\alpha'}}, \qquad (53)$$

with $\alpha' = \alpha - \delta$. Utilizing finally the von Zeipel constant Σ as given by CO (their Eq. 32, resulting from a fit to numerical calculations), and the von Zeipel relation for $\Theta = 0°$, we have approximately

$$\dot{M}_{\rm total}({\rm 2-D}) = \dot{M}_{\rm 1-D}\,\frac{1 - \frac{2}{3}\left(\frac{v_{\rm rot}}{v_{\rm crit}}\right)^2}{1 - \frac{0.2}{\alpha'}\left(\frac{v_{\rm rot}}{v_{\rm crit}}\right)^2} \qquad (54)$$

which should be valid for $v_{\rm crit}/v_{\rm rot} \lesssim 0.8$. Inserting typical values for $\alpha' = 0.6...0.5$ in the OB-star domain, it turns out that the fraction in the above equation has a minimum value of order 0.8, if the complete expression for Σ (accounting for higher orders of $v_{\rm rot}/v_{\rm crit}$) is used for highest rotation rates.

Thus, our finding $\dot{M}_{\rm total}({\rm 2-D}) \approx \dot{M}_{\rm 1-D}$ can be understood at least for models with constant $k_{\rm CAK}$, α and δ. With respect to our self-consistent simulations, the above analysis is hampered by the assumption of constant force-multiplier parameters. Anyhow, for almost all calculated models the ratio of $\dot{M}_{\rm total}$ to $\dot{M}_{\rm polar}(R_*)$ follows the analytical prediction (52), with a value of roughly 0.5 for $v_{\rm rot} = 0.85 v_{\rm crit}$ (cf. Tab. 3, column 4 vs. 7). This on a first glance astonishing result is primarily related to the fact that, close to the surface, the major impact of our self-consistent approach concerns the equatorial regions, whereas the differences in polar regions are minor (cf. Sect. 7.2.1 and Fig. 27). Since the strongly reduced mass-loss in equatorial regions has only small influence on the total one, the validity of Eq. 52 and consequently Eq. 54 is explained also for the self-consistent models. In the outer regions, of course, the differences become larger, again mostly near the equator (Fig. 24). However, these differences do not play any role for the total mass-loss: Once calculated at the wind base, it is known throughout the wind due to its global conservation.

As a consequence of the above arguments, the relation $\dot{M}_{\rm total}({\rm 2-D}) \approx \dot{M}_{\rm 1-D}$ should be valid as long as there is no dramatic difference between polar and intermediate latitude ionization structure. For models with gravity darkening, this seems to be almost impossible (provided that the continuum is optically thin), and we actually have found the above "identity" not only for models at 20,000 K, but also for models of different spectral type, e.g., for O-stars (cf. Petrenz 1999).[15]

One might argue that our finding is self-evident, since the decisive factor controlling the total mass-loss is the total luminosity, being conserved under rotation. However, the additional dependence of $\dot{M}$ on effective mass modified by centrifugal acceleration is non-negligible, and is compensated for only if gravity darkening is taken into account. Otherwise, the scaling for $\dot{M}$ as function of Θ behaves differently (actually, directed in the opposite sense, with the bracket in Eq. 50 modified by an exponent of $(1 - 1/\alpha') \approx -1$), and it is easy to show that in this case $\dot{M}_{\rm total}$ becomes larger than for corresponding non-rotating winds.

We can continue now with our comparison of latitudinal wind structure as function of rotation rate. One of the most striking features is the significant enhanced density contrast when increasing $v_{\rm rot}$ from $200\,{\rm km\,s^{-1}}$ to $290\,{\rm km\,s^{-1}}$, cf. Fig. 22.

This different morphology of intermediate and rapidly rotating winds is, of course, the consequence of the drastically diminished temperature contrast between equator and pole for the model with $v_{\rm rot} = 200\,{\rm km\,s^{-1}}$. In particular, the equatorial temperature ($T_{\rm eff,eq} = 18150$ K) is much closer to the nominal value than for the rapid rotator ($T_{\rm eff,eq} = 14600$ K).

Thus, FeII with its many lines is much less important at the equator (see Fig. 26 for the ionization fractions of iron), and the latitudinal variations of $N_{\rm eff}(Z)$ at the wind base have almost vanished, as displayed in Fig. 27. As well, also the radial variation of $N_{\rm eff}(Z, r)$ is less significant than for $v_{\rm rot} = 290\,{\rm km\,s^{-1}}$: $N_{\rm eff}(Z, r)$ becomes a mildly and monotonically decreasing function of radius at all latitudes, also for carbon in the equatorial plane.

[14] In agreement with this argument, different models with global force-multipliers not discussed here show a weaker equatorial discrepancy for lower and a larger one for higher rotation rates, cf. Petrenz (1999, Fig. 7.15).

[15] The only exception from the rule concerning the model grid presented in Tab. 1 is model B60-30, and will be commented on in the next section.

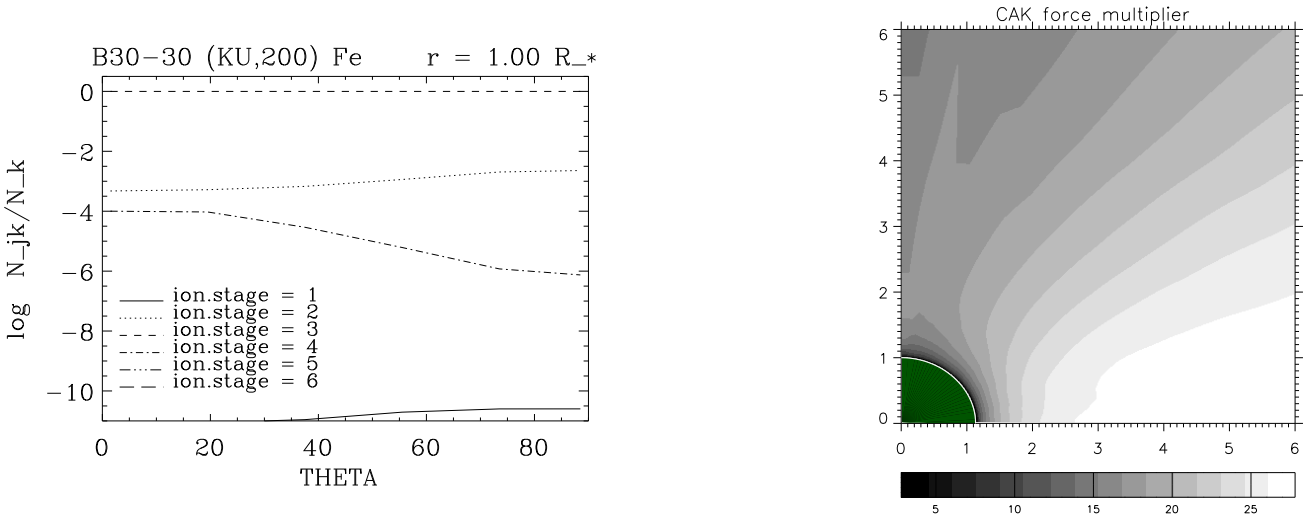

Fig. 26. Model B30-30 for $v_{\rm rot} = 200\,\mathrm{km\,s^{-1}}$. Ionization fractions of iron at the wind base (left); force multiplier $M(\Theta, r)$ (right).

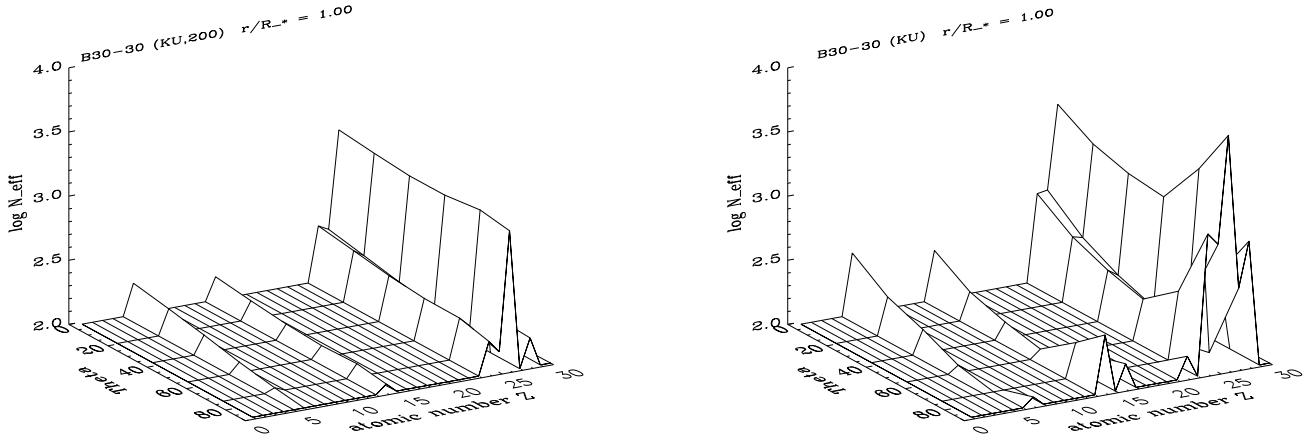

Fig. 27. Model B30-30 (KU): $N_{\rm eff}(\Theta, Z)$ at the wind-base Left: $v_{\rm rot} = 200\,\mathrm{km\,s^{-1}}$; right: $v_{\rm rot} = 290\,\mathrm{km\,s^{-1}}$.

Since $N_{\rm eff}(r, \Theta)$ is now a well-behaved function and also the illuminating flux ($\propto T_{\rm eff}^4(\Theta)$) varies to a much lesser extent, the wind is by far not as asymmetric as for $v_{\rm rot} = 290\,\mathrm{km\,s^{-1}}$.

Also the force multiplier M displays a monotonic behaviour, and has a much lower maximum ($\lesssim 25$ for $\Theta = 90°$, Fig. 26) than for the rapid rotator ($M \lesssim 80$, Fig. 13). This brings us finally back to the question concerning the non-monotonic polar variation of M for the latter model, as shown in Fig. 13: Starting at the poles, M initially increases as function of Θ due to the increasing evaporation of the wind ($M \propto t_r^{-\alpha} \propto (\rho/\mathrm{d}v/\mathrm{d}r)^{-\alpha}$). Near the equatorial plane, however, both the stellar oblateness and the slower radial expansion imply a larger value of t_r, and $M(t_r)$ decreases again, although $N_{\rm eff}$ grows in accordance with the increasing contribution from FeII. Since for lower rotation rates the polar variation of both the flux and the effective line number is much lower, the "density effect" remains the stronger one, and $M(t_r)$ does not change its behaviour.

7.2.5. Dependence of wind properties on stellar luminosity

In order to estimate possible *maximum* effects of rotation on the application of radiation driven wind theory to stellar evolution calculations and the wind-momentum luminosity relation, we will finally discuss the dependence of wind properties on luminosity, by means of *rapidly* rotating models ($v_{\rm rot} \approx 0.85\, v_{\rm crit}$).

To this end, we have calculated a sequence of stellar winds from models at $T_{\rm eff} = 20000$ K and different luminosities (cf. Tab. 1). The most important numerical results have been listed in Tab. 3.

Fig. 28 displays the ratio of polar to equatorial mass-loss as function of luminosity. In agreement with our previous results, we find also here a clearly prolate wind structure in all considered cases, with a maximum ratio $\lesssim 25$ for main sequence models with lowest mass-loss rates. This contrast decreases towards highest luminosities, since the latitudinal ionization gradients of the CNO group are most effective for the thinner winds (see Sect. 7.2.3, Fig. 21). For larger wind densities, the mass-loss from more or less all latitudes is controlled

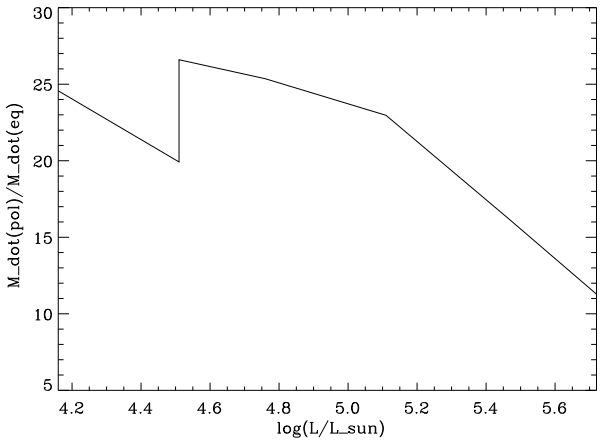

Fig. 28. Ratio of polar to equatorial mass-loss rate as function of stellar luminosity, for rapidly rotating B-star models with $T_{\rm eff} = 20,000$ K ($v_{\rm rot} = 0.85 v_{\rm crit}$, ratio evaluated at 4 $R_{\rm p}$ and 4 $R_{\rm eq}$, respectively). The non-monotonic behaviour at $\log(L/L_\odot) = 4.5$ is due to the difference in stellar mass for the two models B15-10 and B15-15.

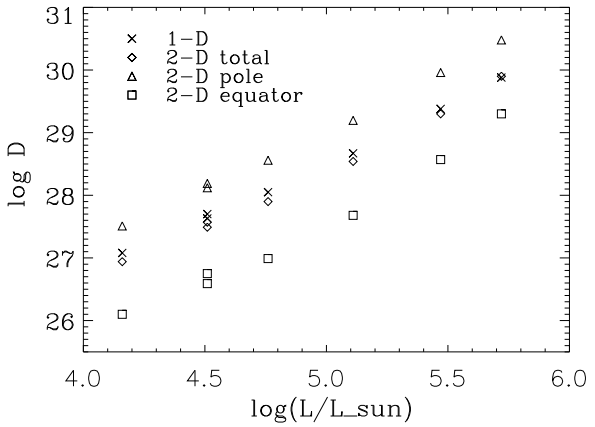

Fig. 29. Wind-momentum luminosity relation for the same models as in Fig 28. Compared are the modified wind-momenta $D = \dot{M} v_\infty (R_*/R_\odot)^{1/2}$ resulting from our 2-D simulations with mass-loss rate $\dot{M} = \dot{M}_{\rm total}, \dot{M}_{\rm p}, \dot{M}_{\rm eq}$, respectively, and from corresponding (self-consistent) 1-D models ($v_{\rm rot} = 0$). See text.

by iron, displaying a less significant ionization shift and thus favourizing a reduced density contrast. (To clarify this trend unambiguously, we have included also models for B-supergiant winds which actually should become optically thick in the Lyman continuum ($\log L/L_\odot \gtrsim 5.4$, cf. Tab. 4). For these models, our simplified non-LTE description is certainly no longer correct, and the bi-stability effect might begin to operate.)

If we compare the ratio of surface-integrated 2-D mass-loss rate $\dot{M}_{\rm total}$ to the corresponding value $\dot{M}_{1-\rm D}$ for the non-rotating star, we find, in agreement with the results from our reference model and the reasoning given in the previous section, for almost all models a close agreement, except for the one with highest luminosity. The borderline (at $T_{\rm eff} = 20000$ K) appears to be situated at $\log(L/L_\odot) \approx 5.3$, from where on the discrepancy between $\dot{M}$ and $\dot{M}_{1-\rm D}$ becomes larger, owing to the strongly enhanced Thomson acceleration over the poles. (The Γ term is no longer negligible for such models, becoming a strongly increasing function of latitude because of the polewards increase of $T_{\rm eff}(\Theta)$, cf. also Sect. 3.3)

In consequence, the total mass-loss rate might become larger than $\dot{M}_{1-\rm D}$ at highest luminosities, by roughly a factor of two. This result, however, has to be taken with caution, since we have neglected effects due to the optically thick Lyman continuum.

Consequences for the wind-momentum luminosity relation. The mutual compensation of polar and equatorial mass-loss in comparison with the 1-D value even for rapid rotators implies some interesting consequences for the application of the wind-momentum luminosity relation, as displayed in Fig. 29.

This figure shows the modified wind-momentum $D = \dot{M} v_\infty (R_*/R_\odot)^{1/2}$ as defined by Kudritzki et al. (1995), plotted against stellar luminosity, where the values for $\dot{M}$ and v_∞ have been taken for the following cases (for simplicity, we have always used $R_* = R_{\rm p}$): For the polar and equatorial wind, for the global wind with total mass-loss rate $\dot{M}_{\rm total}$ and some average value $< v_\infty >$ (remember that in most cases $v_\infty(\Theta)$ varies only marginally), and for the according self-consistent 1-D model.

In all four cases, the mass-loss rate has been evaluated at $r = 4\,R_*$, where the polar density contrast has already saturated to its maximum value. By means of this diagram, we can estimate the *maximum* contamination of empirically derived WLRs due to rotation: If the wind is observed under arbitrary inclination, the polar and equatorial value of $\log D$ may differ by up to 1.5 dex, thus implying a considerable scatter in the observed WLR. This difference becomes smaller for higher stellar luminosities, because of the smaller mass-loss/density contrast for denser winds, as discussed above.

Note, however, that this maximum deviation is certainly overestimated if the mass-loss rate is derived from $\rm H_\alpha$. Firstly, most of this emission originates from the inner wind ($r \approx 1.0 \ldots 1.5\,R_*$), where the density contrast is smaller than in the outer wind, even for extreme rotation rates. A typical number for this reduced density contrast in the lower wind is a factor of four (cf. Petrenz 1999, Tab. 8.1), so that the above maximum scatter is reduced to a value of 0.9 dex. Secondly, the observed $\rm H_\alpha$ emission consists of a superposition of polar *and* equatorial emission. Even if one observes the star directly pole-on, there will be always a lower emission from equatorial regions (and vice versa for equator-on observations), which partly compensates for the deviation from the emission predicted by simple 1-D wind models. Only detailed line synthesis calculations (e.g., as performed by PP96 for the case of wind-compressed zone models) will finally allow to check the actual scatter arising in the WLR, if the winds were observed either pole-on or equator-on.

A very promising result, however, is the very good agreement of $\log D$ derived for the global wind ($\dot{M}_{\rm total}, < v_\infty >$) and the according self-consistent 1-D model. Note especially that even for the model of highest luminosity (with $\dot{M}_{\rm total} \approx$

$2 \cdot \dot{M}_{1-\mathrm{D}}$) both quantities agree, due to the compensation by a lower terminal velocity. In so far, it is evident that the most important scaling relation relying on the principal mechanism, radiative driving, is not affected if the *global* wind is considered: *The primary effect of rotation is "only" a redistribution of matter*. Thus, the assumption of non-rotating, spherical winds is a reasonable simplification if a description of *global* quantities is aimed at, e.g., in the context of (1-D) stellar evolutionary models, and the models are situated not too close to the Eddington or Ω limit.

8. Summary, conclusions and future work

In this paper, we have extended previous 2-D models of line-driven winds from rotating hot stars by accounting for the dependence of ionization structure and occupation numbers on local physical properties (density, velocity field) and the non-local stellar radiation field (variation with temperature and frequency).

To this end, we have formulated for the first time an approximate non-LTE description of 2-D winds. Since the exact dependence of the incident radiation field on direction and frequency (if gravity darkening is considered) cannot be accounted for simultaneously because of limited computational capacities and time, we have proposed the concept of a "mean irradiating atmosphere". This Ansatz allows, in an approximate way, to consider the *frequency dependence* of the incident photospheric radiation field, which most importantly determines the local ionization equilibrium, at least if realistic flux distributions are used. (For stellar surfaces emitting locally, i.e., as function of Θ, a black body spectrum, the mean radiation temperature in the wind varies only weakly with frequency.)

In order to describe this frequency dependence of T_{rad} for all values of (Θ, r) in a satisfactory way, we have defined local, frequency-independent mean effective temperatures $\overline{T}_{\mathrm{eff,cont}}$, which, in connection with the appropriate gravitational acceleration, just define the above mean irradiating atmospheres and thus the frequency-dependent flux distributions in $\boldsymbol{r}$. It has been shown that $\overline{T}_{\mathrm{eff,cont}}\,(\Theta, r)$ varies much stronger with latitude than with distance from the star and decreases, for all isocontours of r, monotonically from pole to equator, since the influence of the radiation field from the corresponding footpoint $(\Theta, R_*(\Theta))$ is significant at all radii.

By means of the resulting flux-distributions and local conditions, we have calculated 2-D NLTE occupation numbers, force-multipliers and according force-multiplier parameters, as function of (Θ, r). The hydrodynamic models constructed in this way are entirely self-consistent, and converge to a stationary solution in the same way as models for globally constant k_{CAK}, α, δ, with the only difference that the physical convergence time can be larger by a factor of 5...10.

For mass-loss rates $\dot{M} \lesssim 10^{-9}\,M_\odot \mathrm{yr}^{-1}$, the procedure as outlined in this paper is not suitable for quantitative calculations (due to saturation effects arising from all lines becoming optically thin), although a generalization would be easily possible. Since, however, it is rather questionable whether a one-component plasma model is valid for such extremely thin winds at all, we have restricted our investigation to winds with mass-loss rates $\dot{M} \gtrsim 10^{-8}\,M_\odot \mathrm{yr}^{-1}$. For these winds, our algorithm to parameterize the force multiplier yields a very satisfactory accuracy of $5 \ldots 10\%$ (considering the complexity of the problem), if compared with the "exact" values found from summing up the individual line accelerations.

Our study was aimed at an estimate of maximum effects arising from rotation, in particular with respect to the *differential* behaviour as function of latitude, if compared with previous models allowing only for predefined, global force-multipliers. Thus, we have concentrated on rapidly rotating B-star winds, since in this spectral range the ionization structure is much more sensitive to local conditions and the variation of the radiation field than at other temperatures, e.g., for O-stars. For all models of our grid, which has been constructed to allow for a variety of luminosities, we have checked whether the Lyman continuum is optically thin, a prerequisite to definitely inhibit any bi-stability effect (to be investigated in a forthcoming paper, see below).

In all considered cases, we found a *prolate* wind structure, if gravity darkening is accounted for, with maximum ratios of polar to equatorial mass-loss rate up to a factor of 30. Non-radial components of the line (and continuum) acceleration inhibit any wind compression and cause negative polar velocities of order $v_\Theta \approx -40 \ldots -80\,\mathrm{km\,s}^{-1}$. Even if the non-radial line force components are neglected, a globally prolate wind is created, however with a moderately compressed disk in the equatorial plane.

Thus, the "$\varkappa$-effect" suggested by Maeder (1999, cf. Sect. 1) is actually *not* occuring, at least for winds with an optically thin continuum. Since we have considered a temperature regime with maximum effects of ionization and have also understood the physical origin why a consistent NLTE approach gives rise to an even enhanced prolate wind morphology (Sect. 7.2.1 and below), we are convinced that this statement does not only apply to the limited spectral range considered here, but also at least for the complete OB-star range. (A-type winds might deserve a special investigation.)

For B-star winds with significant mass-loss ($\dot{M} \gtrsim 10^{-7}\,M_\odot \mathrm{yr}^{-1}$), the density contrast between the flow over the poles and in the equatorial plane reaches values of order $\rho_{\mathrm{p}}/\rho_{\mathrm{eq}} \lesssim 15$. This ratio grows with rotation rate and decreases from thin winds ($\dot{M} \gtrsim 10^{-8}\,M_\odot \mathrm{yr}^{-1}$, $\rho_{\mathrm{eq}}/\rho_{\mathrm{p}} \lesssim 20 \ldots 30$) to denser ones (B-supergiants, $\dot{M} \gtrsim 10^{-6}\,M_\odot \mathrm{yr}^{-1}$, $\rho_{\mathrm{p}}/\rho_{\mathrm{eq}} \lesssim 5$).

For our reference model B30-30, we have also calculated the wind structure which would arise if we neglect any 2-D effects with respect to occupation numbers and force-multipliers. For this purpose, we estimated global averages for k_{CAK}, α and δ from our self-consistent solution. The according model shows a density contrast $\rho_{\mathrm{p}}/\rho_{\mathrm{eq}}$ of only half of the value in the original one. Compared to this "zero order" approximation of 2-D winds, our self-consistent parameterization leads to a moderately enhanced concentration of wind material over the poles

and a significant reduction in the equatorial plane, as a consequence of the ionization effects summarized in the following.

Inspecting the contribution from various elements to the line force, the dominant role of iron in winds with considerable densities is obvious. The CNO group is most important (but still much less effective than iron) in the equatorial wind, since the flow evaporates for larger co-latitudes Θ (at constant r), and the meta-stable iron lines do not accelerate the matter as effectively as in the denser polar wind. For an illumination by Kurucz fluxes, FeIII provides the major part of acceleration. Only for extremely rapid rotators ($v_{\rm rot} \gtrsim 0.85\,v_{\rm crit}$), FeII becomes most decisive in the coolest regions close to the equator, due to the significant reduction of the mean radiation temperature induced by gravity darkening ($\overline{T}_{\rm eff,cont}\,(90^\circ) \approx 15000\,{\rm K}$).

The *radial* variation of the ionization fractions over the pole is determined by the decrease of both effective wind density and $\overline{T}_{\rm eff,cont}$ with increasing distance from the star. Both effects act on the ionization equilibrium in the opposite way and thus have a stabilizing effect, with the consequence of rather frozen-in (however sometimes non-monotonic) ionization fractions. In contrast, the radially decreasing density and the increasing mean radiation temperature near the equator act in parallel and lead to a monotonic increase of the ionization equilibrium towards higher stages, which have, on the average, fewer lines and thus provide less acceleration. This different behaviour over the poles and in the equatorial plane is the final reason for the enhanced polar density contrast in self-consistent wind solutions, and should be valid in the complete OB-star range (though with a different degree of significance), as pointed out above.

We have also investigated briefly the importance of using realistic flux distributions by comparing our self-consistent models to winds illuminated by Planck fluxes. In such cases, the ionization equilibrium of the most contributing elements is shifted, on the average, to one stage higher than for Kurucz fluxes. In consequence, the winds become significantly thinner (with increased polar density contrast), and the CNO group becomes crucial for the acceleration. Due to the significant contribution from carbon – CIII close to the surface, being converted to CIV for larger radii in the equatorial region –, such models even show a larger equatorial terminal velocity, in contrast to all other models calculated with Kurucz fluxes where the polar value is the largest. (For all our models, however, the difference between polar and equatorial v_∞ is by far not as significant as for WCZ models, with $v_\infty(90^\circ) \lesssim 0.3\,v_\infty(0^\circ)$, cf. Petrenz 1999.)

Our most important finding with regard to the influence of rotation on *global* wind properties is that the total mass-loss rate $\dot{M}_{\rm total}$ deviates from its 1-D value $\dot{M}_{\rm 1-D}$ (for $v_{\rm rot} = 0$) by at most 10...20 %. This turned out to be true even for the highest rotation rates considered here ($v_{\rm rot} \lesssim 0.85\,v_{\rm crit}$), with the only exception of winds from supergiants close to the Eddington-limit, where differences up to a factor of 2 become possible.

The enhanced mass-loss over the pole is compensated for by the reduced density in the equatorial plane, both effects resulting from gravity darkening. Since, under the assumption of an optically thin continuum, the ionization effects *for a large part of the stellar surface* are moderate (for equatorial regions, they are decisive, of course), and the total luminosity remains conserved under rotation, these small changes of the total 2-D mass-loss rate, compared to the non-rotating wind, are plausible, and have been explained by using some relevant scaling relations.

In conclusion, a quantitatively correct description of line-driven winds from rapidly rotating hot stars requires a self-consistent parameterization of the line force in all those cases, where the variation of $T_{\rm rad}\,(\Theta)$ at the stellar surface can induce a (significantly) stratified ionization equilibrium. For the hotter O-stars, this is possible only for large rotation rates, whereas in the B-star domain also moderate rates have to be included, especially for lower luminosities with thinner winds.

The resulting ionization pattern varying as function of latitude, if significant, implies a dependence of the spectral signature of corresponding lines on stellar inclination. Future effort on decent spectrum synthesis calculations is required to prove or disprove the theoretical predictions given in this paper.

In Sect. 7.2.5, we have investigated also the "worst-case" scenario with respect to the application of the WLR, if the winds are rapidly rotating, but mass-loss rates are derived by a 1-D analysis. Although a maximum scatter of 1.5 dex seems to be apparent, this scatter is reduced significantly if a mass-loss indicator is used which depends "only" on the lower wind conditions (e.g., $\rm H_\alpha$). Since the density contrast is smaller in those regions than in the outer wind (by roughly a factor of four, with a minimum value of order $1 - (v_{\rm rot}/v_{\rm crit})^2$, cf. Eq. 50), and since, as already discussed, the *total* line profile is influenced both from polar and equatorial regions, the actual contamination by rotational effects is definitely smaller.

PP96 have estimated the maximum error in the derivation of $\dot{M}$ introduced by the standard 1-D analysis of $\rm H_\alpha$ to $\lesssim 70\%$. In their analysis, they used the simple analytic WCZ model with compression factors $\rho_{\rm eq}/\rho_{\rm p} \lesssim 4$. Thus, this estimate does not necessarily correspond to all other wind models one might imagine. However, since the density contrast in our self-consistent simulation for a rotation speed $v_{\rm rot} = 200\,{\rm km\,s^{-1}}$ is of the same order of magnitude as found in the WCZ model, the same degree of contamination should be expected.

Therefore, the influence of stellar rotation on mass-loss rates derived from $\rm H_\alpha$ is, in most cases, a second-order effect, regarding the fact that any application of the WLR uses the values of a large sample of stars, and, moreover, rapid rotators can be excluded from those samples easily unless they are observed pole-on. Note, however, that erroneously determined mass-loss rates for individual objects may have severe consequences with respect to their evolutionary status: An error in $\dot{M}$ of only a factor of two is able to alter the evolution history drastically, as shown by Maeder (1991).

Future work. We have to admit that a number of aspects have been simplified in this investigation. In a "perfect" description,

line-overlap and line-shadowing neglected here might introduce additional complications, as well as the impact of X-rays on the ionization equilibrium in the outer wind. In particular, the consequences of an optically thick Lyman continuum and the bi-stability effect on the wind dynamics have to be considered and will be discussed in a forthcoming paper.

A further phenomenon which is important both for the diagnostics of stellar winds and their dynamics is the presence or absence of clumps in the wind. If they actually exist and their spatial scale is small, the line acceleration $g^{\rm lines} \sim 1/\rho^{\alpha}$ could be drastically reduced and the inertial terms might become decisive again. Thus, the WCD/WCZ model might be resurrected. Whether final results of a first study on the influence of the line instability in rotating winds (Owocki 1999) support this scenario, has still to be awaited for. Finally, magnetic fields, *if* present with sufficient strength, could again alter our conclusions given above.

Of course, any improvement of the theory (especially regarding the considerable effort required) makes only sense if the models can be discriminated by a comparison with observations.

Thus, a re-investigation of previously analyzed winds from rapidly rotating early-type stars by means of *systematically refined* hydrodynamic wind models seems to be desirable. In particular, the determination of inclination, i.e., of *absolute* rotational velocities $v_{\rm rot}$, remains the major problem and is presently possible only for few objects (e.g., the rapid rotator HD 93521, which exhibits spectral signatures that indicate a wind-compressed equatorial disk – despite all theoretical arguments against this scenario, cf. Bjorkman et al. 1994 and Massa 1995).

Fortunately, the different theoretical ideas and models yield also different results regarding the density structure. For a final clarification, an analysis of several spectral ranges is desirable to gain further and complementary insight (e.g., by infrared lines or IR/radio continua). In these spectral ranges, the line/continuum formation process takes place at much larger distances from the star as for the H_{α} emission, and the density contrast, at least present in the theoretical simulations, is largest. Finally, the *direct* observation of the wind morphology by means of (optical) long-baseline interferometry is supposed to make excellent progress within the next years.

Acknowledgements. We like to thank Prof. Dr. S. Owocki for continuous and engaged collaboration. This work has been supported by the German *Deutsche Forschungsgemeinschaft, DFG*, project number Pu 117/2–1/2 and partly also by the *DLR*, project FKZ 50 OR 9413 6.

All numerical simulations were performed on the basis of the ZEUS-2D code developed at the National Center for Supercomputing Applications (NCSA) at the University of Urbana, Illinois.

References

Abbott, D. C., 1980, ApJ 242, 1183
Abbott, D. C., 1982, ApJ 263, 723
Abbott, D. C., Lucy, L. B., 1985, ApJ 288, 679
Anders, E., Grevesse, N., 1989, Geochim. et Cosmochim. Acta 53, 197
Batchelor, G. K., 1967, An Introduction to Fluid Dynamics, Cambridge University Press, Cambridge
Bjorkman, J. E., Cassinelli, J. P., 1993 (BC), ApJ 409, 429
Bjorkman, J. E., Ignace, R., Tripp, T.M., Cassinelli, J. P., 1994, ApJ 435, 416
Bjorkman, J. E., 1999. In: Variable and Non-spherical Stellar Winds in Luminous Hot Stars, IAU Coll. 169, eds. B. Wolf, O. Stahl, A. W. Fullerton, Springer, Heidelberg, p. 121
Cassinelli, J.P., Ignace, R., Bjorkman, J.E., 1995. In: Wolf-Rayet Stars: Binaries, Colliding Winds, Evolution, IAU Symp. 163, eds. K. A. van der Hucht & P. M. Williams, Kluwer, Dortrecht, p. 191
Castor, J. I., 1974, MNRAS 169, 279
Castor, J. I., Abbott, D. C., Klein, R. I., 1975 (CAK), ApJ 195, 157
Collins II, G. W., 1963, ApJ 138, 1134
Collins II, G. W., 1965, ApJ 142, 265
Conti, P. S., Ebbets, D., 1977, ApJ 213, 438
Cranmer, S. R. , Owocki, S. P., 1995 (CO95), ApJ 440, 308
Donati, J.-F., 1998. In: Cyclical Variability in Stellar Winds, ESO Astrophysical Symposia, eds. L. Kaper & A. W. Fullerton, p. 212
Feldmeier, A., 1995, A&A 299, 523
Friend, D., Abbott, D. C., 1986, ApJ 311, 701
Gayley, K. G., 1995, ApJ 454, 410
Gayley, K. G., Owocki, S. P.: 2000, in prep.
Glatzel, W., 1998, A&A 339, L5
Grevesse, N., Noels, A., Sauval, A. J., 1996. In: Cosmic abundances, eds. S. S. Holt & G. Sonneborn, PASPC 99, 117
Grinin, A., 1978, Sov. Astr. 14, 113
Herrero, A., Kudritzki, R.-P., Vilchez, J. M., Kunze, D., Butler, K., Haser, S., 1992, A&A 261, 209
Herrero, A., Puls, J., Villamariz, M. R.,A&A , in press
Ignace, R., Cassinelli, J. P., Bjorkman, J. E., 1996, ApJ 459, 671
Käufl, H.U., 1993, A&A 272, 452
Kippenhahn, R., Weigert, A., 1991, Stellar Structure and Evolution, 2nd Printing, Springer-Verlag Berlin, Heidelberg
Koninx, J.-P., 1992, PhD thesis, University Utrecht
Kudritzki, R.-P., Pauldrach, A. W. A., Puls, J., Abbott, D. C., 1989, A&A 219, 205
Kudritzki, R.P., Lennon, D. J., Puls, J., 1995. In: Science with the VLT, ESO Astrophysics Symposia, eds. J.R. Walsh & I.J. Danziger, Springer, Heidelberg, p. 246
Kudritzki, R.-P., 1997, Quantitative Spectroscopy of the Brightest Blue Supergiant Stars in Galaxies. In: Proc. 8th Canary Winter School: Stellar Astrophysics for the Local Group - A first step to the Universe, eds. A. Aparicio & A. Herrero, Cambridge University Press, 149
Kudritzki, R.-P., Springmann, U., Puls, J., Pauldrach, A. W. A., Lennon, M., 1998 (Ku98). In: Boulder-Munich II: Properties of hot, luminous stars, ed. I. D. Howarth, PASPC 131, 299
Kudritzki, R.-P., Puls, J., Lennon, D. J., Venn, K. A., Reetz, J., et al., 1999, A&A 350, 970
Kurucz, R. L., 1992, Rev. Mex. Astrofis., 23, 45
Lamers, H. J. G. L. M., Pauldrach, A. W. A., 1991, A&A 244, L5
Lamers, H. J. G. L. M., Vinck, J. S., de Koter, A., Cassinelli, J. P., 1999. In: Variable and Non-spherical Stellar Winds in Luminous Hot Stars, IAU Coll. 169, eds. B. Wolf, O. Stahl, A. W. Fullerton, Springer, Heidelberg, p. 159
Langer, N., Hamann, W.-R., Lennon, M., Najarro, F., Pauldrach, A. W. A., et al., 1994, A&A 290, 819
Langer, N., 1998, A&A 329, 551
Langer, N., Heger, A., 1998. In: Boulder-Munich II: Properties of hot, luminous stars, ed. I. D. Howarth, PASPC 131, 76

Lucy, L. B., Solomon, P., 1970, ApJ 159, 879
MacFarlane, J. J., Waldron, W. L., Corcoran, M. F., Wolff, M. J., Wang, P., et al., 1993, ApJ 419, 813
MacLow, M.-M., Langer, N., Garcia-Segura, G., 1996, Bull. American Astron. Soc. 188, 38.06
Maeder, A., 1991. In: Proc. of STScI 5, ed. C. Leitherer, p. 97
Maeder, A., 1998. In: Boulder-Munich II: Properties of hot, luminous stars, ed. I. D. Howarth, PASPC 131, 85
Maeder, A., 1999, A&A 347, 185
Massa, D., 1995, ApJ 438, 376
Mathys, G., 1999. In: Variable and Non-spherical Stellar Winds in Luminous Hot Stars, IAU Coll. 169, eds. B. Wolf, O. Stahl, A. W. Fullerton, Springer, Heidelberg, p. 95
Mazzali, P. A.,, 1990, A&A 238, 191
McCarthy, J. K., Lennon, D. J., Venn, K. A., Kudritzki, R. P., Puls, J., et al., 1995, ApJ 455, L135
McCarthy, J. K., Kudritzki, R.-P., Lennon, D. J., Venn, K. A., Puls, J., 1997, ApJ 482, 757
Meynet, G., 1998. In: Boulder-Munich II: Properties of hot, luminous stars, ed. I. D. Howarth, PASPC 131, 96
Mihalas, D., 1978, Stellar Atmospheres, 2nd Edition, W. H. Freeman and Company, San Francisco
Owocki, S. P., Castor J. I., Rybicki, G. B., 1988, ApJ 335, 914
Owocki, S. P., 1991. In: Stellar atmospheres: Beyond classical models, NATO ASI Series C 341, eds. L. Crivellari, I. Hubeny, D. G. Hummer, Kluwer, Dordrecht, p. 235
Owocki, S. P., Cranmer, S. R., Blondin, J. M., 1994 (OCB), ApJ 424, 887
Owocki, S. P. , Cranmer, S. R., Gayley, K. G., 1996, ApJ 472, L115
Owocki, S. P. , Cranmer, S. R. , Gayley, K. G., 1997. In: Proc. of Workshop on B[e] stars, Paris 1997, ed. A. Hubert, Kluwer, Dortrecht
Owocki, S. P., Gayley, K. G., Cranmer, S. R., 1998. In: Boulder-Munich II: Properties of hot, luminous stars, ed. I. D. Howarth, PASPC 131, 237
Owocki, S.P., 1999. In: Variable and Non-spherical Stellar Winds in Luminous Hot Stars, IAU Coll. 169, eds. B. Wolf, O. Stahl, A. W. Fullerton, Springer, Heidelberg, p. 294
Pauldrach, A. W. A., Puls, J., Kudritzki, R. P., 1986 (PPK), A&A 164, 86
Pauldrach, A. W. A., 1987, A&A 183, 295
Pauldrach, A. W. A., Puls, J., 1991, A&A 237, 409
Pauldrach, A. W. A., Kudritzki, R. P., Puls, J., Butler, K., Hunsinger, J., 1994, A&A 283, 525
Pauldrach, A. W. A., Lennon, M., Hoffmann, T., Sellmaier, F., Kudritzki, R.-P., et al., 1998. In: Boulder-Munich II: Properties of hot, luminous stars, ed. I. D. Howarth, PASPC 131, 258
Petrenz, P., 1994, diploma thesis, Ludwig-Maximilians-University Munich
Petrenz P., Puls, J., 1996 (PP96), A&A 312, 195
Petrenz, P., 1999, PhD thesis, Ludwig-Maximilians-University Munich
Porter, J. M., Skouza, B. A., 1999, A&A 344, 205
Puls, J., 1987, A&A 184, 227
Puls, J., Kudritzki, R. P., Herrero, A., Pauldrach, A. W. A., Haser, S. M., et al., 1996, A&A 305, 171
Puls, J., Springmann, U., Owocki, S.P., 1998. In: Cyclical Variability in Stellar Winds, ESO Astrophysical Symposia, eds. L. Kaper & A. W. Fullerton, p. 389
Puls, J., Petrenz, P., Owocki, S.P., 1999. In: Variable and Non-spherical Stellar Winds in Luminous Hot Stars, IAU Coll. 169, eds. B. Wolf, O. Stahl, A. W. Fullerton, Springer, Heidelberg, p. 131
Puls, J., Springmann, U., Lennon. M., 2000, A&AS 141, 23
Rybicki, G. B., Hummer, D. G., 1978, ApJ 219, 654
Schmutz, W.: 1991. In: Stellar atmospheres: Beyond classical models, NATO ASI Series C 314, eds. L. Crivellari, I. Hubeny, D. G. Hummer, Kluwer, Dordrecht, p. 191
Sobolev, V. V., 1957, Soviet Astr.–AJ 1, 678
Springmann, U. W. E., Pauldrach, A. W. A., 1992, A&A 262, 515
Springmann, U., 1997, PhD thesis, Ludwig-Maximilians-University, Munich
Springmann, U., Puls, J., 1998, In: Boulder-Munich II: Properties of hot, luminous stars, ed. I. D. Howarth, PASPC 131, 286
Stone, J. M. , Norman, M. L., 1992, ApJS 80, 753
von Zeipel, H., 1924, MNRAS 84, 665
Venn, K. A., Dieng, M., Lennon, D. J., Kudritzki, R.-P., 1999, A&AS 194, 1303
Wolf, B., Stahl, O., Fullerton, A. (eds.), 1999, Variable and Non-spherical Stellar Winds in Luminous Hot Stars, IAU Coll. 169, Springer, Heidelberg
Zickgraf, F.-J., Wolf, B., Stahl, O., Leitherer, C., Appenzeller, I., 1986, A&A 163, 119
Zickgraf, F.-J., 1999. In: Variable and Non-spherical Stellar Winds in Luminous Hot Stars, IAU Coll. 169, eds. B. Wolf, O. Stahl, A. W. Fullerton, Springer, Heidelberg, p. 40